

ULTRA-FAST, HIGH-TEMPERATURE MICROWAVE PROCESSING OF SILICON  
CARBIDE AND GALLIUM NITRIDE

by

Siddarth G. Sundaresan  
A Dissertation  
Submitted to the  
Graduate Faculty  
of  
George Mason University  
In Partial fulfillment of  
The Requirements for the Degree  
of  
Doctor of Philosophy  
Electrical and Computer Engineering

Committee:

Mulpuri, V. Rao  
D. E. Ioannou  
Alok K. Berry  
John A. Schreifels  
Albert V. Davydov  
André Manitius  
Lloyd J. Griffiths

Dr. Mulpuri V. Rao, Dissertation Director  
Dr. Dimitrios E. Ioannou, Committee Member  
Dr. Alok K. Berry, Committee Member  
Dr. John A. Schreifels, Committee Member  
Dr. Albert V. Davydov, Committee Member  
Dr. André Manitius, Department Chairperson  
Dr. Lloyd J. Griffiths, Dean, The Volgenau  
School of Information Technology and  
Engineering

Date: SEPTEMBER 27, 2007

Fall Semester 2007  
George Mason University  
Fairfax, Virginia.

Ultra-Fast High Temperature Microwave Processing Of Silicon Carbide And Gallium  
Nitride

A dissertation submitted in partial fulfillment of the requirements for the degree of  
Doctor of Philosophy at George Mason University

By

Siddarth G. Sundaresan  
Master of Science  
George Mason University, 2004

Director: Mulpuri V. Rao, Professor  
Department of Electrical and Computer Engineering

Fall Semester 2007  
George Mason University  
Fairfax, VA

Copyright 2007 Siddarth G. Sundaresan  
All Rights Reserved

## **DEDICATION**

This work is dedicated to my mother, Usha Sundaresan and father, Gopala Sundaresan for all their love and support, without which this work would not have been possible.

## ACKNOWLEDGEMENTS

I would like to thank Dr. Yong-Lai Tian of LT Technologies and Dr. Albert Davydov of NIST for firstly allowing me access to the microwave system and NIST facilities, respectively, and also for spending so many hours discussing issues related to my Ph.D. project.

I gratefully acknowledge the support from the following grants that made this work possible: Army Research Office (Dr. Prater) under Grant # W911NF-04-1-0428, National Science Foundation under Award # ECS-0618948, and subcontracts from LT Technologies under NSF SBIR Grants # 0539321 and # 0646184.

Thanks are also due to Dr. Chip Eddy (NRL), Dr. Syed Qadri (NRL), Dr. Jaime Freitas (NRL), Dr. John Schreifels (GMU), Dr. R.D. Vispute (UMD), Dr. Elba-Gomar Nadal (UMD), Dr. Ken Jones (ARL), Dr. Mark Vaudin (NIST), Dr. Igor Levin (NIST), Dr. James Maslar (NIST), Dr. Mark Ridgway (ANU), Nadeem Mahadik (GMU) and Madhu Murthy (GMU). Each has contributed greatly toward this work.

I would also like to thank Abhishek Motayed, Brian Polk, Madhav Ranganathan, Rama Sreenivasan and Ganesh Ramachandran, for helping me through the difficult times and constantly motivating me. I am also greatly indebted to Rahul Radhakrishnan and Meera Rahul for putting up with me (which I'm sure wasn't easy) at their house for the last two years.

Last but by no means the least, I would like to sincerely thank my Ph.D. advisor, Prof. Rao Mulpuri for supporting me through thick and thin during the last 4½ years. I also wish to thank him for giving me the freedom to work on some of my inventive ideas which have since spun-off into separate projects.

## TABLE OF CONTENTS

	<b>Page</b>
Abstract.....	xii
Page.....	v
1. INTRODUCTION.....	1
1.1 Why silicon carbide (SiC) and gallium nitride (GaN)?.....	1
1.2 Why is a high processing temperature required for fabricating SiC and GaN devices?.....	3
1.3 Disadvantages of conventional annealing techniques.....	5
1.4 Ultra-fast solid-state microwave annealing.....	5
1.5 SiC nanowires.....	8
2. MICROWAVE ANNEALING OF ION-IMPLANTED SILICON CARBIDE.....	12
2.1 Existing issues:.....	12
2.2. Uncapped microwave annealing.....	20
2.2.1 Annealing in an uncontrolled (air) ambient.....	20
2.2.1.2 Surface morphology.....	21
2.2.1.3 Surface chemistry study.....	25
2.2.1.4 Thermal stability of Boron implanted SiC.....	29
2.2.1.5 Rutherford back-scattering (RBS) study.....	33
2.2.1.6. Electrical Characteristics of Nitrogen Implanted SiC.....	35
2.2.1.7. Electrical Characteristics of Aluminum implanted SiC.....	37
2.2.1.8 Conclusions from uncapped microwave annealing of ion-implanted SiC in uncontrolled ambient.....	40
2.2.2 Microwave annealing in a pure nitrogen atmosphere.....	40
2.2.2.1 Implantation and annealing schedules.....	41
2.2.2.2 Atomic Force Microscopy (AFM) study of the surface morphology.....	43
2.2.2.3 Annealed SiC surface chemical analysis using Auger electron spectroscopy (AES) and x-ray photoelectron spectroscopy (XPS).....	45
2.2.2.4 Investigation of surface sublimation and/or dopant redistribution.....	47
2.2.2.5 Rutherford backscattering channeling (RBS-C) study.....	49
2.2.2.6 Electrical characteristics of aluminum implanted 4H-SiC.....	51
2.2.2.8 Electrical characteristics of phosphorus implanted 4H-SiC.....	55
2.2.2.9 Summary of uncapped microwave annealing in a pure nitrogen ambient.....	57
2.3 Microwave annealing with a protective graphite cap.....	59
2.3.1 Experimental details regarding implantation, annealing and graphite capping.....	60
2.3.2 XPS characterization of the graphite cap.....	61

2.3.3 Surface morphology of the graphite capped microwave annealed material.....	63
2.3.4 SIMS depth profiles.....	65
2.3.5 X-ray diffraction study .....	68
2.3.6 Rutherford backscattering – channeling (RBS-C) study.....	73
2.3.7 Electrical characterization .....	75
2.3.8 Conclusions from graphite capped annealing .....	79
2.4 Summary and suggested future work on microwave annealing of ion-implanted SiC	79
3. MICROWAVE ANNEALING OF IN-SITU AND ION-IMPLANTED ACCEPTOR DOPED GALLIUM NITRIDE .....	81
3.1 Existing issues concerning acceptor activation in in-situ and ion-implantation doped GaN .....	81
3.2 Microwave annealing of in-situ Mg doped GaN.....	89
3.2.1 Experimental Details .....	89
3.2.2 XPS characterization of AlN capped GaN.....	90
3.2.3. Surface morphology of the microwave annealed samples .....	92
3.2.4. Photoluminescence characterization .....	95
3.2.5. Electrical Characterization .....	99
3.2.6 Conclusions from microwave annealing of in-situ Mg doped GaN.....	101
3.3 Microwave annealing of Mg-implanted GaN .....	102
3.3.1 Implantation and annealing schedules.....	102
3.3.2 SIMS depth profiling.....	103
3.3.3 Photoluminescence characterization .....	105
3.3.4 Electrical characterization .....	109
3.4 Summary and suggested future work on microwave annealing of GaN.....	109
4. SILICON CARBIDE NANOWIRES.....	111
4.1 Introduction .....	111
4.2 Sublimation-sandwich method developed in this work to grow SiC nanowires.....	111
4.3 Unique features of the sublimation-sandwich method used in this work compared to other techniques employed for nanowire growth.....	114
4.4 Experimental parameters related to SiC nanostructure growth.....	115
4.5 Experimental apparatus used for characterizing SiC nanostructures .....	115
4.6 Morphology and chemical composition of SiC nanowires .....	116
4.7 Crystallography of the SiC nanowires.....	121
4.8 Raman study of the SiC nanowires .....	129
4.9 Summary and suggested future work on SiC nanowires.....	131
5. CONCLUSIONS AND FUTURE WORK.....	133
5.1 Conclusions .....	133
5.2 Future work .....	134
6. APPENDIX.....	137

## LIST OF TABLES

Table	Page
Table I: A comparison of material properties for Si, GaAs, SiC, and GaN [Ref: <a href="http://www.nitronex.com/education/ganHEMT.pdf">http://www.nitronex.com/education/ganHEMT.pdf</a> ].	2
Table II: Sheet resistance obtained after conventional furnace annealing of Al <sup>+</sup> - SiC.	14
Table III: Electrical characteristics of single- and multiple- energy nitrogen implanted 6H-SiC annealed by solid-state microwave (SSM) annealing and conventional furnace annealing.	36
Table IV: Electrical characteristics of solid-state microwave annealed, 25 – 200 keV multiple energy Al <sup>+</sup> implanted SiC for a total implant dose of $2.7 \times 10^{15} \text{ cm}^{-2}$ . The implant temperature is 600 °C.	38
Table V: Implant schedules for microwave annealing in a pure nitrogen atmosphere.	42
Table VI: RMS Surface roughness extracted from tapping mode 5 μm x 5 μm AFM scans of Al <sup>+</sup> - implanted SiC. The noise level in the measurements is measured to be 0.15 nm.	44
Table VII: Unintentionally grown oxide/nitride film thickness as a function of annealing temperature for 15 s microwave annealing in a pure nitrogen atmosphere.	46
Table VIII: List of the electrical characteristics of p-type GaN available from literature.	82
Table IX: Multiple Energy implant schedule performed into GaN.	104

## LIST OF FIGURES

Figure	Page
<b>Figure 1:</b> Block diagram of the solid-state microwave annealing system developed and employed in this work.....	7
<b>Figure 2:</b> A typical heating cycle achievable with the microwave annealing system used in this work. The sample used in this case was 4H-SiC. The applied microwave power in this case was 104 W, and a steady state temperature of ~1800 °C was maintained for ~ 15 seconds. ....	9
<b>Figure 3:</b> RBS measurements on boron, aluminum and nitrogen implant profiles after a 1750 °C / 10 min conventional furnace anneal. Much of the N-implant damage is removed after annealing, whereas residual damage is clearly observed for both the Al and B implants. ....	15
<b>Figure 4:</b> Atomic force micrographs of Al <sup>+</sup> -implanted SiC, (a) annealed at 1500 °C for 10 min and (b) annealed at 1600 °C for 10 min. ....	15
<b>Figure 5:</b> SIMS plots of a buried boron implant, before and after furnace annealing at 1400 °C for 10 min. The implant was performed at 200 keV with a dose of 1 x 10 <sup>15</sup> cm <sup>-2</sup> .....	17
<b>Figure 6:</b> Diffusion tail observed in a multiple energy boron implant profile after a 10 min, 1750 °C anneal.....	18
<b>Figure 7:</b> Atomic force microscope images of Al <sup>+</sup> -implanted 4H-SiC samples, (a) microwave annealed at 1570 °C for 10 s, ( b) microwave annealed at 1770 °C for 10 s, and (c) furnace annealed at 1500 °C for 15 min. ....	22
<b>Figure 8:</b> Plot of the root mean square (RMS) roughness extracted from the AFM images as a function of annealing temperature for 10 s – 35 s anneals for implanted SiC.....	23
<b>Figure 9:</b> FE-SEM images of (a) 1500 °C /15 min furnace annealed 4H-SiC sample and (b) 1770 °C / 10 s microwave annealed 4H-SiC sample.....	24
<b>Figure 10:</b> A typical Auger sputter profile showing the spatial variation of the elemental constituents of the silicon oxide film formed during the microwave annealing at 1820 °C.....	27
<b>Figure 11:</b> The variation of oxide thickness as a function of annealing temperature for the proximity cap and the face-up (direct exposure) sample configurations. ....	28
<b>Figure 12:</b> SIMS depth profile of a 50 keV / 8.8 x 10 <sup>14</sup> cm <sup>-2</sup> Boron implant before and after microwave annealing at 1670 °C for 10 s. A significant out-diffusion of boron is observed resulting in an overall loss of boron from the SiC surface.....	30

<b>Figure 13:</b> SIMS depth profiles for 200 keV / $1 \times 10^{15}$ cm <sup>-2</sup> B <sup>+</sup> implantation before and after 1670 °C/10 s microwave annealing and 1400 °C / 10 min furnace annealing.....	31
<b>Figure 14:</b> SIMS depth profile of a 1 MeV / $2 \times 10^{15}$ cm <sup>-2</sup> Boron implant before and after microwave annealing at 1670 °C for 10 s. ....	32
<b>Figure 15:</b> RBS spectra on 50 keV/ $3.1 \times 10^{15}$ cm <sup>-2</sup> N <sup>+</sup> -implanted material, before and after 1770 °C/25 s microwave annealing and 1600 °C/15 min conventional furnace annealing.....	34
<b>Figure 16:</b> XPS survey scan for an 1800 °C / 15 s microwave annealed virgin 4H-SiC sample in a pure nitrogen atmosphere. ....	46
<b>Figure 17:</b> SIMS depth profiles for Al <sup>+</sup> - implanted SiC, microwave annealed at 1800, 1950 and 2100 °C for 15 s. The profiles were shifted to the right to align the implant tail region with the as-implanted sample. Vertical dotted lines indicate the amount of the implant that had sublimed after microwave annealing.....	48
<b>Figure 18:</b> RBS-C aligned spectra for a virgin 4H-SiC sample, an Al <sup>+</sup> as-implanted sample, and a microwave annealed sample at 2050 °C / 15 s. RBS-C spectrum for a randomly aligned SiC sample is also shown for reference.....	50
<b>Figure 19:</b> Plot of sheet resistance as a function of annealing temperature in Al <sup>+</sup> - implanted 4H-SiC, for 15s and 30 s microwave anneals.....	52
<b>Figure 20:</b> Plot of sheet carrier concentration and hole mobility, as a function of the annealing temperature in Al <sup>+</sup> -implanted SiC for 15 s microwave anneals.....	52
<b>Figure 21:</b> Plot of sheet resistance and sheet hole concentration, as a function of annealing time in Al <sup>+</sup> -implanted 4H-SiC for 1950 °C annealing.....	54
<b>Figure 22:</b> Plot of sheet resistance and implant sheet carrier concentration, as a function of annealing temperature in P <sup>+</sup> -implanted 4H-SiC, for 30 s anneals.....	56
<b>Figure 23:</b> Plot of electron mobility as a function of microwave annealing temperature for 30 s anneals of P <sup>+</sup> -implanted samples.....	56
<b>Figure 24:</b> Plot of sheet resistance and sheet electron concentration, as a function of annealing time at 1925 °C in P <sup>+</sup> -implanted 4H-SiC.....	58
<b>Figure 25:</b> (a) XPS spectrum of the photoresist coated SiC surface microwave annealed at 1050 °C for 5 s. The binding energy of C1s at 283.7 eV is consistent with graphite. (b) XPS spectrum of the SiC surface after 1800 °C microwave annealing subsequent to removing the graphite cap by dry oxidation at 1050 °C for 2 hours. Inset shows narrow XPS scans of the C1s peak before and after the 1050 °C / 5 s microwave treatment showing the shifting of the C1s BE from 284.5eV (consistent with hydrocarbon) to 283.7 eV (consistent with graphite).....	62
<b>Figure 26:</b> Tapping mode AFM scans of Al-implanted 4H-SiC for different conditions: (a) as-implanted (b) 1800 °C / 5 min. conventional annealing using graphite cap, and (c) 1900 °C / 30 s microwave annealing using graphite cap. ....	64
<b>Figure 27:</b> SIMS Al depth profiles for the as-implanted, 1800 °C / 5 min. conventionally annealed, and the 1900 °C / 30 s microwave annealed Al-implanted 4H-SiC.....	67
<b>Figure 28:</b> $\theta$ -2 $\theta$ x-ray diffraction profile for the SiC (004) reflection for the Al as-implanted 4H-SiC sample, showing subsidiary peaks known as Kiessig fringes between the defect sub-lattice peak and the main epilayer peak.....	69

<b>Figure 29:</b> $\theta$ - $2\theta$ x-ray diffraction spectra for the (0,0,12) reflection from the Al as-implanted and the 1900 °C / 30 s microwave annealed 4H-SiC samples. ....	70
<b>Figure 30:</b> High resolution rocking curves of the SiC (004) from the Al as-implanted 4H-SiC sample, after conventional annealing at 1800 °C for 5 min., and after microwave annealing at 1850 °C and 1900 °C for 30 s.....	71
<b>Figure 31:</b> RBS-C spectra on Al as-implanted, 1800 °C / 5 min conventionally annealed and 1900 °C / 30 s microwave annealed 4H-SiC.....	74
<b>Figure 32:</b> Measured sheet resistance and hole mobility as a function of annealing temperature for the 30 s microwave annealing .....	76
<b>Figure 33:</b> Diffusion, recovery, and activation processes of ion-implanted impurities in GaN as a function of annealing temperature.....	84
<b>Figure 34:</b> AFM micrograph of Be <sup>+</sup> -implanted GaN, annealed by halogen lamp RTA at 1100 °C for 2 min.[H.T. Wang et al. J. Appl. Phys. <b>98</b> , 094901 (2005).].....	86
<b>Figure 35:</b> X-ray diffraction spectra $\theta$ - $2\theta$ recorded for (a) a MBE as-grown GaN sample, (b) a Be-implanted sample after combination of PLA and RTA (c) a Be-implanted sample after RTA, (d) a Be-implanted sample after PLA, and (e) a Be-implanted sample without annealing .....	86
<b>Figure 36:</b> Electrical characteristics of uncapped and AlN capped GaN, annealed using the Zapper furnace with heating rates of 50 °C / s .....	88
<b>Figure 37:</b> XPS survey scans of: (a) AlN as-capped GaN sample, (b) AlN capped sample after 1400 °C/5 s annealing, and (c) after removal of the AlN cap at the conclusion of annealing .....	91
<b>Figure 38:</b> Tapping mode AFM images of: (a) an as-grown GaN surface (RMS = 0.3 nm); after 1300 °C / 5 s microwave annealing of GaN layers with (b) no cap (RMS =9.2 nm), (c) MgO cap (RMS =0.8 nm), and (d) AlN cap (RMS = 1 nm); (e) after 1400 °C / 5 s annealing with MgO cap (RMS = 7.2 nm); and (f) after 1500 °C/5 s annealing with AlN cap (RMS = 0.6 nm).....	93
<b>Figure 39:</b> Low-temperature (5 K) PL spectra of as-grown Mg-doped GaN; and of AlN capped samples subjected to 5 s microwave annealing at 1300 °C and 1500 °C.....	96
<b>Figure 40:</b> Low-temperature (5 K) PL spectra of as-grown Mg-doped GaN; and of e-beam deposited MgO capped in-situ Mg-doped GaN samples after 5 s microwave annealing at 1300 °C and 1350 °C. ....	98
<b>Figure 41:</b> Hole concentration (p) as a function of annealing temperature for 5 s duration microwave annealing on uncapped, MgO capped, and AlN capped in-situ Mg-doped GaN. ....	100
<b>Figure 42:</b> A comparison of simulated and experimental (as-implanted) Mg multiple energy implant profile in GaN .....	104
<b>Figure 43:</b> SIMS depth profiles of Mg-implanted GaN, before and after 1300 °C/ 5 s and 1400 °C / 5 s microwave annealing .....	106
<b>Figure 44:</b> Low-temperature (5 K) PL spectra from an un-implanted GaN epilayer, and GaN epilayers before and after 1400 °C / 5 s and 1500 °C / 5 s microwave annealing.....	108
<b>Figure 45:</b> Schematic of the ‘sublimation-sandwich’ cell used to grow SiC nanowires ...	112
<b>Figure 46:</b> FESEM image of SiC nanowires grown at $T_s = 1700$ °C and $\Delta T = 150$ °C for 40 s. ....	118

<b>Figure 47:</b> Statistical distribution of the SiC nanowire diameters. About 42% of the nanowires have diameters $\leq 100$ nm.....	118
<b>Figure 48:</b> (a) Cone-shaped SiC nanostructures grown at $T_s = 1600$ °C and $\Delta T = 150$ °C. (b) Needle-shaped SiC nanostructures grown at $T_s = 1700$ °C and $\Delta T = 250$ °C .....	120
<b>Figure 49:</b> A typical x-ray diffraction spectrum obtained from the SiC nanowires grown in this work. ....	122
<b>Figure 50</b> (a) FESEM image of a SiC nanowire harvested on a heavily doped Si substrate. (b) EBSD pattern from the nanowire indexed to the 3C-SiC phase. (c) EBSD pattern from the nanowire tip indexed to $Fe_2Si$ . ....	123
<b>Figure 51:</b> EBSD patterns from the catalytic tip of the SiC nanowires grown using (a) Ni catalyst. (EBSD pattern indexed to $Ni_3Si$ ) (b) Pd catalyst (EBSD pattern indexed to $Pd_2Si$ ). (c) Pt catalyst (EBSD pattern indexed to $PtSi$ ). ....	125
<b>Figure 52:</b> Representative $\langle 101 \rangle$ selected area electron diffraction pattern recorded from a single SiC nanowire. The reflections are indexed according to the F-centered cubic 3C-SiC unit cell. ....	127
<b>Figure 53:</b> Diffraction contrast TEM images of two types of 3C-SiC nanowires. (a) twin-like defects are observed on different sets of $\{111\}$ planes. ....	128
<b>Figure 54:</b> $\mu$ -Raman spectrum from an isolated SiC nanowire.....	130

## **ABSTRACT**

### **ULTRA-FAST, HIGH-TEMPERATURE MICROWAVE PROCESSING OF SILICON CARBIDE AND GALLIUM NITRIDE**

Siddarth G. Sundaresan, Ph.D.

George Mason University, 2007

Dissertation Director: Prof. Mulpuri V. Rao

A novel solid-state microwave annealing technique is developed in this work for post-implantation annealing of SiC and GaN, and for the controlled growth of SiC nanowires. This technique is capable of heating SiC samples to temperatures in excess of 2100 °C, at ultra-fast temperature ramping rates  $> 600$  °C/s.

Microwave annealing of ion-implantation doped (both p-type and n-type) hexagonal SiC was performed in an uncontrolled (air) ambient, as well as a controlled 100% atmosphere of nitrogen, with or without a protective graphite cap. Microwave annealing was performed in the temperature range of 1500 °C – 2120 °C, for durations of 5 s – 60 s. Uncontrolled ambient microwave annealing of SiC at temperatures  $> 1700$  °C resulted in a significant oxidation of the SiC surface, leading to a loss of the implanted layer. Annealing in a 100% nitrogen atmosphere eliminated the oxidation problem. For microwave annealing at temperatures  $\geq 1800$  °C, significant SiC sublimation was

observed, even for 15 s annealing. Microwave annealing with a photoresist-converted graphite cap solved this surface sublimation problem for annealing temperatures up to 2100 °C. For the P<sup>+</sup> and Al<sup>+</sup>-implanted SiC, sheet resistances as low as 14 Ω/ and 1.9 kΩ/ and majority carrier mobilities as high as 100 cm<sup>2</sup>/Vs and 8.3 cm<sup>2</sup>/Vs, respectively, were obtained. For the Al<sup>+</sup>-implanted SiC, sheet resistances as low as 1.9 kΩ/ and hole mobilities as high as 8.3 cm<sup>2</sup>/Vs were obtained. These values constitute the best ever reported electrical characteristics for ion-implanted SiC. Microwave annealing at temperatures > 1800 °C not only removed the implantation-induced lattice damage but also the defects introduced during crystal growth.

Microwave annealing of in-situ as well as ion-implantation acceptor doped GaN was performed in the temperature range of 1200 °C – 1600 °C, for a duration of 5 s, using different protective caps (AlN, MgO, graphite) for protecting GaN surfaces during annealing. Pulsed-laser deposited AlN was found to protect the GaN surface effectively, for microwave annealing at temperatures as high as 1500 °C. The RMS surface roughness (0.6 nm) of the GaN sample annealed at 1500 °C with an AlN cap is similar to the value (0.3 nm) measured on the as-grown sample with a decrease in the compensating deep donor concentration.

Cubic 3C-SiC nanowires were grown by a novel Fe, Ni, Pd, and Pt metal catalyst-assisted sublimation-sandwich (SS) method. The nanowire growth was performed in a nitrogen atmosphere, in the temperature range of 1650 °C to 1750 °C for 40 s durations. The nanowires grow by the vapor-liquid-solid (VLS) mechanism facilitated by metal catalyst islands. The nanowires are 10 μm to 30 μm long with about 52% of them having

diameters in the range of 15 nm – 150 nm, whereas 14% of the nanowires had diameters in excess of 300 nm.

# 1. INTRODUCTION

## 1.1 Why silicon carbide (SiC) and gallium nitride (GaN)?

A comparison of material properties of several semiconductors, Si, GaAs, SiC and GaN is provided in Table I. The SiC and GaN belong to a class of semiconductors known as wide band-gap semiconductors. Silicon carbide is a wide band gap semiconductor that possesses high thermal conductivity, high breakdown electric field and also chemical and mechanical stability. As a consequence, SiC devices can perform under high-temperature, high-power, and/or high-radiation conditions in which conventional (i.e. narrow band gap) semiconductors cannot adequately perform<sup>1,2</sup>. Silicon carbide's ability to function under extreme conditions is expected to enable significant improvements to a far ranging variety of applications and systems. SiC power devices have improved high-voltage switching characteristics compared with conventional semiconductors like Si and GaAs. Applications of high-power SiC devices range from public electric power distribution and electric vehicles to more powerful solid state microwave sources for radar and communications to sensors and controls for cleaner-burning, more fuel-efficient, jet aircraft and automobile engines<sup>1,2</sup>.

Gallium nitride (GaN) is another important direct, wide-bandgap semiconductor for high-power solid-state devices, especially for those intended for microwave frequency

**Table I:** A comparison of material properties for Si, GaAs, SiC, and GaN [Ref: <http://www.nitronex.com/education/ganHEMT.pdf>]

<b>Attribute</b>	<b>Si</b>	<b>GaAs</b>	<b>4H- SiC</b>	<b>GaN</b>
Energy Gap (eV)	1.11	1.43	3.2	3.4
Breakdown E-Field (V/cm)	$6.0 \times 10^5$	$6.5 \times 10^5$	$3.5 \times 10^6$	$3.5 \times 10^6$
Saturation Velocity (cm/s)	$1.0 \times 10^7$	$2.0 \times 10^7$	$2.0 \times 10^7$	$2.5 \times 10^7$
Electron Mobility (cm <sup>2</sup> /V-s)	1350	6000	800	1600*
Thermal Conductivity (W/cmK)	1.5	0.46	3.5	1.7
Heterostructures	SiGe/Si	AlGaAs/GaAs InGaP/GaAs AlGaAs/InGaAs	None	AlGaN/GaN InGaN/GaN

\* Typical two-dimensional electron gas mobility for AlGaN/GaN heterostructures.

range and also for optoelectronics applications on account of its direct bandgap<sup>3</sup>. The GaN based high electron mobility transistors (HEMTs) have defined state-of-the-art for output power density and have the potential to replace GaAs based transistors for a number of high-power applications<sup>4</sup>. The advantages of GaN over other semiconductors include: a high breakdown field (3 MV/cm, which is ten times larger than that of GaAs); a high saturation electron velocity ( $2.5 \times 10^7$  cm/s), and the capacity of the III-nitride material system to support heterostructure device technology with a high two-dimensional electron gas (popularly known as 2-DEG) density and high carrier mobility<sup>3,5</sup>. Another attractive feature of all III-nitride semiconductors is the possible polarization-induced bulk three-dimensional doping without physically introducing shallow donors<sup>3,5</sup>. The strong piezoelectric effect and a large spontaneous polarization in the III-nitride system allows for the incorporation of a large electric field ( $> 10^6$  V/cm) and a high sheet charge density ( $> 10^{13}$  cm<sup>-2</sup>) without doping. This helps to realize a variety of high-performance and high-power microwave devices.

## **1.2 Why is a high processing temperature required for fabricating SiC and GaN devices?**

Ion-implantation is an indispensable technique for selective area doping of SiC and GaN, for fabricating high-power electronic and opto-electronic devices. Other doping methods such as thermal diffusion are impractical for SiC and GaN technologies because the diffusion coefficients of the technologically relevant dopants in SiC and GaN is very small, even at temperatures in excess of 1800 °C<sup>6,7</sup>. However, ion-implantation being a

highly energetic process causes damage to the semiconductor crystal lattice; also the as-implanted dopants do not reside in electrically active substitutional sites in the semiconductor lattice. Therefore, ion-implantation always needs to be followed by a high-temperature annealing step for alleviating the implantation-induced lattice damage and for activating the implanted dopants (i.e. moving them from interstitial to electrically active substitutional lattice sites).

For SiC, the implanted n-type dopants (nitrogen and phosphorus) require annealing temperatures in the range of 1500 – 1700 °C, whereas implanted p-type dopants (aluminum and boron) require temperatures in excess of 1800 °C<sup>8</sup>. The higher annealing temperatures required for p-type dopants is a result of the higher activation energy for forming the substitutional Al<sub>Si</sub> species compared to the P<sub>Si</sub> and N<sub>C</sub> species. Also, the lattice damage introduced by Al implantation requires higher annealing temperatures to be removed as opposed to the lattice damage introduced by the P and N implantation<sup>8</sup>. For implanted n-type dopants (e.g. Si) in GaN, annealing temperatures in the range of 1200 °C are required, whereas implanted p-type dopants (Mg and Be) in GaN require annealing temperatures in excess of 1300 °C for satisfactorily removing implantation-induced lattice damage, for activating the implanted dopants, and for recovering the luminescence properties (which are severely degraded by the ion-implantation)<sup>3,5,9</sup>. The higher temperature requirement for activating p-type implants compared to n-type implants in GaN is primarily due to the much larger formation energy of the substitutional Mg<sub>Ga</sub> species compared to the Si<sub>Ga</sub> species.

### **1.3 Disadvantages of conventional annealing techniques**

Traditionally, post-implantation annealing of SiC is performed in either resistively or inductively heated, high-temperature ceramic furnaces, since ultra-high temperatures  $> 1600\text{ }^{\circ}\text{C}$  are required. The furnaces used for annealing SiC have modest (few  $^{\circ}\text{C}/\text{s}$ ) heating and cooling rates, which makes annealing SiC at temperatures  $> 1500\text{ }^{\circ}\text{C}$  impractical because of an excessive SiC sublimation that one encounters at such high temperatures when exposed for long durations. The problem has been alleviated somewhat by capping the SiC surface with a layer of graphite prior to annealing, but still the maximum annealing temperatures are limited to  $1800\text{ }^{\circ}\text{C}$ . Even higher temperatures are required, especially for activating implanted p-type dopants in SiC and for healing the implantation-induced lattice damage.

As for GaN, temperatures  $> 1300\text{ }^{\circ}\text{C}$  are required for completely activating in-situ as well as ion-implanted p-type dopants. However, when annealed at temperatures  $> 800\text{ }^{\circ}\text{C}$ , GaN decomposes into Ga droplets due to the nitrogen leaving the surface. Annealing of GaN is performed in halogen lamp-based RTA systems, due to the rapid heating/cooling rates accorded by these RTA systems. However, due to their quartz hardware, these halogen lamp based RTA systems are limited to a maximum temperature of  $1200\text{ }^{\circ}\text{C}$ , which is not sufficient to effectively anneal p-type GaN.

### **1.4 Ultra-fast solid-state microwave annealing**

Solid-state microwave heating is advantageous for high-temperature processing of wide-bandgap semiconductors such as SiC and GaN. The microwave heating system has

a capability to reach sample temperatures  $> 2000\text{ }^{\circ}\text{C}$  (for SiC wafers) with heating and cooling rates in excess of  $600\text{ }^{\circ}\text{C/s}$ .

The solid-state microwave RTP system used in this work, with the schematic shown in Fig. 1, has three main building blocks: 1. a variable frequency microwave power source, which consists of a signal generator and a power amplifier; 2. a heating system, which consists of a tuning and coupling circuit and a heating head, and 3. a measurement and control system which consists of a network analyzer, a computer, an optical pyrometer and other equipment. Microwave power generated by the variable frequency power source is amplified and then coupled to a SiC sample through the heating head. The sample temperature is monitored by an infrared pyrometer. The SiC and GaN sample emissivities were both measured as 0.8 using a blackbody source and this emissivity value was keyed into the pyrometer for all temperature measurements of this study.

The microwave system used in this work can be tuned to efficiently heat semiconductor samples at variable frequencies. However, the microwave amplifier used for the experiments in this study delivers maximum stable power ( $\approx 150\text{ W}$ ), only in the frequency range of 910 – 930 MHz. Therefore, the microwave system was appropriately tuned for an operating frequency of 920 MHz, which was used for all the experiments of this work. A typical temperature/time cycle of this system for heating 5 mm x 5 mm heavily (in-situ) doped 4H-SiC is shown in Fig. 2. Since the samples are placed in an enclosure made of microwave transparent, high-temperature stable ceramics such as boron nitride and mullite, microwaves only heat the strong microwave absorbing

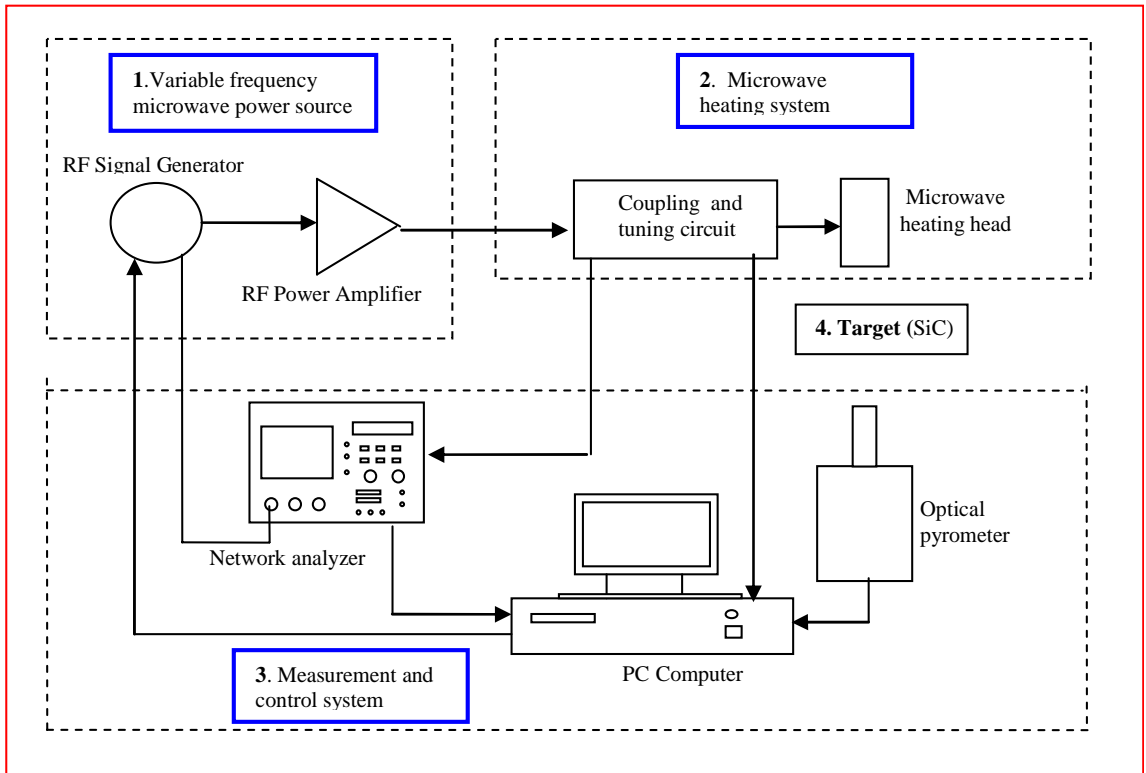


**Figure 1:** Block diagram of the solid-state microwave annealing system developed and employed in this work.

(electrically conductive) semiconducting films, which present a very low thermal mass in comparison with a conventional furnace where the surroundings of the sample are also heated. Thus, heating rates  $> 600$  °C/s are possible. In fact, selective heating of thin, highly doped semiconductor layers is possible if the doped layers are formed on semi-insulating or insulating substrates. Therefore, for efficient microwave annealing of implanted semi-insulating (SI) SiC substrates and GaN epilayers grown on (electrically insulating) sapphire substrates, a 5 mm x 5 mm heavily doped 4H-SiC sample was placed as a susceptor directly underneath the sample to be annealed. It was possible to directly couple microwave power and heat GaN epilayers grown on sapphire, without using any susceptor. However, the spatial distribution of temperature across the sample was observed to be extremely non-uniform. Placing a SiC susceptor sample underneath the GaN sample of interest solved this problem.

### **1.5 SiC nanowires**

Over the past decade, one dimensional (1-D) semiconductor nanostructures, such as nanotubes and nanowires, have attracted special attention due to their high aspect and surface to volume ratios, small radius of curvature of their tips, absence of 3-D growth related defects such as threading dislocations, and fundamentally new electronic properties resulting from quantum confinement<sup>10,11</sup>. These nanostructures are expected to play a crucial role as building blocks for future nanoscale electronic devices and nanoelectromechanical systems (NEMS), designed using a bottom-up approach<sup>12-14</sup>. The 1D and quasi-1D nanowires of Si, GaN, ZnO, SiC and other semiconductors have been

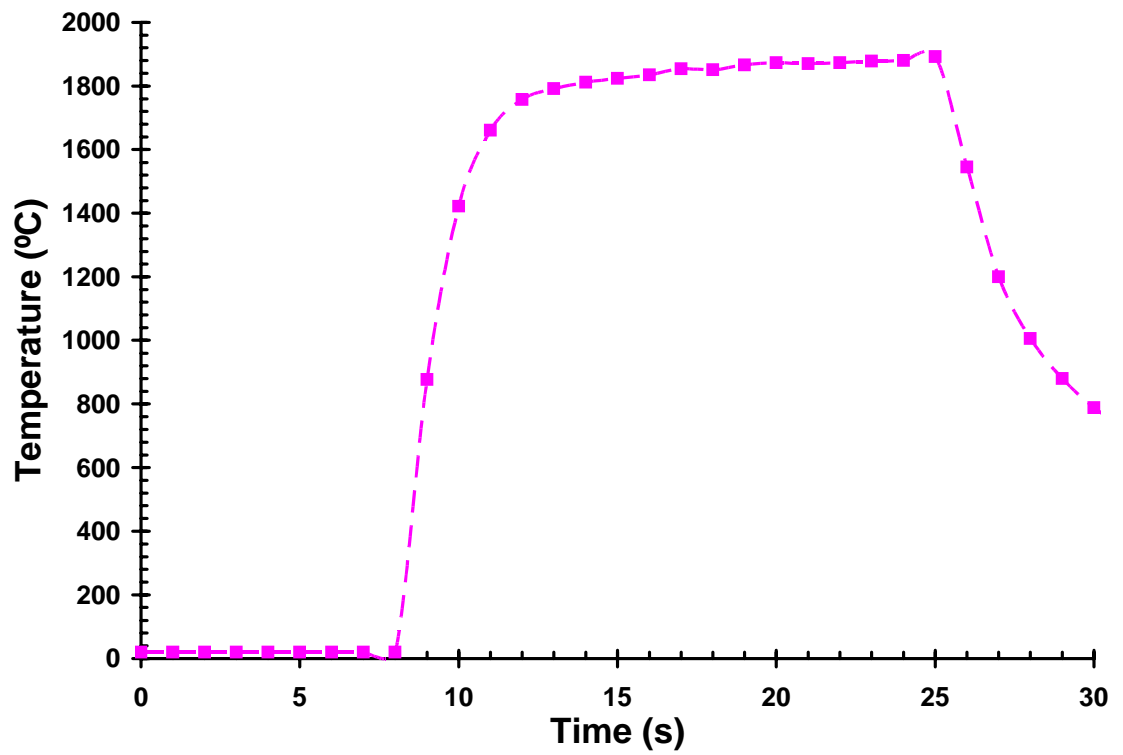


**Figure 2:** A typical heating cycle achievable with the microwave annealing system used in this work. The sample used in this case was 4H-SiC. The applied microwave power in this case was 104 W, and a steady state temperature of ~1800 °C was maintained for ~ 15 seconds.

synthesized<sup>10,11</sup>. Silicon carbide, due to its wide bandgap, high electric breakdown field, mechanical hardness, and chemical inertness, offers exciting opportunities in fabricating nanoelectronic devices for chemical/biochemical sensing, for high-temperature, for high-frequency and for aggressive environment applications<sup>15</sup>. Several techniques have been applied to synthesize SiC nanowires using physical evaporation<sup>16</sup>, chemical vapor deposition<sup>17-19</sup>, laser ablation<sup>14,20,21</sup>, and various other techniques<sup>22-31</sup>. An intriguing feature of SiC is its ability to crystallize in over 200 different polytypes. There has been a lot of research (and debate) over the physical basis underlying polytypism in SiC<sup>32</sup>. However, the thermodynamically stable polytypes of SiC include 3C (zincblende), 2H (wurtzite), 4H, 6H, and 15R. The other polytypes can be synthesized only under special conditions. The 4H- and 6H- polytypes are most favorable for fabricating electronic devices on account of their larger bandgap (3.0 eV for 6H, 3.2 eV for 4H), higher electron mobilities and higher breakdown electric field strength. In nanowire form, it is very difficult to synthesize 4H- and 6H- polytypes due to the low surface energy for the 3C- polytype. Finding suitable growth conditions for synthesizing 4H- and 6H- SiC nanowires is still the subject of extensive research.

## **1.6 What is done in this work?**

In this work, the feasibility of solid-state microwave processing is demonstrated for post-implantation annealing of SiC, for achieving dopant activation in in-situ and ion-implantation doped GaN, and for growing 3C-SiC nanowires.

Aluminum, boron, nitrogen and phosphorus implanted SiC are subjected to ultra-fast microwave annealing at temperatures in the range of 1500 – 2120 °C, for durations of 5 s – 1 min. The annealed material is subjected to surface, electrical and structural characterization in order to study the improvement in the material properties in comparison with conventional furnace annealing. The annealing of ion-implanted SiC is performed in different ambients, with and without a surface capping layer of graphite.

In-situ Mg doped and Mg ion-implanted GaN epilayers are subjected to microwave annealing in the temperature range of 1300 – 1600 °C, for short 5 s annealing durations. The feasibility of using various capping materials such as graphite, MgO, and AlN for protecting the GaN surface during high-temperature microwave annealing is explored. After annealing, the GaN layers are thoroughly characterized for determining the luminescence, electrical and surface morphology/chemistry properties.

The difference in microwave absorption by semiconductors with different electrical conductivities is exploited in this work to construct a sublimation sandwich cell for growing different morphologies of quasi 1-D, 3C-SiC nanostructures. Specific conditions that facilitate the growth of nanowires, needle-shaped and cone-shaped nanostructures are identified. These SiC nanostructures are grown at temperatures in the range of 1500 – 1750 °C, for durations of 15 s – 40 s.

## 2. MICROWAVE ANNEALING OF ION-IMPLANTED SILICON CARBIDE

### 2.1 Existing issues:

As discussed in Chapter 1, N and P (the n-type dopants) ion-implanted SiC require temperatures in the range of 1500 °C – 1700 °C for efficient annealing, whereas Al and B (the p-type dopants) ion-implanted SiC require annealing temperatures in excess of 1800 °C. There are several critical problems in the current techniques used for post-implant annealing of SiC at the high-temperatures<sup>33</sup>:

1. Ineffective crystal recovery and low implant activation efficiency.
2. Loss of Si and dopant impurities from SiC wafer due to surface sublimation.
3. High surface roughness due to evaporation and re-deposition of Si species at surface
4. Significant dopant redistribution in case of boron implants.

The first problem of ineffective crystal recovery and low activation efficiency results in a low carrier concentration and a low mobility and thus a poor sheet resistance. Minimum sheet resistance reported for conventional annealing techniques can be as high as  $10^4 \Omega/$  -  $10^5 \Omega/$  for Al<sup>+</sup> and B<sup>+</sup> implanted p-type SiC (see Table II) and  $10^2 \Omega/$  -  $10^3 \Omega/$  for N<sup>+</sup> implanted n-type SiC<sup>33-37</sup>. Both are a few orders of magnitude higher than the 27

$\Omega$ / obtained for  $P^+$  implanted n-type SiC<sup>38,39</sup>. Fig. 3 shows the Rutherford backscattering – channeling (RBS-C) measurements performed on boron, aluminum and nitrogen implant profiles after a 1750 °C / 10 min conventional furnace anneal as reported by Seshadri et al [see Fig. 3]. Clearly, the scattering yield in all the annealed samples is much higher than the yield from the aligned virgin sample, indicating that the conventional furnace anneal was unsuccessful in alleviating the implant-generated lattice damage. The second problem of surface sublimation results in a loss of the implanted layer. The third problem of surface roughness will also have negative effect on the performance of SiC devices such as degradation of inversion mobility and on-resistance of SiC MOSFETs<sup>40</sup>. The fourth problem of the boron implant redistribution prevents one from designing accurate buried boron implant profiles in device applications. Atomic Force Microscopy (AFM) scans of the surface morphology of conventional furnace annealed samples are shown in Fig. 4. Raising the annealing temperature and reducing the heating time are keys in solving the most critical problems in the post-implant annealing process of SiC. An increase of temperature will be the most effective means to achieve complete activation because the damage recovery and carrier activation are essentially thermal diffusion related processes<sup>41</sup>. Furthermore, the impurity solubility is also increased with increasing annealing temperature, resulting in a high carrier concentration and high implant activation efficiency. However, long exposure at very high temperatures causes serious problems of surface sublimation and increase in roughness. Therefore a short heating duration accompanied with high temperature ramping rates is a must. Senzaki et al.<sup>42</sup>

**Table II:** Sheet resistance obtained after conventional furnace annealing of Al<sup>+</sup> - SiC

<b>Implant details</b>	<b>Annealing Temperature ( °C)</b>	<b>Annealing Time (min)</b>	<b>Sheet Resistance R<sub>s</sub> (Ω/ )</b>	<b>Ref</b>
0.9 x 10 <sup>20</sup> cm <sup>-3</sup> 30 keV – 260 keV 0.4 μm deep	1600	40	5.4 x 10 <sup>4</sup>	40
	1800		3.2 x 10 <sup>4</sup>	
1.2x10 <sup>15</sup> cm <sup>-2</sup> (30-180) keV	1700	30	2.1 x 10 <sup>4</sup>	43
	1770	5	3.8 x 10 <sup>4</sup>	
	1770	2	4.8 x 10 <sup>4</sup>	
1.0 x 10 <sup>20</sup> cm <sup>-3</sup> 0.3 μm deep	1600	30	9.8 x 10 <sup>4</sup>	44
	1650		4.8 x 10 <sup>4</sup>	
	1700		1.5 x 10 <sup>4</sup>	

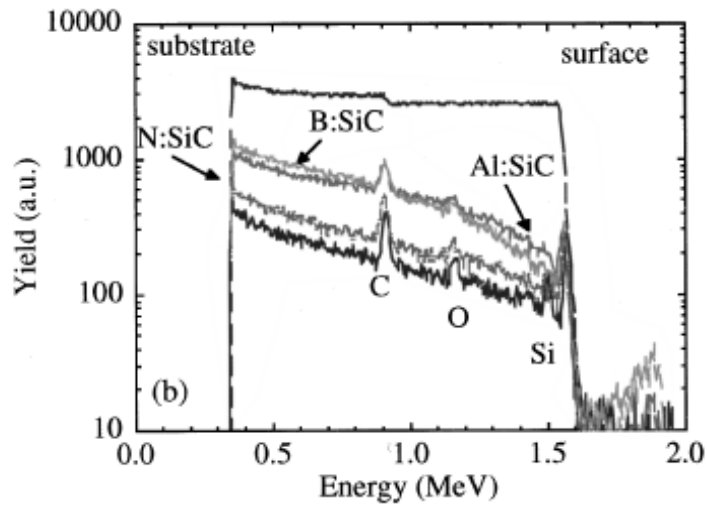


**Figure 3:** RBS measurements on boron, aluminum and nitrogen implant profiles after a 1750 °C / 10 min conventional furnace anneal [S. Sheshadri et al. Appl. Phys. Lett. 72(16), 2026 (1998)]. Much of the N-implant damage is removed after annealing, whereas residual damage is clearly observed for both the Al and B implants.

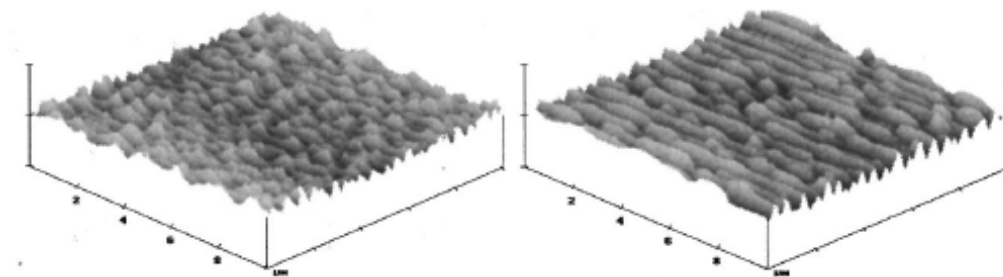


**Figure 4:** Atomic force micrographs of Al<sup>+</sup> -implanted SiC, (a) annealed at 1500 °C for 10 min and (b) annealed at 1600 °C for 10 min. (M.V. Rao et al. J.App. Phys. 86(2), 752 (1999)).

have demonstrated that annealing time can be reduced from 50 minutes to 30 seconds with no change in sheet resistance ( $< 100 \Omega/ \square$ ) in annealing of  $P^+$  implanted SiC at 1700 °C. As a consequence, the surface roughness reduced from 14 nm to 3 nm correspondingly. Recently, annealing was performed on as-grown semi-insulating (SI) 4H-SiC material at temperatures as high as 2600 °C<sup>45</sup>. It was found that this ultra-high temperature annealing increased the minority carrier lifetime in the SiC from  $< 10$  ns to  $15.5 \mu\text{s}$ <sup>45</sup>, which translated to a high ambipolar carrier lifetime of  $3 \mu\text{s}$  for 10 kV p-i-n diodes fabricated in that work. A high ambipolar carrier lifetime (in the  $\mu\text{s}$  range) is necessary to fabricate efficient 10 kV p-i-n diodes in SiC<sup>45</sup>. These results are encouraging and indicate that it is feasible to suppress the evaporation and the surface roughness by minimizing heating time without jeopardizing good dopant activation.

Boron is known to diffuse extensively in Si and SiC by a transient enhanced diffusion process even at low temperatures due to its small atomic size. This prevents one from designing accurate boron profiles in SiC. Secondary ion mass spectrometry (SIMS) depth profiles of a 200 keV,  $1 \times 10^{15} \text{ cm}^{-2}$  boron implant subjected to 1400 °C / 10 min conventional furnace annealing is shown in Fig. 5. Even at such low temperatures (which are not high enough for electrical activation of boron in SiC), appreciable redistribution of the boron profile can be noticed. SIMS profiles of a multiple energy B profile in SiC after a 1750 °C / 10 min conventional furnace anneal are shown in Fig. 6. In this case, the boron has formed a considerable in-diffusion tail, which again is not desirable from a reliable device fabrication standpoint.

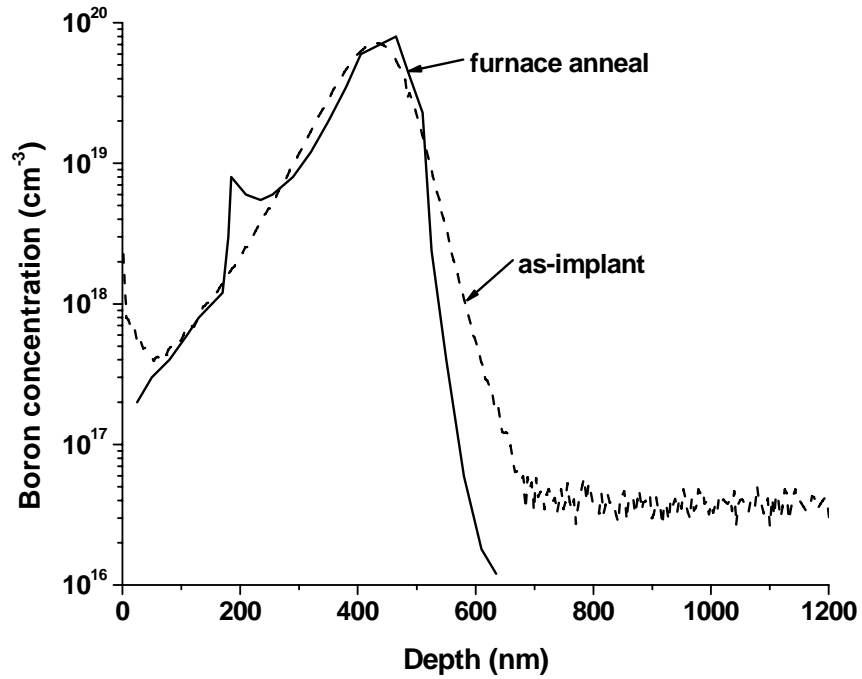


**Figure 5:** SIMS plots of a buried boron implant [M.V. Rao et al. J. App. Phys. **77**(6), 2749 (1995)], before and after furnace annealing at 1400 °C for 10 min. The implant was performed at 200 keV with a dose of  $1 \times 10^{15} \text{ cm}^{-2}$ .

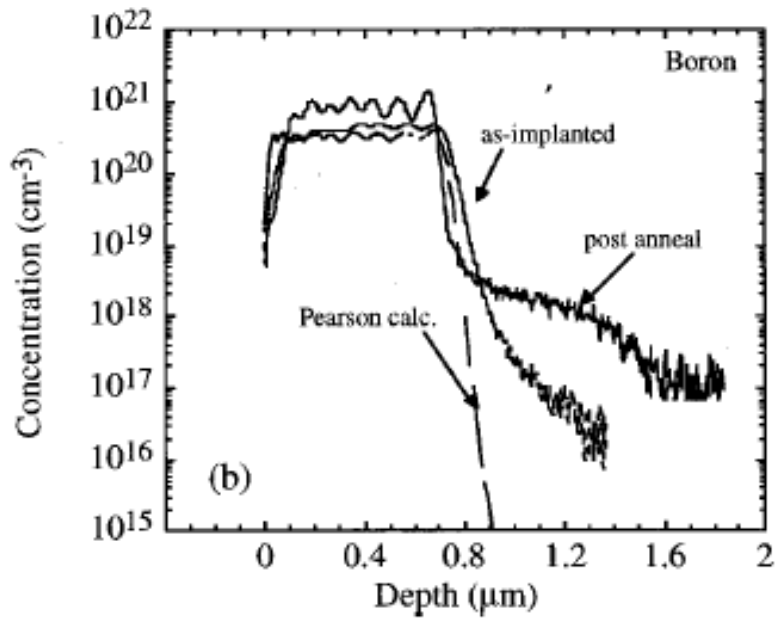


**Figure 6:** Diffusion tail observed in a multiple energy boron implant profile after a 10 min, 1750 °C anneal [S. Sheshadri et al. *App. Phys. Lett.* **72**(16), 2026 (1998)].

Furnace annealing for post-implantation annealing of SiC and GaN results in the materials being exposed for a long time at temperatures at which they are not thermally stable. Although the actual anneal time is as short as 10 min, the heating up time is an additional 10 min, and the cooling down time is even longer, depending on the size of the furnace and the thermal insulation. Therefore the total post-implantation process can last for > 1 hr. During the 1990's, magnetron driven single mode cavities were built at George Mason University for microwave annealing of implanted SiC<sup>46</sup>. This cavity-based system had a relatively high heating rate of 200 °C/min but was prone to arcing problems above 1600 °C. There have been attempts to anneal SiC using high-intensity flash lamps<sup>47</sup> or pulsed excimer lasers<sup>48,49</sup>. Due to its high bandgap of over 3 eV, SiC is transparent and absorbs very little in the visible spectrum. Hence to anneal SiC in RTP systems initially made for Si processing, the samples have to be placed on absorbing materials or into a graphite container, which obviously does not result in very efficient heat transfer. The initial experiments with pulsed excimer lasers showed that a high number of shots (in the range of 10000 – 100000) have to be performed to result in sufficient annealing of SiC layers<sup>50</sup>. This gives a duration of the actual anneal of around 10 min, which is very similar to furnace annealing. The activation efficiency of laser annealed aluminum implanted SiC was estimated to be about 0.1 %<sup>50</sup>, which indicates that laser annealing is not an effective annealing technique for post-implantation annealing of SiC. Since ultra-fast microwave annealing has the potential to solve many of the above-mentioned problems associated with conventional annealing of ion-implanted SiC, in this work, the microwave annealing of SiC is pursued.

## **2.2. Uncapped microwave annealing**

### **2.2.1 Annealing in an uncontrolled (air) ambient**

#### **2.2.1.1 Implantation and annealing schedules**

Initially, microwave annealing of N, Al and B implanted 4H- and 6H-SiC was conducted in an uncontrolled (air) ambient<sup>51</sup>. In this study, for the single- and multiple-energy N<sup>+</sup> implantations were performed into 3.5° off-axis (0001)- oriented Si-face p-type ( $5 \times 10^{17} \text{ cm}^{-3}$ ) bulk 6H-SiC crystals, as well as p-type ( $5 \times 10^{15} \text{ cm}^{-3}$ ) epitaxial layers grown on bulk 6H-SiC substrates. Nitrogen implants were performed at both room temperature (RT) and 700 °C. Single-energy (50 keV) N<sup>+</sup>-implants were performed for an implant dose of  $3.1 \times 10^{15} \text{ cm}^{-2}$ . Two multiple-energy N<sup>+</sup>-implants were performed, one in the energy range (15-250 keV) and another deeper implant in the energy range (50 keV – 4 MeV). The total implant doses were  $2.7 \times 10^{15} \text{ cm}^{-2}$  and  $1.57 \times 10^{15} \text{ cm}^{-2}$ , respectively. Multiple-energy implants were designed to obtain uniform doping concentrations. Multiple-energy (25 – 200 keV) Al<sup>+</sup>-implantations were performed (at 600 °C) into a semi-insulating on-axis 4H-SiC wafer. The total implant dose was  $2.7 \times 10^{15} \text{ cm}^{-2}$ . Three different boron implants, (a) 50 keV /  $8.8 \times 10^{14} \text{ cm}^{-2}$  (b) 200 keV /  $1 \times 10^{15} \text{ cm}^{-2}$  and (c) 1 MeV /  $2 \times 10^{15} \text{ cm}^{-2}$  B<sup>+</sup>-implants were performed into n-type epilayers grown on 6H-SiC substrate. The B<sup>+</sup> implantations were all performed at 700 °C. In air, in the temperature range 1570 – 1970 °C for a duration of 10- 35 s, the samples were annealed using a SiC proximity cap to suppress Si sublimation during annealing. For comparison, results of samples cut from the same wafers, which were subjected to conventional furnace annealing were used. The furnace annealing was performed by

Jason Gardner, past student at GMU. Conventional anneals were performed in a ceramic processing furnace, in the temperature range 1400 – 1600 °C for a duration of 10 – 15 min. The conventional anneals were performed at a pressure of 1 atm in argon ambient.

### **2.2.1.2 Surface morphology**

The surface morphology of the aluminum and nitrogen implanted SiC samples before and after microwave annealing was examined using atomic force microscopy (AFM) and field-emission scanning electron microscopy (FESEM). AFM images of Al-implanted 4H-SiC samples, annealed at 1570 °C/10 s and 1770 °C/10 s are shown in Figs. 7(a) and 7(b), respectively. For comparison an AFM image of a furnace annealed sample (1500 °C / 15 min) is shown in Fig. 7(c). Figure 8 shows a plot of the root mean square (RMS) roughness extracted from the AFM images as a function of annealing temperature for 10 – 35 s anneals on Al<sup>+</sup>-implanted SiC. Figure 9 shows FESEM images for an Al<sup>+</sup>-implanted furnace annealed sample and a microwave annealed sample. From Fig. 8, it can be seen that the RMS roughness for the microwave annealed samples, except for annealing temperatures  $\geq 1920$  °C, is much smaller than the 6 nm roughness observed in 1500 °C/ 15 min. furnace annealed sample. This result can be attributed to the short duration of the microwave annealing (~ 10-35 s) compared to the furnace annealing (~15 min) and also to the fast temperature rise and fall times of the microwave annealing. A lower surface roughness directly relates to an increase in the reliability in processing of sub-micron devices. Also, in the furnace annealed samples, continuous long furrows running in one direction across the sample surface can be noticed. These furrows are

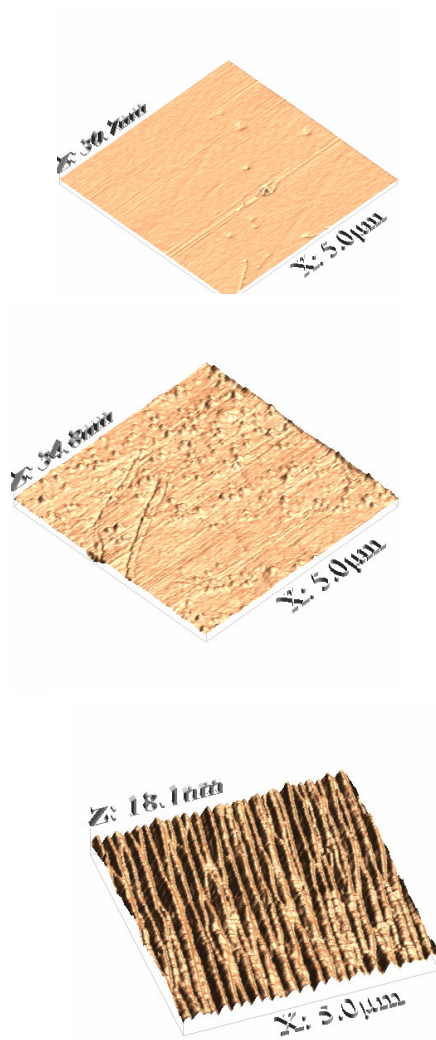


**Figure 7:** Atomic force microscope images of Al<sup>+</sup>-implanted 4H-SiC samples, (a) microwave annealed at 1570 °C for 10 s, (b) microwave annealed at 1770 °C for 10 s, and (c) furnace annealed at 1500 °C for 15 min.

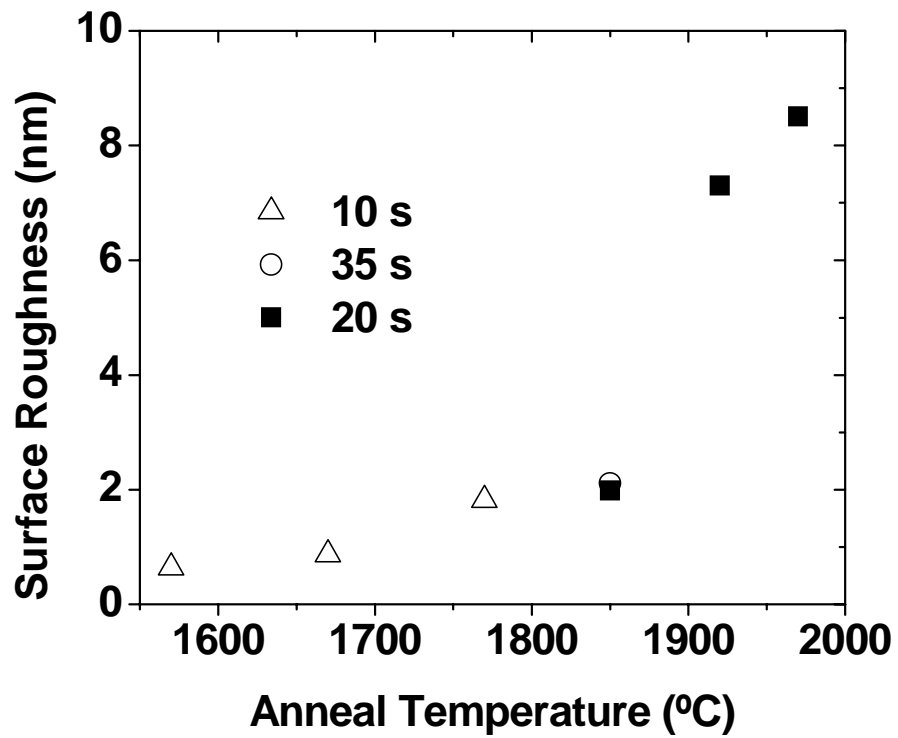
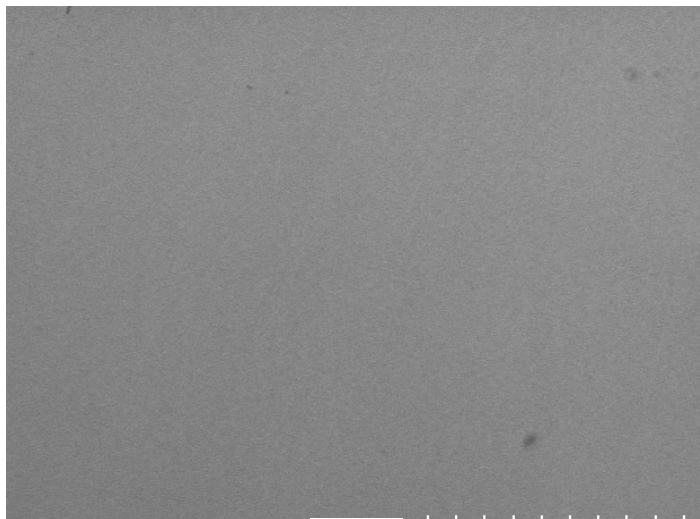
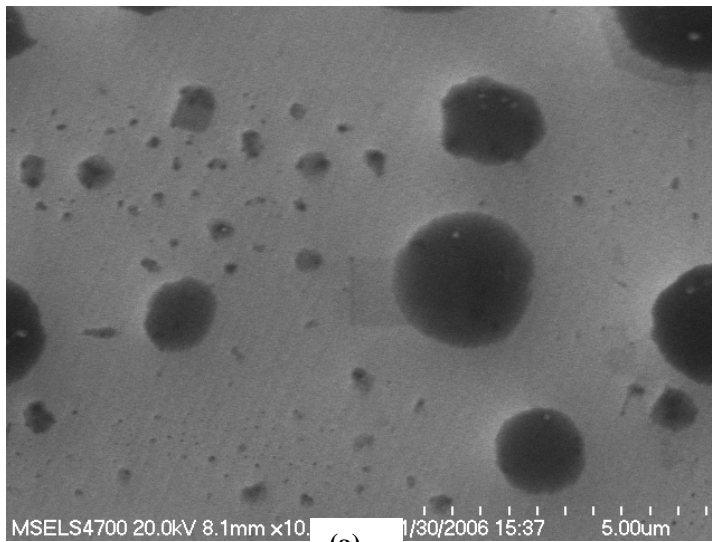


**Figure 8:** Plot of the root mean square (RMS) roughness extracted from the AFM images as a function of annealing temperature for 10 s – 35 s anneals for implanted SiC.



(b)

**Figure 9:** FE-SEM images of (a) 1500 °C / 15 min furnace annealed 4H-SiC sample and (b) 1770 °C / 10 s microwave annealed 4H-SiC sample.

supposed to be caused by the thermal desorption of species such as Si, SiC<sub>2</sub>, Si<sub>2</sub>C, etc<sup>40,43</sup>. In the case of the microwave annealed samples, these furrows show up only in the samples annealed at temperatures > 1770 °C. Even then, for microwave anneals performed at ≤ 1870 °C, the heights of the furrows are much smaller compared to the furnace annealed samples. However, the microwave anneals performed at the higher temperatures, 1920 °C, and 1970 °C do show a marked increase in surface roughness (Fig. 4). Also, the morphology of the furrows in microwave annealed samples is similar to the furnace annealed samples. Therefore, protection of the SiC surface with a graphite cap may be required for high temperature (> 1900 °C) microwave annealing in air.

In the FE-SEM images, presented in Fig. 9, the 1770 °C/10 s microwave annealed sample appears almost featureless, whereas, for the furnace annealed sample (annealed at 1500 °C for 15 min), the presence of the furrows can be clearly seen. In addition, secondary defects such as etch pits, which did not show up in the AFM images can be noticed in the SEM image of the furnace annealed sample. Therefore in light of all this evidence, it can be stated that the rapid solid-state microwave annealing technique leads to a smoother surface with much fewer annealing generated defects compared to the conventional furnace annealing.

### **2.2.1.3 Surface chemistry study**

Since the solid-state microwave (SSM) annealing of this work was performed in air, it is important to study the thermal oxide growth on the SiC surface. AES sputter profiling was used to study the composition of the oxide layer and variation of oxide

thickness with the annealing temperature. The samples used in this study were all virgin (un-implanted) n-type bulk 4H-SiC.

The oxide growth on two different SiC sample configurations was examined. In one case, the sample face was directly exposed to air. In another case, the sample to be studied was placed face down on another virgin SiC sample to mimic the proximity cap configuration used during post-implant annealing. A typical Auger sputter profile is shown in Fig. 10. The variation of oxide thickness with increasing temperature for the two sample configurations mentioned above is shown in Fig. 11. Upon performing Arrhenius fits for the data, the activation energy for SiC oxidation for both sample configurations was found to be similar (4.48 eV for the direct exposure to air, and 4.17 eV for the proximity cap configuration). These values are in general agreement with the values reported<sup>52,53</sup> earlier in the literature for parabolic SiC oxidation, which means that the oxidation rate is limited by the diffusion of the oxidizing species through the oxide film<sup>54</sup>. Propensity for oxidation at a given temperature is less for the proximity cap configuration resulting in shifting of the oxidation curve towards higher temperatures. This behavior is believed to be due to (a) increased partial pressure of Si- and C-containing species (due to sublimation from the surface of the capping sample) and (b) reduced oxygen partial pressure for the proximity cap configuration resulting in a reduced oxide growth rate. Thus, placing the sample in a proximity cap configuration during

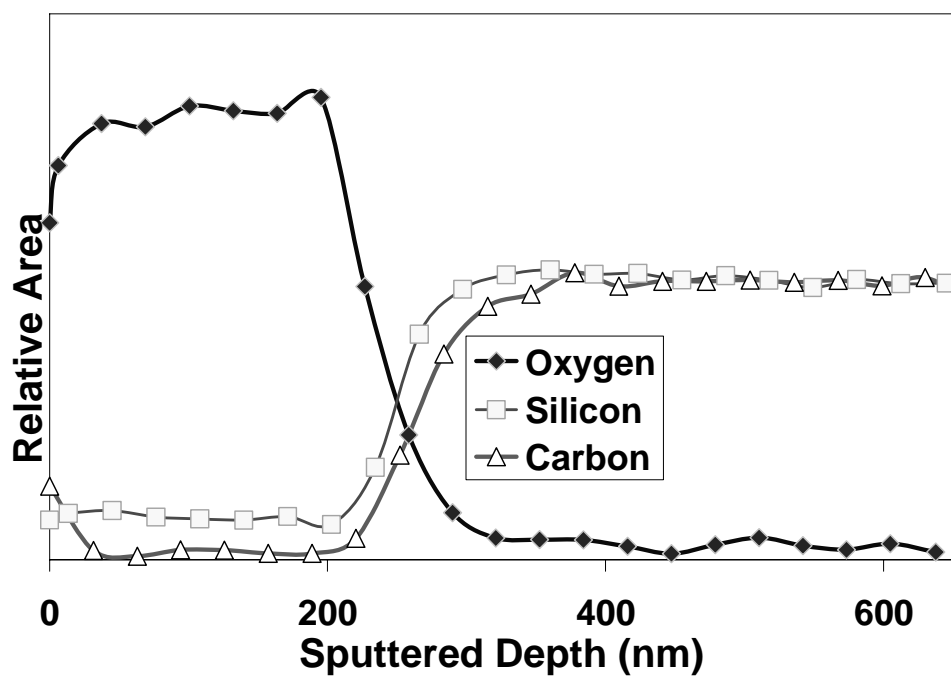


**Figure 10:** A typical Auger sputter profile showing the spatial variation of the elemental constituents of the silicon oxide film formed during the microwave annealing at 1820 °C.

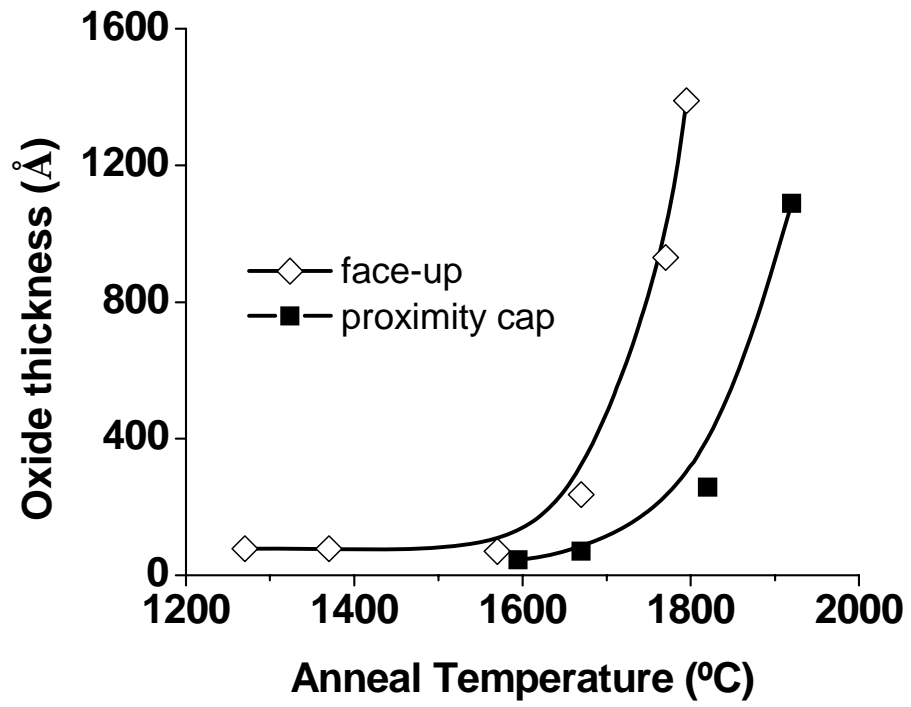


**Figure 11:** The variation of oxide thickness as a function of annealing temperature for the proximity cap and the face-up (direct exposure) sample configurations.

post-implant annealing has the added advantage of suppressing sublimation from implanted sample and reducing the thickness of the unintentional thermally grown oxide layer on this sample.

#### **2.2.1.4 Thermal stability of Boron implanted SiC**

It is well known that dopants such as N, Al and P are thermally stable in SiC. No redistribution of these impurities was observed even in long duration conventional furnace anneals performed up to 1700 °C<sup>55,56</sup>. On the other hand, the boron implant is known to redistribute in SiC even for low-temperature annealing<sup>57,58</sup>. The small atomic size of boron resulting in a high transient enhanced diffusion (TED) is believed to be responsible for this behavior. In this work, SIMS measurements were performed to study the effect of microwave annealing on shallow (50 keV) as well as deep (200 keV, 1 MeV) boron implant depth profiles in SiC. The SIMS depth profiles performed for 50keV, 200 keV and 1 MeV B<sup>+</sup> implantations, before and after 1670 °C/10 s microwave annealing are shown in Figs. 12,13, and 14 respectively. For comparison, the depth profile obtained for the 200 keV boron implant subjected to a 1400 °C/10 min furnace annealing is also shown in Fig. 13. For the 50 keV boron implant (Fig. 12), the 1670 °C / 10 s microwave annealing resulted in a significant out-diffusion of boron from the SiC surface. However, for the 200 keV and 1 MeV boron implants, 1670 °C / 10 s microwave annealing (Figs. 13, 14) did not result in any noticeable boron redistribution. In Fig. 13, for both microwave annealing and furnace annealing, the boron implant formed an out-diffusion front, probably caused by the segregation of boron towards ~ 0.7 R<sub>p</sub>, the depth

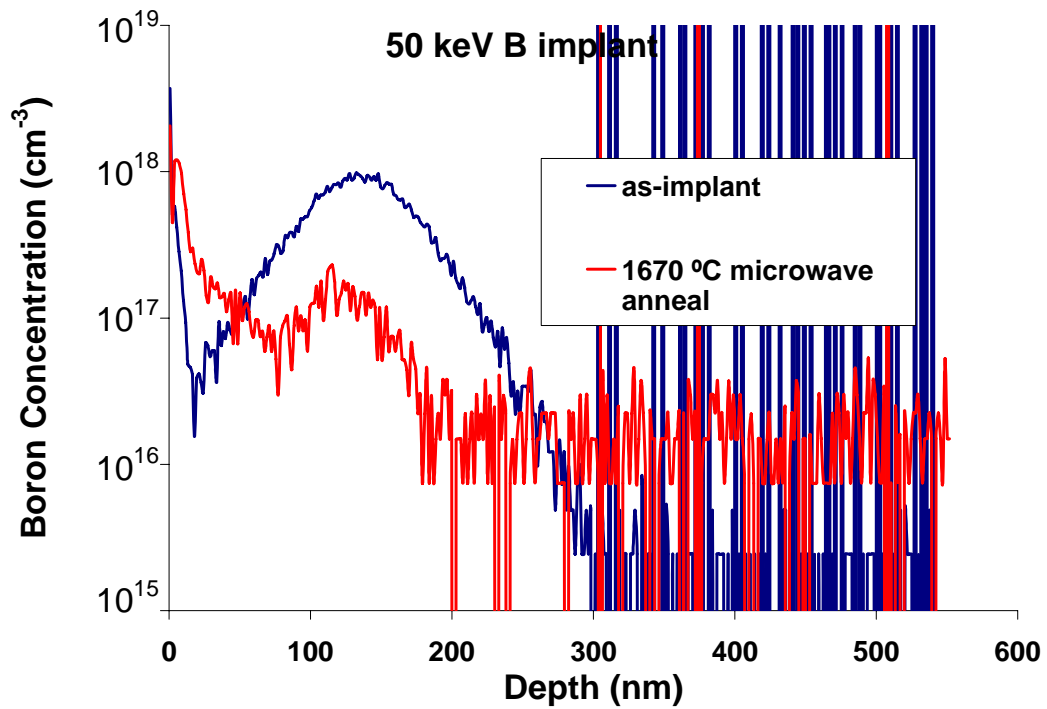


**Figure 12:** SIMS depth profile of a 50 keV /  $8.8 \times 10^{14} \text{ cm}^{-2}$  Boron implant before and after microwave annealing at 1670 °C for 10 s. A significant out-diffusion of boron is observed resulting in an overall loss of boron from the SiC surface.

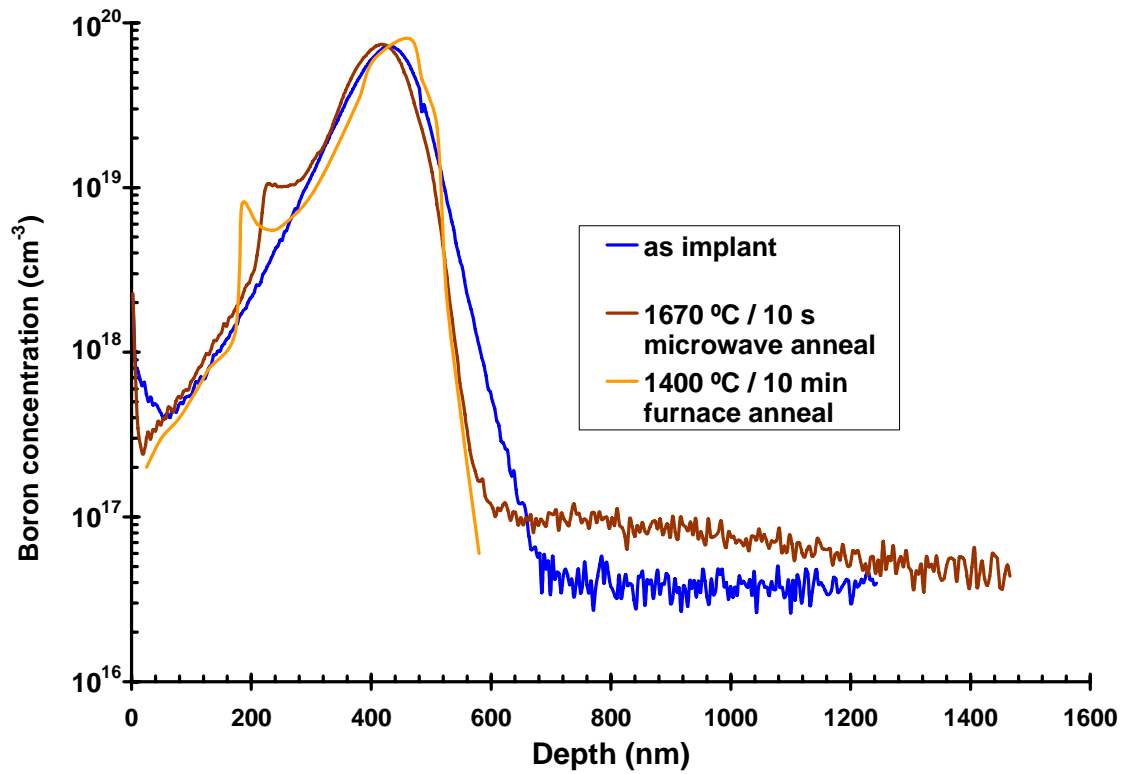


**Figure 13:** SIMS depth profiles for 200 keV /  $1 \times 10^{15}$  cm<sup>-2</sup> B<sup>+</sup> implantation before and after 1670 °C/10 s microwave annealing and 1400 °C / 10 min furnace annealing.

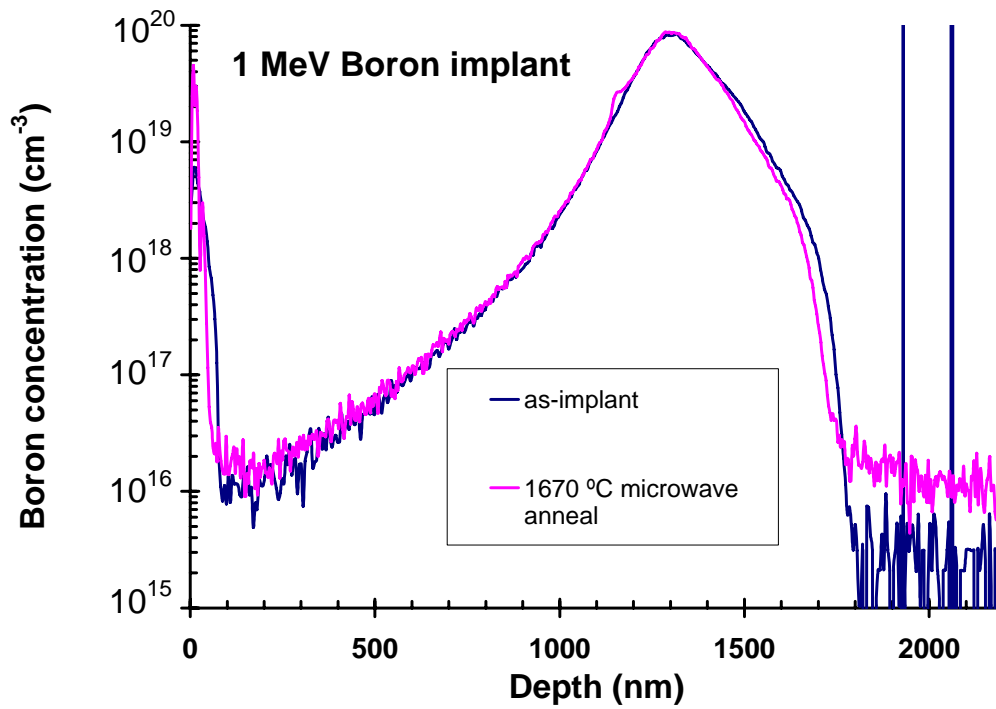


**Figure 14:** SIMS depth profile of a 1 MeV /  $2 \times 10^{15} \text{ cm}^{-2}$  Boron implant before and after microwave annealing at 1670 °C for 10 s.

where implant lattice damage is at its maximum. This is caused by the lattice strain at this location. A similar feature was observed in the B- depth profiles of  $1 \text{ MeV}/ 2 \times 10^{15} \text{ cm}^{-2}$  B for  $1670 \text{ }^\circ\text{C} / 10 \text{ s}$  microwave annealing. Out-diffusion of the boron is less for the microwave annealing compared to the furnace annealing even though the microwave annealing was performed at a temperature  $270 \text{ }^\circ\text{C}$  higher than the furnace annealing. This again establishes the attractiveness of ultra-fast solid-state microwave annealing compared to the furnace annealing, which has much slower heating and cooling rates. Only a small degree of in-diffusion of the boron implant is observed at the implant tail after microwave annealing. Thus the ultra-fast microwave annealing is effective in maintaining the integrity of buried boron implant profiles, but a significant boron out-diffusion is still observed for  $10 \text{ s}$  microwave annealing at  $1670 \text{ }^\circ\text{C}$ . Possibly capping the boron implanted SiC surface with a layer of graphite might minimize the extent of boron out- diffusion.

#### **2.2.1.5 Rutherford back-scattering (RBS) study**

RBS spectra on  $50 \text{ keV}/3.1 \times 10^{15} \text{ cm}^{-2} \text{ N}^+$ -implanted material, before and after  $1770 \text{ }^\circ\text{C}/25 \text{ s}$  microwave annealing and  $1600 \text{ }^\circ\text{C}/15 \text{ min}$  conventional furnace annealing, are shown in Fig. 15. It clearly demonstrates that the lattice quality of microwave-annealed material is better than the furnace annealed material. The results show that the as-implanted sample has the highest level of lattice damage, with the backscattering signal reaching 14% of that of amorphous or randomly oriented SiC. The reason for such a low scattering yield in the as-implanted sample, even for such a high implant dose is the

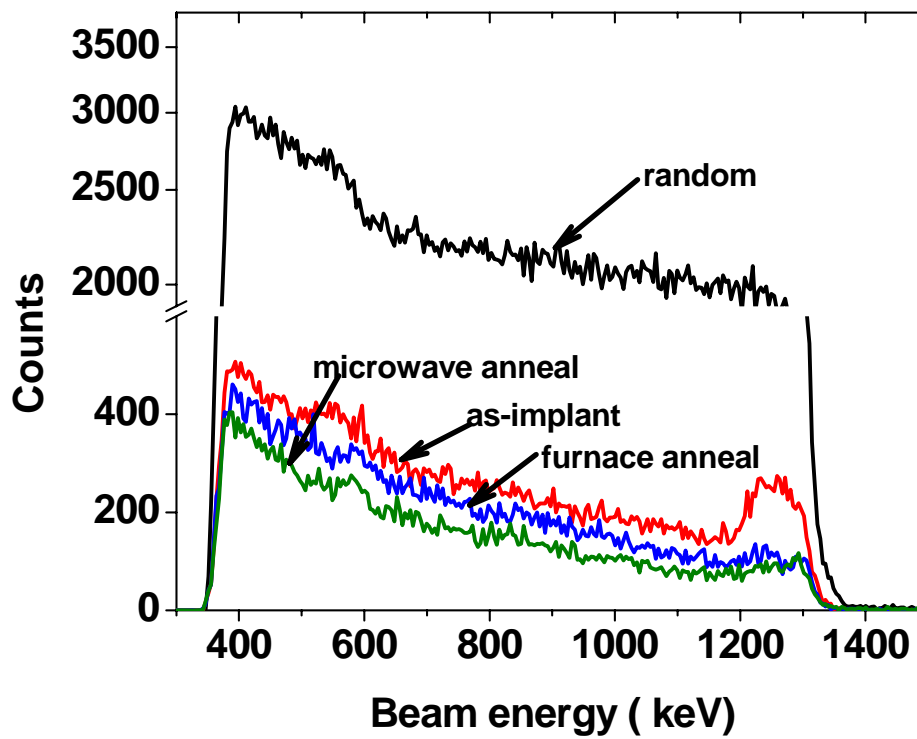


**Figure 15:** RBS spectra on 50 keV/ $3.1 \times 10^{15}$  cm<sup>-2</sup> N<sup>+</sup>-implanted material, before and after 1770 °C/25 s microwave annealing and 1600 °C/15 min conventional furnace annealing.

elevated temperature at which the implantation was performed. Elevated temperature implantation is known to promote a certain amount of in-situ dynamic annealing during the implantation process. The implant damage is present in the 0-200 nm depth range. The microwave-annealed sample shows the lowest (3.1%) amount of backscattering, corresponding to the least crystal damage. The furnace annealed sample shows slightly higher damage than the microwave annealed sample for depths corresponding to 100 nm - 200 nm. The increased backscattering signals for the as-implanted and the furnace annealed samples for depths greater than 200 nm is due to de-channeling of the  $\text{He}^{++}$  ion beam caused by damage in the 0-200 nm depth range.

#### **2.2.1.6. Electrical Characteristics of Nitrogen Implanted SiC**

Electrical characteristics of the nitrogen implanted/annealed 6H-SiC material, obtained by van der Pauw Hall measurements at room temperature (RT) are given in Table III. The implant energies and the doses pertaining to the samples are also included in the table. For comparison, the results on SiC samples annealed by a conventional Brew ceramic furnace are also included. The electrical activation ( $\Phi$ ) given in Table III is the ratio of measured sheet carrier concentration at RT to the total implant dose. It is well known that due to a high donor ionization energy ( $\sim 70$  meV - 80 meV) in SiC, the measured carrier concentration at RT doesn't represent the actual substitutional activation of the implant<sup>56</sup>.

By comparing the results of rapid SSM with that of furnace annealing for the 15 keV – 280 keV multiple energy  $\text{N}^+$ -implant, it can be stated that the implantation

**Table III:** Electrical characteristics of single- and multiple- energy nitrogen implanted 6H-SiC annealed by solid-state microwave (SSM) annealing and conventional furnace annealing.

Anneal type	Implant Energy	Implant temp (°C)	Total Dose (cm <sup>-2</sup> )	Annealing Temp /time	Sheet resistance (Ω/□)	Sheet carrier concentration (cm <sup>-2</sup> )	Φ (%)	Carrier Hall mobility (cm <sup>2</sup> /Vs)
furnace	50 keV	700	3.1 x 10 <sup>15</sup>	1500°C/ 15 min	2390	1.24x 10 <sup>14</sup>	4	21.1
furnace	50 keV	700	3.1x 10 <sup>15</sup>	1600°C/ 15 min	1660	1.83x 10 <sup>14</sup>	6	14
SSM	50 keV	700	3.1x 10 <sup>15</sup>	1770°C/ 25s	967	4.84x 10 <sup>14</sup>	15.6	13.4
furnace	15-280 keV	RT	1.35x 10 <sup>15</sup>	1600°C/ 15 min	333	4.1 x 10 <sup>14</sup>	30.4	46
SSM	15-280 keV	RT	1.35x 10 <sup>15</sup>	1620°C/ 10s	666	2.079 x 10 <sup>14</sup>	15.3	45.1
furnace	15-280 keV	700	2.7x 10 <sup>15</sup>	1600°C/ 15 min	290	8.6 x 10 <sup>14</sup>	31.2	25
SSM	15-280 keV	700	2.7x 10 <sup>15</sup>	1620°C/ 10 s	407	9.8 x 10 <sup>14</sup>	36.2	15.7
furnace	50keV-4 MeV	700	1.57x 10 <sup>15</sup>	1600°C/ 15 min	211	5.96 x 10 <sup>14</sup>	38	50
SSM	50keV-4 MeV	700	1.57x 10 <sup>15</sup>	1570°C/ 10 s	695	2.58 x 10 <sup>14</sup>	16.4	35
SSM	50keV-4 MeV	700	1.57x 10 <sup>15</sup>	1670°C/ 10 s	391	3.3 x 10 <sup>14</sup>	21	48.5

temperature plays an important role in the dopant activation process of rapid SSM annealing. For a 1620 °C/10 s SSM annealing the sheet resistance is closer to that of furnace annealing for the elevated temperature implantation, whereas, it is only 50% of the corresponding furnace annealing value for the RT implantation. However, the sheet resistance values can be improved by increasing the annealing temperature and duration. For the 50 keV – 4 MeV multiple energy N-implant also a higher SSM annealing temperature/time than shown in Table III are required for removing the lattice damage and activating the N-implant. For the single energy (50 keV) N-implanted sample, SSM annealing at 1770 °C for 25 s yielded a much lower sheet resistance (966  $\Omega/\square$ ) compared to the value (1666  $\Omega/\square$ ) for the furnace annealing at 1600 °C for 15 min. In spite of a higher sheet carrier concentration in the microwave annealed sample, the carrier mobility is similar to that of the furnace annealing indicating that the lattice damage is much smaller in the microwave-annealed sample. This observation corroborates with the RBS results shown in Fig. 8, which indeed show a smaller lattice damage for the microwave-annealed sample.

#### **2.2.1.7. Electrical Characteristics of Aluminum implanted SiC**

For the 600 °C Al<sup>+</sup> -implantation in 4H-SiC, the electrical characteristics measured at RT, by the van der Pauw Hall technique, are given in Table IV. The percentage RT activation,  $\Phi$  in Table IV is the ratio of net hole sheet concentration measured at RT to the total Al implant dose. It should be noted that the apparently smaller RT carrier activations measured for Al in comparison with N are a manifestation

**Table IV:** Electrical characteristics of solid-state microwave annealed, 25 – 200 keV multiple energy Al<sup>+</sup> implanted SiC for a total implant dose of  $2.7 \times 10^{15} \text{ cm}^{-2}$ . The implant temperature is 600 °C.

Annealing Temp/time (°C/s)	Sheet resistance ( $\Omega/\square$ )	Sheet carrier concentration ( $\text{cm}^{-2}$ )	$\Phi$ (%)	Hole mobility ( $\text{cm}^2/\text{Vs}$ )
1670 / 10	$1.7 \times 10^5$	$1.05 \times 10^{12}$	0.0004	35
1770 / 10	$1.15 \times 10^5$	$1.95 \times 10^{12}$	0.07	28
1800 / 30	$11.2 \times 10^4$	$1.97 \times 10^{12}$	0.07	28.3
1850 / 35	$7 \times 10^3$	$7.3 \times 10^{13}$	2.7	12
1870 / 30	$3.5 \times 10^4$	$1.5 \times 10^{13}$	0.5	11.9
1920 / 20	$15.55 \times 10^4$	$1.18 \times 10^{12}$	0.0004	34
1970 / 20	$33.81 \times 10^4$	$6.67 \times 10^{11}$	0.0005	27.7

of the much higher carrier ionization energy for the Al acceptor (~200 meV) compared to the N donor (~70 meV) in 4H-SiC. It can be observed from Table IV that even though the sheet resistance decreases with increasing annealing temperature, until a temperature > 1800 °C is reached, the carrier activation remains below 0.1% for the 10 s anneals. For 1850 °C/35 s anneal we measured a maximum  $\Phi$  of 2.7%. Also, the lowest sheet resistance (7 k $\Omega/\square$ ) is measured for this particular anneal. At the time this measurement was performed, the combination of this high activation and low sheet resistance were among the best reported at that time. Negoro et. al.<sup>59</sup>(for an implant concentration  $1.5 \times 10^{21} \text{ cm}^{-3}$  to a depth of 0.2  $\mu\text{m}$ ) have reported a lower sheet resistance of 2.9 k $\Omega/\square$  and an activation  $\Phi$  of 2%, for an anneal time of 30 min, at 1800 °C. However, they observed that their results degrade with an increasing annealing time which is an indication that the increased p- type conductivity that they report may be related to the hopping conduction<sup>60</sup> contributed by implant generated defects in SiC, which are known to exhibit p-type behavior, rather than by the chemical effect of substitutional Al. In hopping conduction, as the annealing duration increases, the implant-generated defects are annealed and a drop in conductivity is observed. Also, at dopant concentrations in excess of  $10^{21} \text{ cm}^{-3}$  in SiC, a Mott transition into a metallic phase (characterized by a very low mobility) has been observed in the literature<sup>61,62</sup>.

In Table IV, for the anneals performed at temperatures beyond 1900 °C, a precipitous drop in carrier activation, and a consequent step increase in the measured sheet resistance can be observed. Since all anneals in this exploratory study were performed in the air, we can attribute the reason for this trend to the increased propensity

for SiC oxidation at these high temperatures (See Fig. 11). As a result, a major proportion of the implanted layer is being converted to silicon oxide, thereby decreasing the implant dose in the remaining material. This interpretation of the results suggests that microwave annealing in an inert atmosphere such as xenon, argon or nitrogen is mandatory for high temperature anneals.

#### **2.2.1.8 Conclusions from uncapped microwave annealing of ion-implanted SiC in uncontrolled ambient**

Solid-state microwave annealing is an attractive method for rapid thermal annealing of implanted SiC. In this technique, temperatures as high as 2000 °C can be reached with a ramp-up rate of > 600 °C / s and a fall rate of 400 °C / s. The electrical characteristics and lattice quality of the microwave-annealed material are better than the values obtained for conventional furnace anneals. Due to the short annealing durations, the redistribution of implanted boron is reduced in the microwave-annealed samples. Based on the above results, it is worth re-emphasizing that post-implantation annealing at higher temperatures and shorter durations are necessary for achieving optimum structural as well as electrical material properties. In this study, due to annealing in air, the samples were oxidized, so an annealing chamber for performing anneals in an inert atmosphere is mandatory to prevent oxidation.

#### **2.2.2 Microwave annealing in a pure nitrogen atmosphere**

Promising lattice quality and electrical activation results were obtained, but, in the earlier work<sup>51</sup> anneals were performed in air, limiting the maximum annealing

temperature and the anneal time due to the growth of a thick ( $> 100$  nm) oxide layer during high-temperature ( $> 1850$  °C) annealing. The limitations in anneal temperature and time compromised the optimum electrical properties possible by the solid-state microwave annealing. In this work<sup>63</sup>, solid-state microwave annealing on phosphorus and aluminum ion-implanted 4H-SiC was performed in controlled inert atmospheres of N<sub>2</sub>, Ar, or Xe, to prevent surface oxidation of SiC. Phosphorus is the preferred n-type dopant in SiC because of its higher solubility limit in SiC than nitrogen, which can not be incorporated in excess of  $3 \times 10^{19}$  cm<sup>-3</sup> due to precipitation during post-implantation annealing<sup>54,64</sup>.

Annealing in an inert ambient solved the oxidation problem, allowing for high temperature ( $\sim 2100$  °C) annealing and yielding very low sheet resistances and very high carrier mobilities in implanted 4H-SiC. The principle aim of this work is studying the improvement in lattice structure and electrical characteristics with increasing annealing temperature for 5 – 60 s anneals.

### **2.2.2.1 Implantation and annealing schedules**

Multiple-energy Al<sup>+</sup> and P<sup>+</sup> implant schedules performed into semi-insulating (SI) 4H-SiC are given in Table V. The Al<sup>+</sup>- implant was performed into an on-axis wafer and the P<sup>+</sup>- implant was performed into an 8° off-axis wafer. The Al<sup>+</sup> and P<sup>+</sup>-implants were performed at 500 °C. The P<sup>+</sup>- and Al<sup>+</sup>-implants were designed to obtain a uniform

**Table V:** Implant schedules for microwave annealing in a pure nitrogen atmosphere

<b>Species</b>	<b>Implant Energy (keV)</b>	<b>Implant Dose (cm<sup>-2</sup>)</b>
Aluminum	10	$4.5 \times 10^{15}$
	25	$7 \times 10^{14}$
	40	$6.7 \times 10^{14}$
	100	$1.6 \times 10^{15}$
	200	$2 \times 10^{15}$
	325	$1.8 \times 10^{15}$
	400	$2.2 \times 10^{15}$
Phosphorus	10	$5 \times 10^{14}$
	20	$5 \times 10^{15}$
	60	$9 \times 10^{14}$
	100	$2.2 \times 10^{15}$
	200	$4.5 \times 10^{15}$

implant concentration of  $2 \times 10^{20} \text{ cm}^{-3}$  to a depth of  $\sim 0.3 \text{ }\mu\text{m}$  and  $0.5 \text{ }\mu\text{m}$ , respectively except at the surface. The lowest energy implant was designed to obtain a decade higher surface doping concentration than the rest of the depth to obtain a very low ohmic contact resistance.

In this work, annealing was mainly performed in a controlled atmosphere of 100% UHP grade nitrogen. In addition to nitrogen, microwave annealing was attempted in atmospheres of other inert gases such as helium, argon and xenon. However, these latter gases were found to ionize (generating arcing) due to the intense microwave field in the vicinity of the SiC sample.

The annealing temperatures ranged from  $1750 \text{ }^\circ\text{C}$  –  $2120 \text{ }^\circ\text{C}$  for the aluminum implanted samples. For the phosphorus implanted samples, the annealing temperatures ranged from  $1700 \text{ }^\circ\text{C}$  –  $1950 \text{ }^\circ\text{C}$ . The anneal durations for both aluminum and phosphorus implants varied from 5 s to 60 s.

#### **2.2.2.2 Atomic Force Microscopy (AFM) study of the surface morphology**

The RMS surface roughness extracted from  $5 \text{ }\mu\text{m} \times 5 \text{ }\mu\text{m}$  tapping mode AFM scans of microwave annealed  $\text{Al}^+$ - implanted samples are given in Table VI. The RMS roughness values for the  $1800 - 2050 \text{ }^\circ\text{C}$  anneals were in the range of 1 -2 nm. This is 2.1 times the surface roughness of the as-implanted sample (0.96 nm). Roughness increase in the microwave annealed samples is much lower than the values observed earlier for uncapped conventional furnace anneals (which show an increase in roughness of  $\sim 15$  times the as-implanted value)<sup>40,43</sup>. Roughness increase after uncapped microwave

**Table VI:** RMS Surface roughness extracted from tapping mode 5  $\mu\text{m}$  x 5  $\mu\text{m}$  AFM scans of  $\text{Al}^+$  - implanted SiC. The noise level in the measurements is measured to be 0.15 nm.

<b>Sample details</b>	<b>RMS surface roughness (nm)</b>
As-implant	0.96
1800 °C / 30 s	2.1
1950 °C / 30 s	1.7
2050 °C / 15 s	2
2050 °C / 30 s	1.4

annealing in this work is comparable to the surface roughness measured earlier after furnace annealing using a graphite<sup>65</sup> or AlN<sup>66</sup> cap. These results indicate the attractiveness of high-temperature short duration annealing.

In this study, no proximity capping was used. Due to this reason, the possibility of desorption of evaporated Si and C containing species back onto the implanted SiC, resulting in a wavy SiC surface (a mechanism known as step-bunching)<sup>67,68</sup> is minimal. A high surface roughness in conventionally annealed SiC is mainly due to the formation of furrows caused by the step-bunching effect. Getting a low surface roughness for short-duration high-temperature microwave annealing doesn't mean that there is no sublimation of SiC. As presented later in SIMS results, there is a substantial loss (~ 100 nm) of implanted-SiC with increasing (> 2000 °C) annealing temperature.

### **2.2.2.3 Annealed SiC surface chemical analysis using Auger electron spectroscopy (AES) and x-ray photoelectron spectroscopy (XPS)**

As observed earlier, microwave annealing on SiC at temperatures > 1850 °C for 15 s in an uncontrolled ambient (air) results in a significant (> 100 nm) oxide layer growth<sup>51</sup>. Though in this study<sup>63</sup>, the anneals were performed in a controlled inert environment, trace amount of oxygen present in the inert gasses may result in the formation of an oxide layer, because the annealing temperatures explored were very high (up to 2050 °C). High-temperature anneals in N<sub>2</sub> ambient may result in nitridation of SiC surface. Hence, SiC surface oxidation and nitridation were examined using AES sputter profiling and XPS. All the samples used in this AES and XPS study

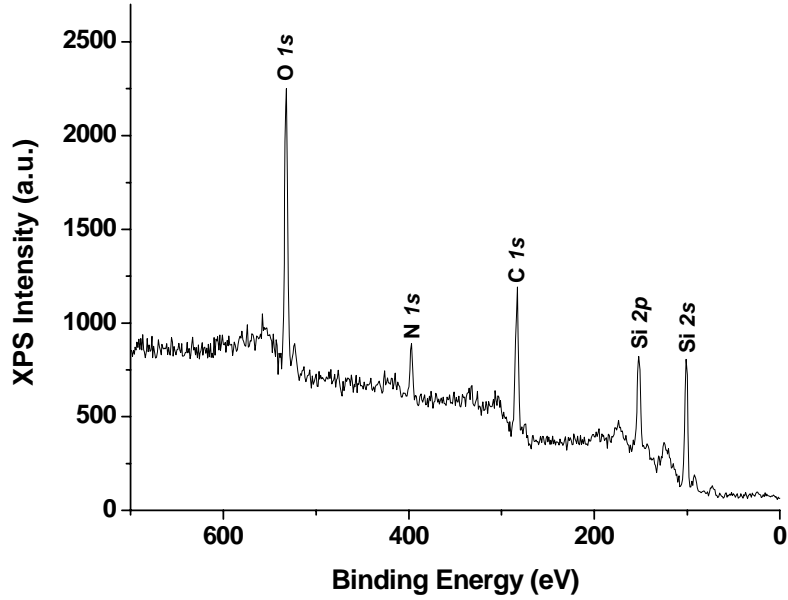


**Figure 16:** XPS survey scan for an 1800 °C / 15 s microwave annealed virgin 4H-SiC sample in a pure nitrogen atmosphere.

**Table VII:** Unintentionally grown oxide/nitride film thickness as a function of annealing temperature for 15 s microwave annealing in a pure nitrogen atmosphere.

Sample details	Film Thickness (Å)
1780	63
1800	33
1900	25
1950	45
2000	25

were virgin semi-insulating 4H-SiC subjected to heat treatment at different temperatures.

Figure 16 shows a typical XPS survey scan of an 1800 °C / 15 s annealed sample in N<sub>2</sub> ambient. The only elements detected in this survey scan are N, O, C, and Si. Detailed XPS scans indicated that the surface layer is made up of silicon oxide and silicon nitride. The thickness of this surface layer was measured using Auger sputter profiling. It can be seen from Table VII that the film thicknesses in the annealed samples ranged from 25 – 65 Å. As observed in case of XPS, the AES also indicated the presence of silicon, carbon, nitrogen and oxygen. Summarizing, the film thicknesses measured after microwave annealing in N<sub>2</sub> upto 2100 °C remained < 70 Å. This is a marked improvement from the earlier study, where the samples annealed in air at temperatures > 1850 °C resulted in oxide films of 1000 Å thickness.

#### **2.2.2.4 Investigation of surface sublimation and/or dopant redistribution**

It is known that both implanted P and Al are thermally stable in SiC. The SIMS measurements in this study were aimed at studying the thickness of implanted SiC layer lost during short-duration high-temperature microwave annealing. Figure 17 shows an overlay of Al implant depth profiles in as-implanted, 1800 °C / 15 s, 1950 °C / 15 s and 2100 °C / 15 s annealed samples. Depth profiles of the annealed samples were shifted to the right to align implant tail region of the annealed samples with that of the as-implanted sample. It is very clear that the implant tails have a good match indicating no significant in-diffusion of Al. Implant tail matching would not have been possible if Al had in-diffused during annealing. From Fig. 17, it is clear that < 20 nm of the implanted layer is

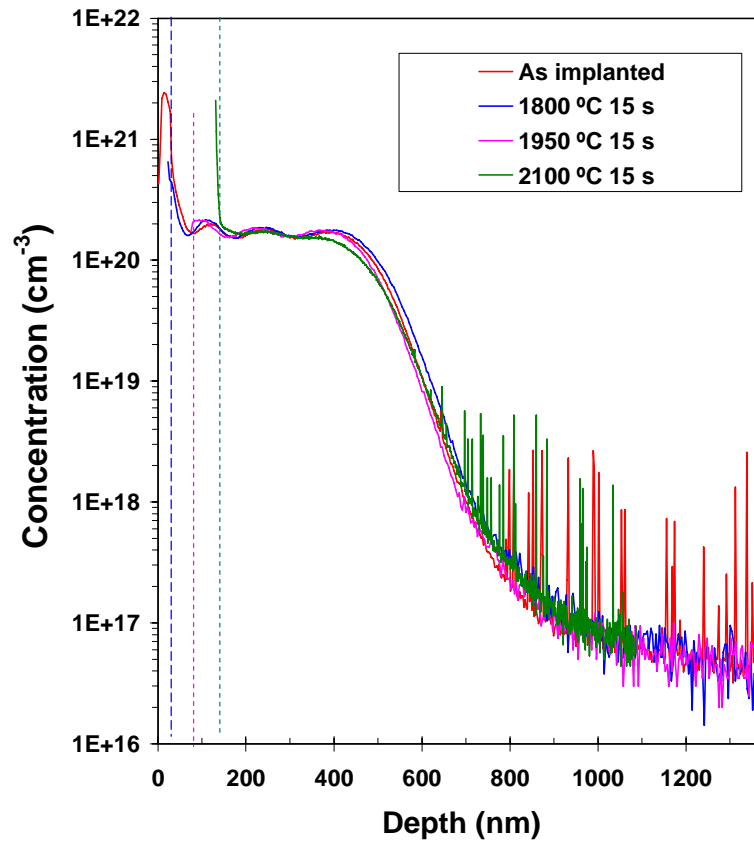


**Figure 17:** SIMS depth profiles for Al<sup>+</sup> - implanted SiC, microwave annealed at 1800, 1950 and 2100 °C for 15 s. The profiles were shifted to the right to align the implant tail region with the as-implanted sample. Vertical dotted lines indicate the amount of the implant that had sublimed after microwave annealing.

lost for the 1800 °C / 15 s annealed sample, whereas ~ 120 nm of the implanted layer has sublimed for the 2100 °C / 15 s annealed sample. Loss of implanted layer during annealing at these high temperatures is expected because no protective cap was used in this study. Hence, the use of a deposited graphite cap to protect the implanted layer surface for short duration microwave annealing at these high annealing temperatures seems mandatory for preserving implanted SiC. If the expected loss of implanted layer is factored-in during the design of implanted profiles itself, one may be able to use microwave annealing without any cap.

#### **2.2.2.5 Rutherford backscattering channeling (RBS-C) study**

The RBS-C spectra were recorded from the Al<sup>+</sup> -implanted SiC samples, before and after microwave annealing. The aligned RBS spectra acquired at a detector angle of 160° was used to study the extent of lattice damage in the samples before and after microwave annealing. Aligned (parallel to the c-axis) RBS-C spectra of the Al<sup>+</sup> implanted SiC, before and after 2050 °C / 15 s microwave annealing are shown in Fig. 18. For comparison, aligned RBS-C spectra from a virgin SiC sample and a RBS-C spectrum from a randomly aligned SiC sample are also presented in Fig. 18.

In spite of the high implant dose employed, amorphization of the substrate was avoided due to the elevated implantation temperature (500 °C). The microwave-annealed sample exhibits a scattering yield near the virgin level. This indicates that the high-temperature microwave annealing is very effective in restoring the crystallinity of the implanted SiC. RBS spectra were also collected (not shown) at a grazing detector angle

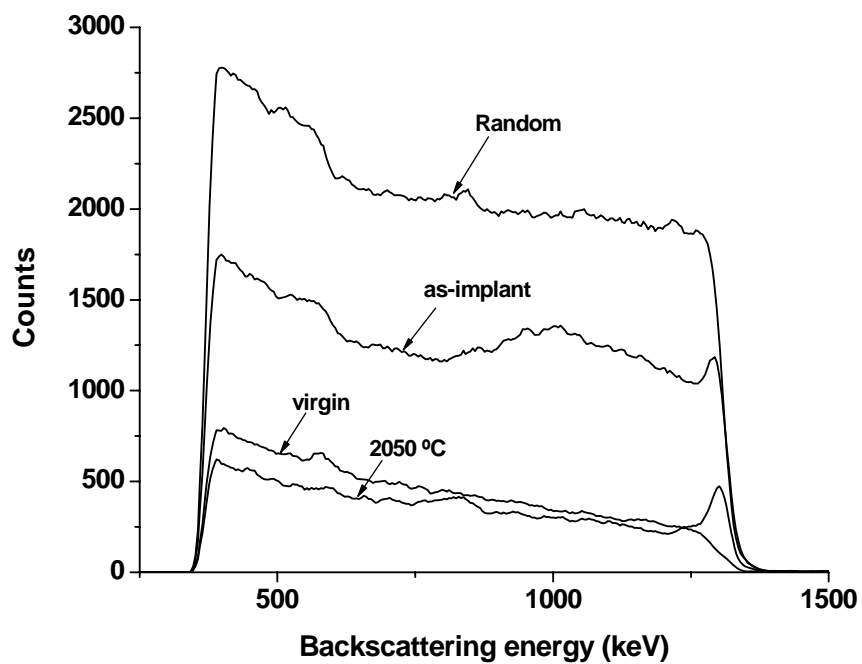


**Figure 18:** RBS-C aligned spectra for a virgin 4H-SiC sample, an Al<sup>+</sup> as-implanted sample, and a microwave annealed sample at 2050 °C / 15 s. RBS-C spectrum for a randomly aligned SiC sample is also shown for reference.

(110°) to study the impact of the high-temperature microwave annealing on SiC surface stoichiometry.

The analysis of the data collected using both the normal and grazing angle RBS geometries indicated a near perfect (1:1) Si:C ratio from the surface to a depth of ~ 100 nm in the as-implanted as well as all the the microwave annealed samples. This proves that the short-duration, high-temperature microwave annealing preserves the surface stoichiometry of the SiC surface and prevents the formation of C-rich surface layers.

#### **2.2.2.6 Electrical characteristics of aluminum implanted 4H-SiC**

The sheet resistance ( $R_s$ ) is an important parameter to evaluate the electrical characteristics of an implanted SiC layer, because a low  $R_s$  can be obtained only if both the sheet carrier concentration and carrier mobility are high. Hence, in this work, the room temperature (RT)  $R_s$  is presented as the prime figure of merit of electrical characteristics of implanted SiC. Variation of the sheet resistance ( $R_s$ ) of  $Al^+$  -implanted SiC, as a function of the microwave annealing temperature in the range 1800 °C – 2120 °C, for anneal durations of 15 s and 30 s, are shown in Fig. 19. Variation of the hole mobility and the sheet hole concentration ( $p_s$ ) for 15 s anneals, as a function of the annealing temperature are shown in Fig. 20.

It is clearly seen from Fig. 19 that there is a critical/threshold temperature of 1950 °C above which very low sheet resistances ( $< 5 \text{ k}\Omega/\square$ ) are obtained. Microwave annealing at 2100 °C for 15 s yields a sheet resistance of  $2.4 \text{ k}\Omega/\square$ . This is among the lowest sheet resistances reported to date for chemically active, acceptor implanted p-type

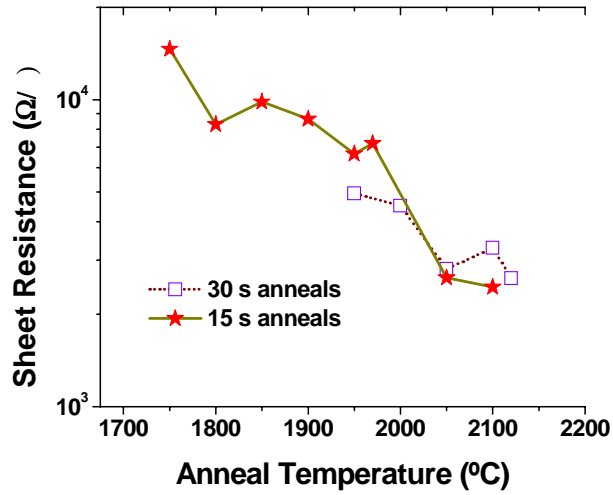


**Figure 19:** Plot of sheet resistance as a function of annealing temperature in  $\text{Al}^+$  - implanted 4H-SiC, for 15s and 30 s microwave anneals.

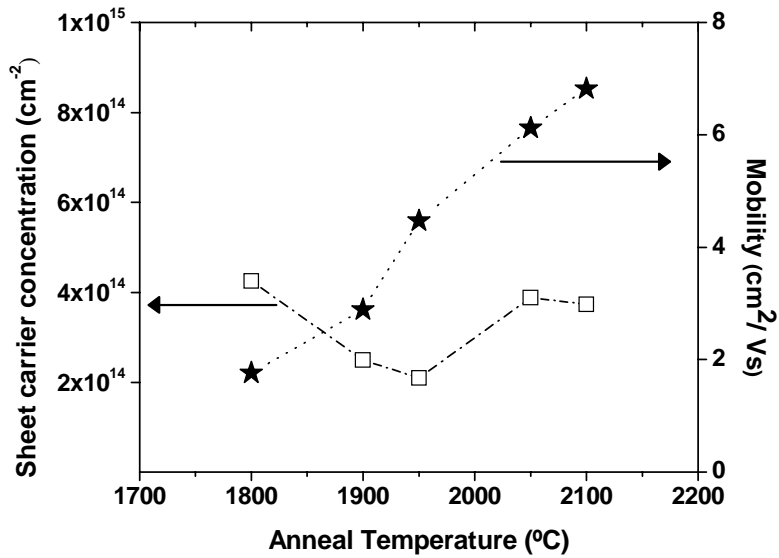


**Figure 20:** Plot of sheet carrier concentration and hole mobility, as a function of the annealing temperature in  $\text{Al}^+$  -implanted SiC for 15 s microwave anneals.

SiC. With increasing annealing temperature, the hole mobility (see Fig. 20) is also found to increase along with a corresponding increase in the sheet hole concentration. The increase in the hole mobility with the increasing carrier concentration is an indication that the implantation induced defects are annealed out effectively by the high-temperature microwave annealing. This means that the RT hole mobility in the acceptor implanted material is not primarily limited by ionized impurity scattering (since very few Al atoms are ionized at RT) but rather by defects (residual implantation damage as well as substrate growth-related) in the material. The defect concentration in the implanted material continuously decreases with increasing annealing temperature resulting in an increasing hole mobility.

In the past, extremely high dose ( $> 10^{21} \text{ cm}^{-3}$ ) Al<sup>+</sup>- implantation<sup>69</sup>, with or without flash-lamp annealing<sup>70</sup>, resulted in extremely low resistive layers of SiC. However, the hole mobilities obtained in these layers were extremely low ( $\sim 0.4 \text{ cm}^2 / \text{V.s}$ ), implying that either a Mott transition into a metallic phase had occurred, or that the low-sheet resistivity reported was most likely contributed by the implant-generated high concentration defects, through the so called “hopping conduction” mechanism<sup>71</sup>. In other words, the electrical conduction in these studies was most probably not due to chemically active substitutional dopant activation as observed in the present work.

To elucidate the dependence of electrical characteristics on the anneal time, variation of  $R_s$  and  $p_s$  as a function of annealing time in the range 5 s – 60 s is shown in Fig. 21 for an annealing temperature of 1950 °C. There is a drop in the sheet resistance and a corresponding increase in sheet carrier concentration, with an increasing annealing

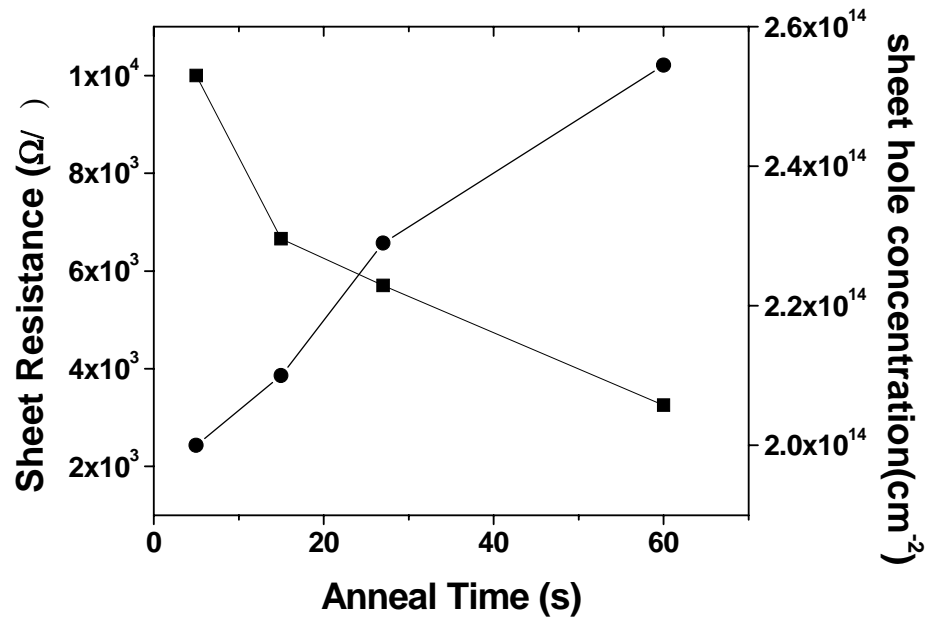


**Figure 21:** Plot of sheet resistance and sheet hole concentration, as a function of annealing time in  $\text{Al}^+$ -implanted 4H-SiC for 1950 °C annealing.

time. The hole mobilities were again in the range of 3 – 7 cm<sup>2</sup>/Vs, which is an indicator of chemically activated electrical conduction.

Microwave annealing resulted in an increasing sheet carrier concentration with increasing annealing temperature (upto 2050 °C) and increasing anneal duration in spite of losing a portion of the implanted layer due to sublimation. If this sublimation rate is factored into the results, the increasing sheet carrier concentration with increasing annealing temperature is much more impressive than indicated by Figs. 20 and 21.

#### **2.2.2.8 Electrical characteristics of phosphorus implanted 4H-SiC**

A plot of sheet resistance ( $R_s$ ) and sheet electron concentration ( $n_s$ ) of the phosphorus implanted material, as a function of the microwave annealing temperature in the range 1700 °C – 1950 °C, for an anneal duration of 30 s, is shown in Fig. 22 . A corresponding plot of electron mobility is shown in Fig. 23.

It can be observed from Fig. 22 that microwave annealing at temperatures  $\geq 1900$  °C for 30 s yields ultra-low sheet resistances ( $< 50 \Omega/$ ) combined with high sheet electron concentrations. Microwave annealing at 1950 °C for 30 s resulted in an unprecedented low sheet resistance of 14  $\Omega/$  accompanied by a very high RT sheet electron concentration of  $4.41 \times 10^{15} \text{ cm}^{-2}$  and a very high electron mobility of 100 cm<sup>2</sup>/Vs. Such high sheet electron concentrations at RT are possibly due to the high doping concentrations ( $2 \times 10^{20} \text{ cm}^{-3}$ ) used in this study, which exceeded the  $N_c$  (conduction band density of states) value<sup>72</sup> for 4H-SiC ( $1.35 \times 10^{19} \text{ cm}^{-3}$ ), resulting in an impurity band formation under the conduction band, and subsequent reduction in the carrier ionization

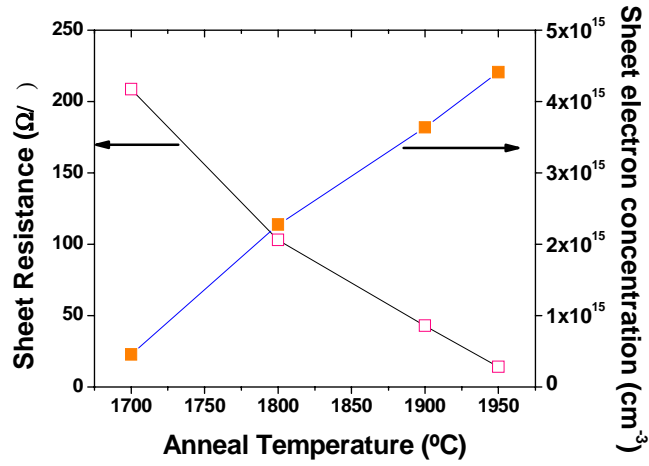


**Figure 22:** Plot of sheet resistance and implant sheet carrier concentration, as a function of annealing temperature in P<sup>+</sup>-implanted 4H-SiC, for 30 s anneals.

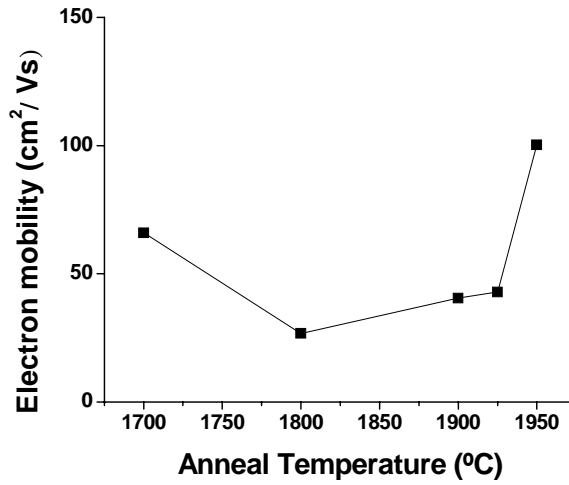


**Figure 23:** Plot of electron mobility as a function of microwave annealing temperature for 30 s anneals of P<sup>+</sup>-implanted samples.

energy. The combination of high carrier mobility and high sheet electron concentration is a clear indication of the alleviation of the implant-generated defects. To elucidate the dependence of electrical characteristics on the anneal time, a plot of  $R_s$  and  $n_s$ , as a function of annealing time in the range 15 – 60 s at a temperature of 1925 °C is shown in Fig. 24. There is a drop in the sheet resistance and a corresponding increase in sheet carrier concentration, with an increasing annealing time. For a similar phosphorus doping concentration, Senzaki et.al.<sup>44</sup> observed a decrease in  $n_s$  with increasing annealing time for 1700 °C annealing. They attributed this behavior to the precipitation of P donors, which leads to effective carrier density lowering. However, upon comparing Figs. 23 and 24, it can be concluded that as in case of Al-implantation, the electrical characteristics show a much weaker dependence on anneal time compared to the annealing temperature.

#### **2.2.2.9 Summary of uncapped microwave annealing in a pure nitrogen ambient**

Solid-state microwave annealing is an attractive method for rapid thermal annealing of implanted SiC. Using this technique, annealing temperatures as high as 2100 °C can be reached with a ramp-up rate of > 600 °C / s and a fall rate of 400 °C / s. RMS surface roughness after uncapped microwave annealing at 2050 °C for 30 s in N<sub>2</sub> ambient is comparable to the surface roughness of the capped samples subjected to the conventional annealing at 1700 °C. Annealing in N<sub>2</sub> ambient prevented the formation of a thick oxide layer, which was observed in open air annealing. SIMS depth profiles show negligible Al in-diffusion even at annealing temperatures as high as 2100 °C. However, the sublimation of about 100 nm of the SiC surface layer is noticed upon annealing at

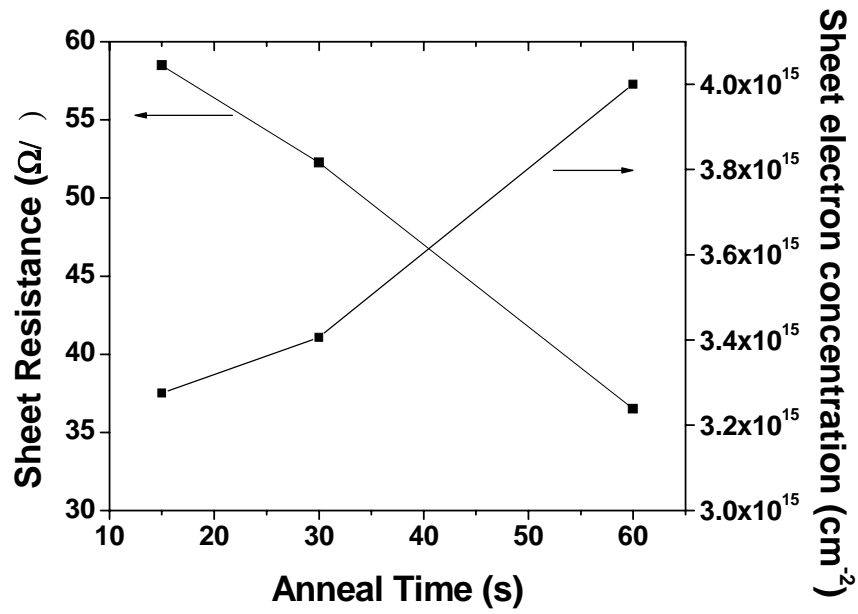


**Figure 24:** Plot of sheet resistance and sheet electron concentration, as a function of annealing time at 1925 °C in P<sup>+</sup>-implanted 4H-SiC.

2100 °C for 15 s. In the next phase of this work, anneals are performed on graphite capped SiC samples, in order to minimize surface sublimation. The lattice quality of the microwave annealed material is near the virgin SiC, indicating complete removal of implantation induced damage. Electrical characterization of both Al<sup>+</sup>- and P<sup>+</sup>- implanted material subjected to microwave annealing yielded very low sheet resistance and high carrier mobility values. This is again an indication that the microwave annealing is effective in both activating the implanted dopants and reducing the implantation generated defects in the SiC material. To avoid sublimation at high annealing temperatures in N<sub>2</sub> ambient, surface capping is required.

### **2.3 Microwave annealing with a protective graphite cap**

For uncapped microwave anneals performed in N<sub>2</sub> ambient, we achieved very low sheet resistances for both Al- and P-implanted 4H-SiC<sup>63</sup>. However, SIMS depth profiles indicated a sublimation loss of ~ 70 nm thick implanted SiC for the 1950 °C / 15 s annealing, which is unacceptable for reliable device processing.

In this phase of the work<sup>73</sup>, the Al-implanted 4H-SiC samples were capped by a layer of photoresist-converted graphite prior to the annealing, in an attempt to avoid the SiC surface sublimation during high-temperature microwave annealing. Recently, photoresist converted graphite layers have been effectively employed in conventional furnace annealing of implanted SiC to reduce the surface sublimation problem<sup>65,74-77</sup>. These graphite capping layers were reliable up to a temperature of ~ 1800 °C for conventional furnace annealing. Schottky diodes on 4H-SiC fabricated by graphite

capped annealing of implanted p-type layers have displayed lower reverse leakage currents and higher diode ideality factors<sup>65,77</sup>. Due to the ultra-fast heating/cooling rates achievable with the microwave RTA system, it is attractive to extend this upper temperature limit for the graphite capped Al-implanted SiC. In this section, the surface morphology, structural and electrical characteristics of the microwave annealed and conventional furnace annealed Al ion-implanted SiC layers that were protected by the graphite cap during annealing are compared.

### **2.3.1 Experimental details regarding implantation, annealing and graphite capping**

The multiple energy aluminum implantations were performed (at 500 °C) into lightly doped ( $5 \times 10^{16} \text{ cm}^{-3}$ ) n-type, 6  $\mu\text{m}$  thick epilayers grown on a heavily n-type doped, 4° off-axis (toward the [11-20] direction) 4H-SiC substrate. The multiple energy Al<sup>+</sup> implant schedule consisted of 45 keV /  $3.5 \times 10^{14} \text{ cm}^{-2}$ , 85 keV /  $2 \times 10^{14} \text{ cm}^{-2}$ , 140 keV /  $8 \times 10^{14} \text{ cm}^{-2}$ , and 210 keV /  $1 \times 10^{15} \text{ cm}^{-2}$  implants. The total Al implant dose was  $2.35 \times 10^{15} \text{ cm}^{-2}$ , resulting in an almost uniform Al concentration of  $1.3 \times 10^{20} \text{ cm}^{-3}$  to a depth of  $\sim 0.2 \mu\text{m}$ . In order to form the graphite capping layer, a layer of photoresist was first spin-coated on the Al-implanted SiC wafer and heat treated in a conventional furnace. The samples cut from this wafer were then subjected to microwave annealing at 1050 °C for 5 s in a N<sub>2</sub> atmosphere, which resulted in a graphitic surface. The graphite-capped implanted face of the sample was placed in close proximity with an in-situ doped conductive 4H-SiC sample during high-temperature ( $\geq 1750 \text{ °C}$ ) microwave annealing to achieve both optimum microwave coupling to the implanted sample and for extra surface

protection. After the high-temperature annealing, the graphite cap was removed by dry oxidation inside a conventional horizontal tube furnace at 1050 °C for 2 hrs. After removing the graphite cap, the samples were dipped in buffered hydrofluoric acid to remove any SiO<sub>2</sub> that may have formed on the SiC surface during the tail end of graphite cap removal. In this work, all microwave anneals were performed in a 100% N<sub>2</sub> atmosphere. Microwave annealing was performed in the temperature range of 1750 °C – 1900 °C, for durations of 15 s – 1 min. For comparison, samples cut from the same Al<sup>+</sup>-implanted wafer were subjected to conventional furnace annealing at a temperature of 1800 °C for 5 min using the graphite cap.

### **2.3.2 XPS characterization of the graphite cap**

The surface chemistry of the graphite cap and the microwave annealed, ion-implanted SiC (after the graphite layer removal) were studied by XPS. The purpose of the XPS measurements here is to confirm the reliable application and removal of the graphite cap. It was found that subjecting the photoresist layer capped SiC to a 1050 °C / 5 s microwave anneal resulted in a graphitic capping surface (characterized by a very high electrical conductivity), and a shifting of the binding energy (BE) of the C1s energy level. The XPS spectrum of the 1050 °C / 5 s microwave annealed graphite capping layer is shown in Fig. 25(a). Narrow XPS scans for the C1s energy level of the capped samples before and after the 1050 °C treatment are shown as an inset of Fig. 25. Upon performing the 1050 °C heat treatment, the BE for the C1s shifts from 284.6 eV to 283.7 eV indicating a transformation of the hydrocarbon layer to graphite. Similar XPS spectra (not

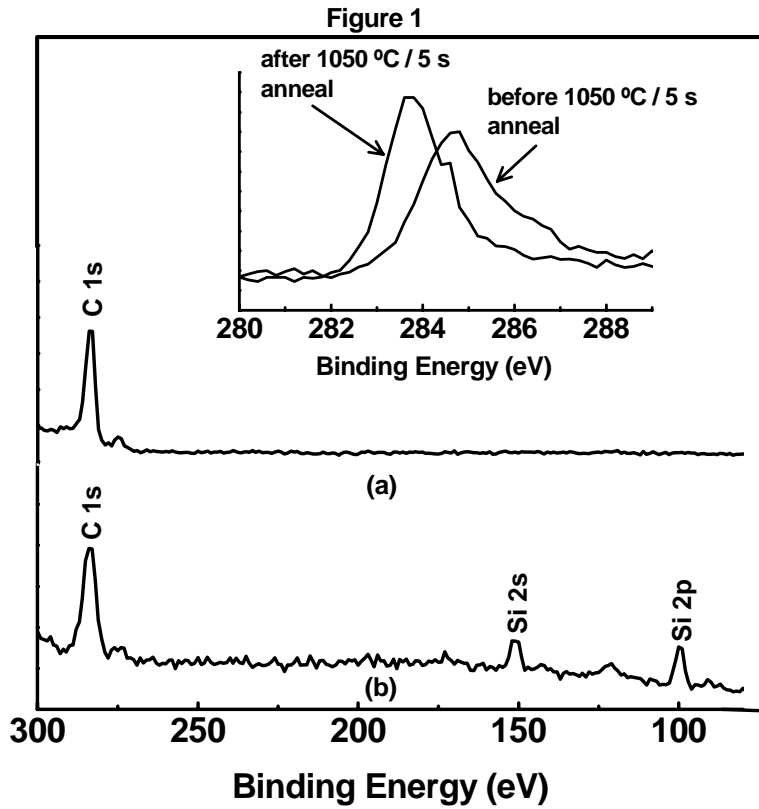
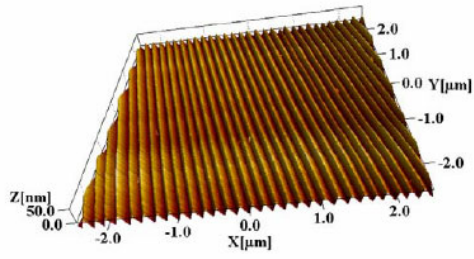


**Figure 25:** (a) XPS spectrum of the photoresist coated SiC surface microwave annealed at 1050 °C for 5 s. The binding energy of C1s at 283.7 eV is consistent with graphite. (b) XPS spectrum of the SiC surface after 1800 °C microwave annealing subsequent to removing the graphite cap by dry oxidation at 1050 °C for 2 hours. Inset shows narrow XPS scans of the C1s peak before and after the 1050 °C / 5 s microwave treatment showing the shifting of the C1s BE from 284.5eV (consistent with hydrocarbon) to 283.7 eV (consistent with graphite).

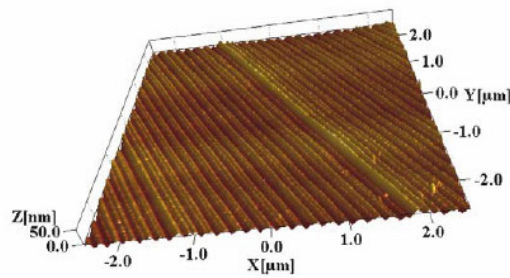
shown) were obtained on the graphite cap after 1900 °C / 30 s microwave annealing, indicating that the graphite capping layer remained on the SiC surface even after the microwave annealing at the highest temperature (1900 °C) used in this work. The XPS spectrum of the microwave annealed (1800 °C / 30 s), Al-implanted SiC surface after removal of the graphite cap is shown in Fig. 25(b). As mentioned earlier, a dry oxidation process at 1050 °C for 2 hours was used to remove the graphite cap. Three sharp peaks at 99.8 eV, 150 eV and 282.4 eV are seen in Fig. 25(b), which can be correlated to the BEs of Si 2p, Si 2s and C 1s in silicon carbide, respectively. Another faint peak can be seen at 122 eV in Fig. 25(b), which represents the BE of the Al 2s orbital. This Al signal could be coming from the implanted species. Therefore (based on the Si and Al peaks), it can be concluded that the graphite cap was reliably removed after microwave annealing using the 1050 °C/ 2 hr heat treatment in oxygen ambient. Thus, the reliable application, sustainability, and removal of the graphite cap were confirmed by the XPS measurements.

### **2.3.3 Surface morphology of the graphite capped microwave annealed material**

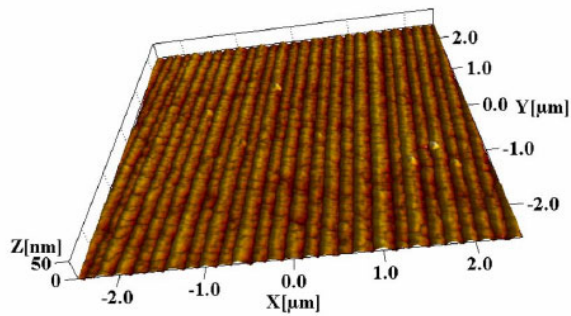
Figure 26 shows the AFM scans of the 4 ° off-axis, Al-implanted 4H-SiC surface before and after microwave annealing at 1900 °C for 30 s. An AFM scan of an 1800 °C/ 5 min. conventional furnace annealed sample is also shown in Fig. 26 for comparison. Both the microwave and conventional annealed samples were protected by the graphite cap during annealing. On the as-implanted sample surface, macrosteps with heights of 10 nm – 15 nm and terrace widths of 150 nm – 200 nm can be seen. Based on the model of Kukta et al.<sup>78</sup>, the short-range attractive step interactions facilitate the macrostep



(a) as-implanted 4 deg off-axis SiC



(b) 1800 °C / 5 min conventional anneal



(c) 1900 °C / 30 s microwave anneal

**Figure 26:** Tapping mode AFM scans of Al-implanted 4H-SiC for different conditions: (a) as-implanted (b) 1800 °C / 5 min. conventional annealing using graphite cap, and (c) 1900 °C / 30 s microwave annealing using graphite cap.

formation. It is speculated<sup>79</sup> that the enhanced macrostep formation on 4° off-axis substrates may be driven by the surface attempting to lower its surface free energy by forming large area facets with the (0001) and (11-20) orientations, as atomic planes of the form (11-2n) have been shown to have a local minimum in surface free energy<sup>80</sup>. It has been known for some time that epitaxial growth on low off-cut angle substrates yields fewer surface defects such as basal plane dislocations (BPD). A high density of BPDs is undesirable because of the so-called forward voltage instability problem in high-voltage SiC bipolar devices<sup>81</sup>. On the surface of both the conventionally annealed sample as well as the microwave annealed sample, the heights of the macrosteps are appreciably smaller, and the steps become more rounded compared to the as-implanted sample surface, possibly suggesting a relaxation to a lower surface energy configuration. Another explanation for the rounding of the steps could be the oxidation of the SiC surface during the dry oxidation process for graphite cap removal. The RMS surface roughness values for the as-implanted (1.8 nm), conventionally annealed (1.4 nm) and 1900 °C / 30 s microwave annealed (2.4 nm) samples are comparable. Thus, high-temperature microwave annealing at 1900 °C for 30 s still preserves the surface morphology of the SiC, if a graphite cap is used for protecting implanted SiC surface.

#### **2.3.4 SIMS depth profiles**

Secondary ion mass spectrometry (SIMS) depth profilometry was performed to study any diffusion of the implanted aluminum atoms, as well as any surface sublimation, which would result in a loss of the implanted layer. It is well-known that implanted dopants

such as aluminum<sup>82</sup> and phosphorus<sup>83</sup> (in the (0001) plane 4H- and 6H-SiC) do not exhibit any substantial diffusion when subjected to high-temperature annealing. As mentioned before, microwave annealing of phosphorus and aluminum ion-implants into the (0001)-face of 4H-SiC did not result in any noticeable dopant in-diffusion into the bulk even at temperatures as high as 2100 °C for 15 s – 30 s anneal durations. However, as mentioned before, a surface sublimation of ~ 70 nm was observed for the 1950 °C / 15 s microwave annealing<sup>63</sup>. SIMS Al depth profiles of an as-implanted sample and samples subjected to the 1900 °C / 30 s microwave annealing and the 1800 °C / 5 min. conventional annealing are shown in Fig. 27. Both the microwave and conventionally annealed samples were protected by graphite caps during the annealing. It can be seen that the tail region (~ 0.45 μm from the surface) of the Al as-implant profile almost coincides with the profiles of the annealed samples. This is an indication that the graphite cap was effective in eliminating SiC surface sublimation during both conventional and microwave annealing. However, after both annealing procedures, the Al profiles show a surface depletion of Al and a pileup of Al at a depth of 30 nm - 45 nm from the surface. Similar implant doses were extracted from the SIMS Al depth profiles of the microwave ( $2.04 \times 10^{15} \text{ cm}^{-2}$ ) and conventionally ( $2.0 \times 10^{15} \text{ cm}^{-2}$ ) annealed samples. Comparison with the Al as-implant dose ( $2.35 \times 10^{15} \text{ cm}^{-2}$ ), indicates a loss of 14% of the implanted Al during annealing. This can be attributed to the diffusion of Al into the graphite cap, driven by the steep concentration gradient of Al across the SiC/graphite cap interface. This value (14% Al implant loss) is still much lower than the 40% Al implant loss recently reported by Wang et al.<sup>84</sup> for a graphite capped, 1800 °C / 10 min conventional

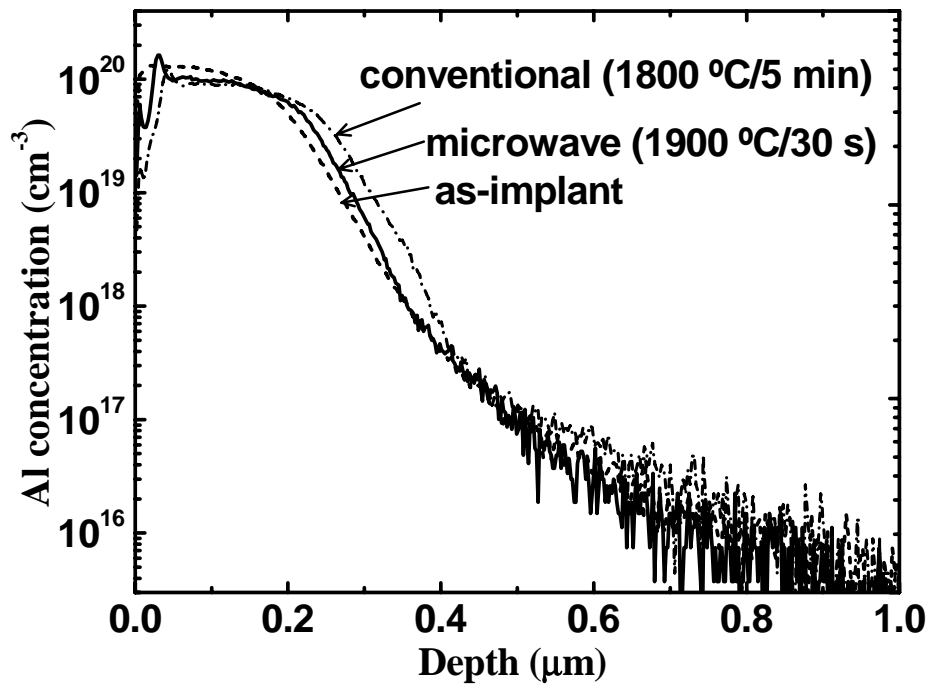


**Figure 27:** SIMS Al depth profiles for the as-implanted, 1800 °C / 5 min. conventionally annealed, and the 1900 °C / 30 s microwave annealed Al-implanted 4H-SiC.

furnace annealing. It can also be seen from Fig. 27 that compared to the furnace annealed sample, the Al profile in the microwave annealed sample exhibits a smaller extent of diffusion into the bulk SiC. These results indicate that a short duration (few seconds) annealing at a high temperature is effective in both preserving the implant dose, and in minimizing the dopant redistribution during annealing.

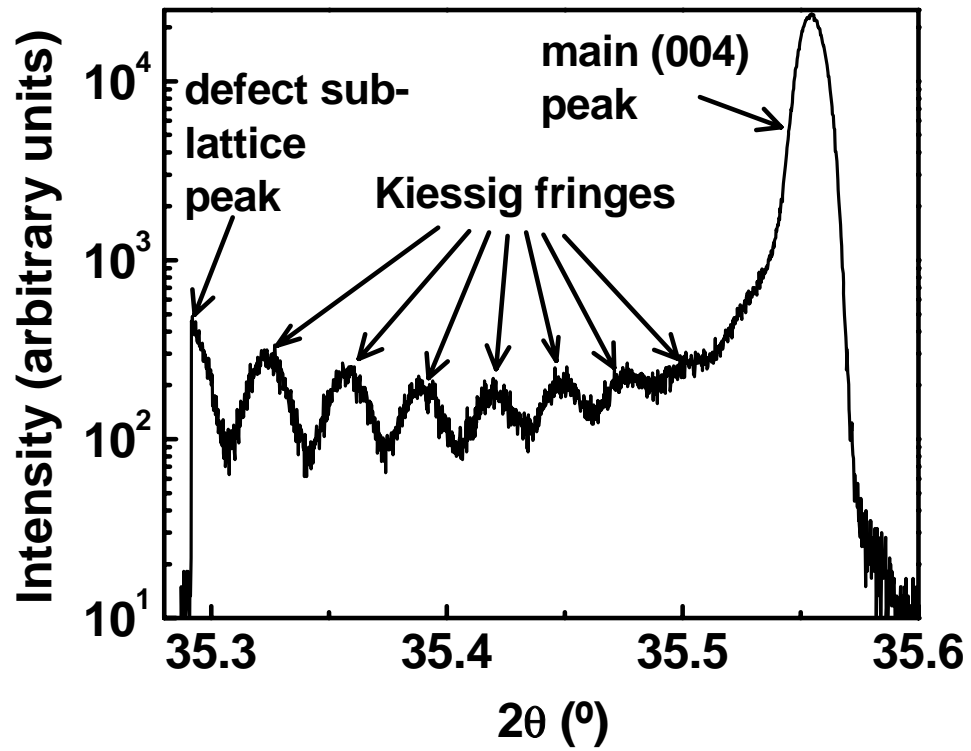
### 2.3.5 X-ray diffraction study

Figure 28 shows a narrow high-resolution XRD  $\theta$ - $2\theta$  scan around the (004) Bragg reflection of the Al as-implanted sample. In addition to the main SiC (004) peak, subsidiary peaks known as Kiessig fringes<sup>85</sup> and the sub-lattice peak due to implanted species can also be seen. The Kiessig fringes appear due to the interference of the x-rays reflected from the top and bottom faces of a lattice damaged layer<sup>86</sup>. The thickness, ‘t’ of the lattice damaged layer can be calculated from the following equation<sup>86</sup>

$$t = \frac{\lambda}{2(\sin \theta_n - \sin \theta_{n-1})} \quad (1)$$

where,  $\lambda$  is the wavelength of the x-rays,  $\theta_n$  and  $\theta_{n-1}$  are the Bragg angles of the nth and the (n-1)th Kiessig fringes. The calculated thickness (average ‘t’ value) of the Al implanted layer was found to be 0.3  $\mu\text{m}$ , which roughly agrees with the  $R_p + 2\Delta R_p$  of the highest energy (210 keV) ions used for the Al implantation.

Figure 29 shows the (0,0,12)  $\theta/2\theta$  diffraction profiles for the Al as-implanted 4H-SiC sample and a 1900 °C / 30 s microwave annealed sample. For the as-implanted sample, in addition to the SiC (0,0,12) peaks, sub-lattice peaks (magnified 6 times) can be observed on the low angle sides. These peaks indicate the presence of a



**Figure 28:**  $\theta$ - $2\theta$  x-ray diffraction profile for the SiC (004) reflection for the Al as-implanted 4H-SiC sample, showing subsidiary peaks known as Kiessig fringes between the defect sub-lattice peak and the main epilayer peak.

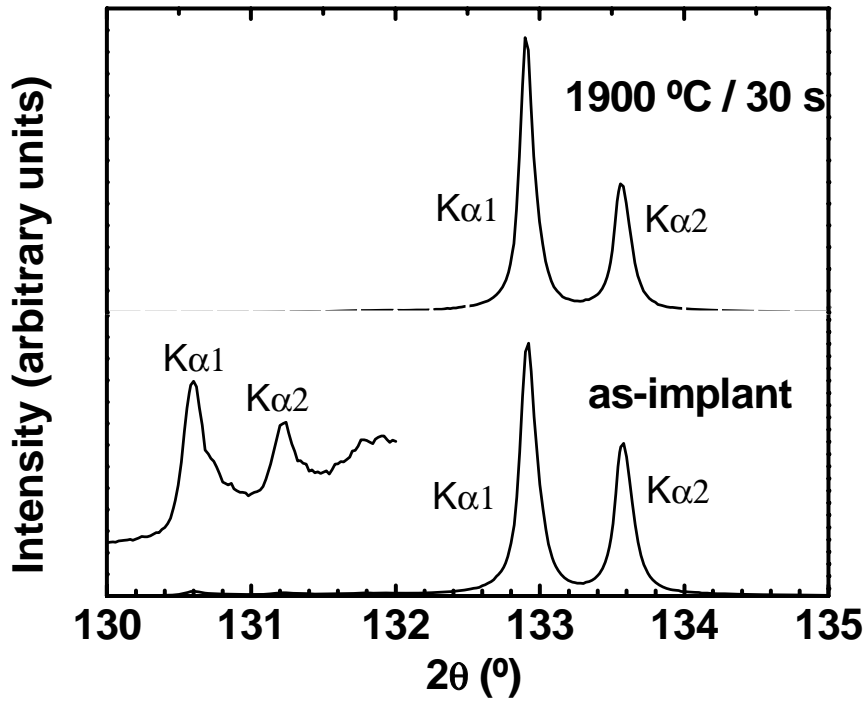


**Figure 29:**  $\theta$ - $2\theta$  x-ray diffraction spectra for the (0,0,12) reflection from the Al as-implanted and the 1900 °C / 30 s microwave annealed 4H-SiC samples. For the as-implanted samples, in addition to the  $K\alpha_1$  and  $K\alpha_2$  components of the main epilayer peak, defect sub-lattice peaks (magnified 6 times) are also observed at  $2\theta = 130.6^\circ$  ( $K\alpha_1$ ) and  $131.4^\circ$  ( $K\alpha_2$ ).

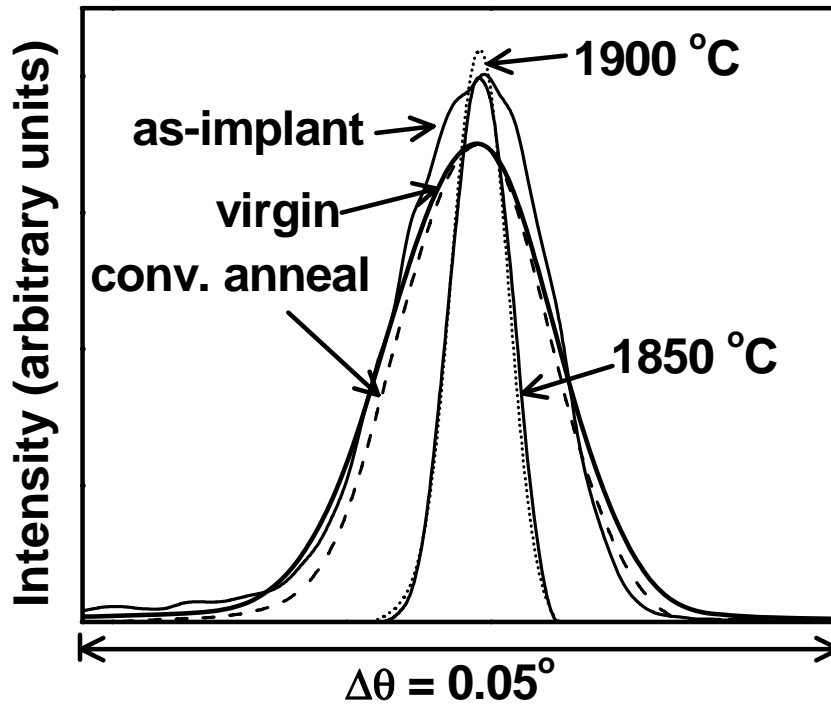


**Figure 30:** High resolution rocking curves of the SiC (004) from the Al as-implanted 4H-SiC sample, after conventional annealing at 1800 °C for 5 min., and after microwave annealing at 1850 °C and 1900 °C for 30 s. The FWHM of the 1850 °C microwave anneal is ~23% better than the conventional anneal indicating a substantial reduction in dislocation density for microwave annealing.

defect sub-lattice with a larger d-spacing as compared to the virgin sample, caused by the displaced Si and C and implanted Al occupying the interstitial lattice positions<sup>86</sup>. For the microwave annealed sample, the disappearance of the sub-lattice peaks indicates that the displaced Si and C have taken their equilibrium lattice positions and the implanted species are incorporated into substitutional positions in the lattice.

Figure 30 shows an overlay of the high-resolution rocking curves (HRRCs) for the SiC (004) reflection for the as-implanted, conventionally annealed (1800 °C / 5 min.) and microwave annealed (1850 °C / 30 s and 1900 °C / 30 s) samples. The HRRC of a virgin 4H-SiC sample (backside of the as-implant sample) is also shown for reference. The HRRC of the as-implanted sample has a full width at half maximum (FWHM) of 42 arc-sec. The HRRC of the conventionally annealed sample is slightly narrower with a FWHM value of 34 arc-sec. However, both the 1850 °C and 1900 °C microwave annealed samples exhibit very narrow HRRCs with FWHM values of 17 arc-sec and 15 arc-sec respectively. The rocking curve for the 1900 °C / 30 s microwave annealed sample is narrower than the rocking curve for the conventionally annealed sample by more than a factor of 2. The FWHM for the virgin sample is 22 arc-sec, which is comparable to that of the as-implant sample.

For the (ion-implanted, single crystal) samples under consideration in this work, the broadening of the rocking curves may be due to contributions from lattice mosaicity, tilt, strain, and random array of dislocations. Thus the reduction in FWHM's of the rocking curves implies reduction in both strain and dislocation density. A remarkable

outcome of these measurements suggests that we can improve the crystalline quality of the SiC significantly through microwave annealing.

One important parameter to consider while analyzing the rocking curve results is the “sampling depth” for the x-ray diffraction. The penetration depth, ‘s’, of x-rays in SiC, which can be roughly assumed to be the sampling depth, is given by [87]:

$$s = \frac{\sin(\theta_i)}{\mu_{SiC}} \quad (2)$$

where  $\mu_{SiC}$  is the linear mass attenuation co-efficient in SiC which is equal to 150.3159 [Ref<sup>87</sup>], and  $\theta_i$  is the angle of incidence of the x-rays normal to the surface. Thus for the (004) Bragg reflection for which the HRRCs were collected, the ordinary penetration depth of the x-rays is about 20.33  $\mu\text{m}$ , but in the dynamical diffraction condition the penetration is only up to 3  $\mu\text{m}$ . The conclusions drawn out from analysis of the rocking curves apply to the top 3  $\mu\text{m}$  of the SiC, of which the implanted layer is only 0.3  $\mu\text{m}$  thick. However, the RCs of the microwave annealed samples are much narrower than the virgin sample. Therefore, it can be inferred that in addition to removing the implant related damage in the shallow surface region of the wafer, the microwave annealing was successful in alleviating the defects introduced into the SiC epilayer as well as the underlying substrate during their growth.

### **2.3.6 Rutherford backscattering – channeling (RBS-C) study**

The RBS-C spectra recorded from the Al<sup>+</sup> -implanted SiC samples, before and after graphite-capped 1900 °C / 30 s microwave and 1800 °C / 5 min conventional annealings are shown in Fig. 31. The scattering yields from a randomly aligned sample

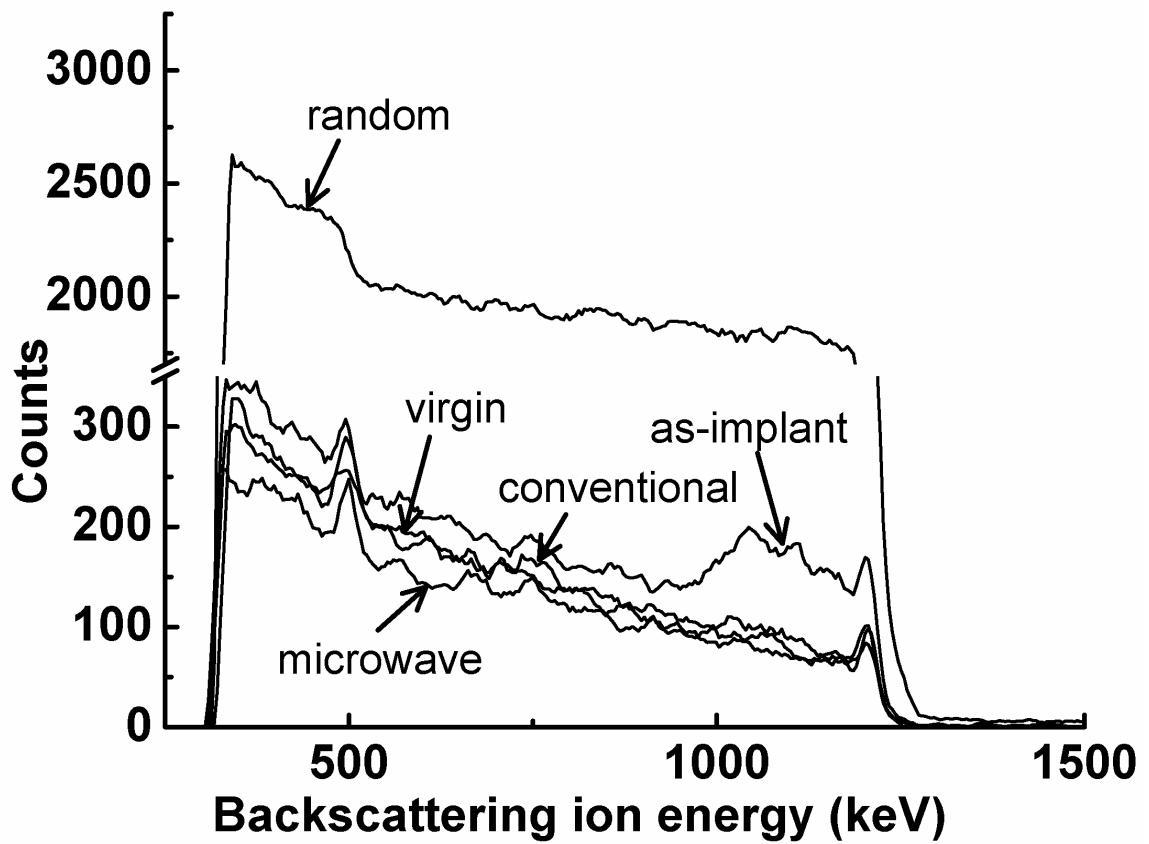


**Figure 31:** RBS-C spectra on Al as-implanted, 1800 °C / 5 min conventionally annealed and 1900 °C / 30 s microwave annealed 4H-SiC. A RBS-C spectrum from un-implanted SiC and a randomly aligned SiC is also shown for comparison.

(which corresponds to fully amorphized SiC) and a virgin (un-implanted SiC) sample are also shown in Fig. 31 for reference. As expected, the as-implanted sample shows a higher scattering yield compared to the annealed samples, but farther away from the random level, indicating that the material is not amorphized. The Al-implant has not amorphized the SiC due to elevated implantation temperature (500 °C) used in this study. Both the conventional as well as the microwave-annealed samples exhibit scattering yields close to the virgin level. Compared with the conventionally annealed sample, the microwave-annealed sample shows slightly lower scattering yields especially in the vicinity of the C sub-lattice signal. Considering this result in combination with the x-ray rocking curve measurements (which sampled 3  $\mu\text{m}$  of the sample surface), it can be said that the microwave annealing removes the defects introduced during the growth of the SiC epilayer in addition to removing the implantation-generated defects.

### **2.3.7 Electrical characterization**

The sheet resistance ( $R_s$ ) of an implanted SiC layer is a reasonable parameter to evaluate its electrical characteristics because a low  $R_s$  can be obtained only if both the sheet carrier concentration and carrier mobility are high. Hence, in this work,  $R_s$  is used as the prime figure of merit of electrical characteristics of the implanted/annealed 4H-SiC. Plots of sheet resistance and hole mobility, as a function of the microwave annealing temperature in the range 1750 °C – 1900 °C, for an anneal duration of 30 s, are shown in Fig. 32. The Hall concentration and mobility are determined using the following equations<sup>88</sup> from

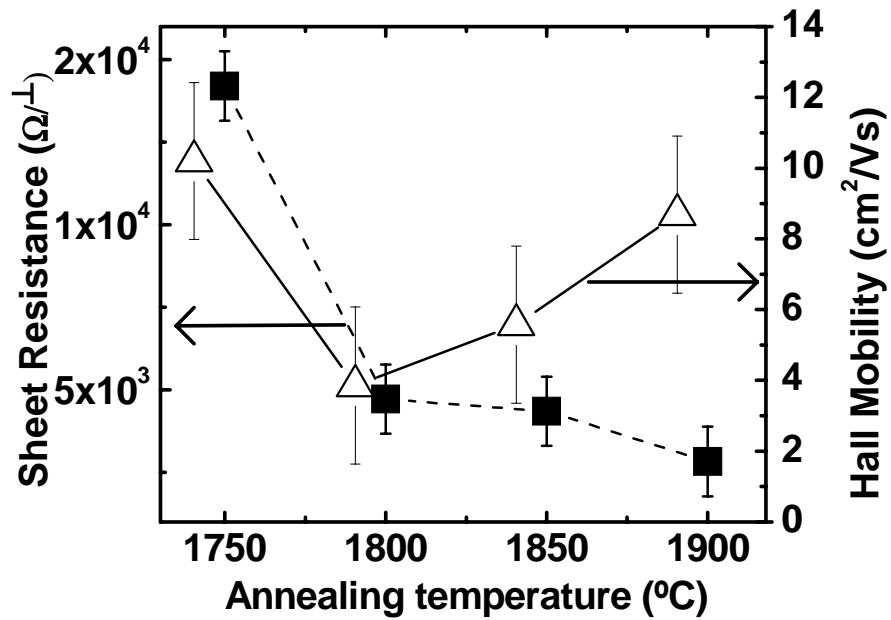


**Figure 32:** Measured sheet resistance and hole mobility as a function of annealing temperature for the 30 s microwave annealing. Error bars for the sheet resistance and hole mobility are estimated as 90% confidence limits for replicate measurements made on five samples, conventionally annealed at 1800 °C for 5 min.

the measured Hall coefficient,  $R_H$ .

$$p = \frac{r_H}{eR_H} \quad (3)$$

for the Hall concentration, and

$$\mu_H = \frac{R_H}{\rho_S r_H} \quad (4)$$

for the Hall mobility. In equations (3) and (4),  $\rho_S$  and  $r_H$  are the sheet resistance and the Hall scattering factor, respectively. The Hall scattering factor,  $r_H$ , depends on the scattering mechanisms, the anisotropy of the scattering mechanisms, and the anisotropy of the valence band energy surface<sup>89</sup>. The  $r_H$  is usually determined by using the relaxation time approximation (Mathiessen rule). However, it has been shown that the relaxation-time approximation is not the best choice to calculate the Hall scattering factor for p-type material. Therefore, most people simply approximate  $r_H$  as unity for SiC. However, recent works have shown that this approximation overestimates the Hall scattering factor, which in turn, results in a systematic overestimation of the doping level determined by Hall measurements, sometimes resulting in more activated carriers than implanted species<sup>90</sup>. In this work, we used the temperature dependence of the Hall scattering factor,  $r_H$ , obtained for 4H-SiC by Pensl et al.<sup>91</sup> and fitted by Pernot et al.<sup>88</sup> by the empirical expression,

$$r_H = 1.74823 - 6.22 \times 10^{-3} T + 1.36729 \times 10^{-5} T^2 - 1.44837 \times 10^{-8} T^3 + 5.86498 \times 10^{-12} T^4 \quad (5)$$

where T is the temperature in K at which the Hall measurements are performed. For the

room temperature (298 K), at which the Hall measurements of this work were performed,  $r_H$  from eqn. (5) is calculated as 0.773.

It can be seen from Fig. 32 that increasing the microwave annealing temperature steadily lowers the sheet resistance, while increasing the hole mobility after an initial dip. It is known that hole mobility in ion-implanted 4H-SiC, at doping levels  $> 1 \times 10^{17} \text{ cm}^{-3}$  is primarily controlled by scattering at ionized impurities and scattering at implantation-induced defects<sup>90</sup>. The initial decrease in hole mobility (Fig. 32) can be attributed to increased ionized Al impurity scattering. The later increase in hole mobility with increasing temperature could be due to more effective defect removal by the microwave annealing. The sheet resistance (2.8 k $\Omega$ / ) for the 1900 °C / 30 s microwave annealed sample is a factor of 4.6 times lower compared to the value of 13 k $\Omega$ / measured for the 1800 °C / 5 min conventionally annealed sample, whereas the sheet carrier concentration (not shown) for the microwave annealed sample almost one order of magnitude higher ( $3.2 \times 10^{14} \text{ cm}^{-2}$ ) compared to the conventionally annealed sample ( $3.5 \times 10^{13} \text{ cm}^{-2}$ ). However, the hole mobility for the microwave annealed sample (8.7 cm<sup>2</sup>/ Vs) is only slightly lower than that for the conventionally annealed sample (13.7 cm<sup>2</sup>/Vs), even though the holes in the microwave annealed material are subjected to an enhanced ionized impurity scattering than the conventionally annealed sample. This means that the decreased sheet resistance measured for the microwave annealed samples is due to a combination of a much more effective Al implant activation, as well as effective implant-induced damage annealing, compared to the conventional furnace annealing.

### **2.3.8 Conclusions from graphite capped annealing**

The microwave RTA is very effective in annealing graphite cap protected, ion-implanted SiC. The surface morphology of the samples, microwave annealed at 1900 °C for 30 s (with a graphite cap) is very smooth with a RMS roughness as low as 2.4 nm. SIMS depth profiles show that the graphite cap is effective in preventing SiC surface sublimation even after a 1900 °C / 30 s microwave treatment. Also, the SIMS profile of the 1900 °C / 30 s microwave annealed sample shows a smaller degree of Al indiffusion compared to the 1800 °C / 5 min furnace annealed sample. However, some aluminum diffusion into the graphite cap during annealing results in a relatively small (14%) loss of the implanted dose, for both microwave and furnace annealed samples. High-resolution XRD rocking curves and RBS spectra indicate that the 30 s duration microwave annealing at temperatures  $\geq 1850$  °C is much more effective than the 1800 °C / 5 min conventional furnace annealing in not only annealing the implantation-induced lattice damage but also in removing the defects. Van der Pauw – Hall measurements indicate an extremely low sheet resistance value of 2.8 k $\Omega$ /□ accompanied by a relatively high mobility of 8.7 cm<sup>2</sup>/Vs for the 1900 °C / 30 s microwave annealing.

### **2.4 Summary and suggested future work on microwave annealing of ion-implanted SiC**

Ultra-fast microwave annealing at temperatures in the range of 1800 – 2000 °C is attractive for effectively annealing ion-implanted SiC. Microwave anneals after graphite capping the ion-implanted SiC layer effectively eliminated the surface sublimation

problem for microwave annealing temperatures up to 2100 °C. Smooth surfaces (RMS roughness  $\approx 1 - 2$  nm) and very low sheet resistances in the range of  $2 - 3$  k $\Omega/\square$  and  $14 - 50$   $\Omega/\square$  are obtained for Al- and P-implanted material, respectively, after short 30 s microwave annealing treatments at high temperatures. RBS-C and high-resolution XRD rocking curve scans indicate that microwave annealing is more effective than conventional annealing in healing implantation-induced as well as crystal growth-induced defects in SiC.

The drastic improvements in material quality when microwave annealing is used in place of conventional furnace annealing needs to be translated to improvements in device quality. In order to validate the microwave annealing technology at the device level, the impact of microwave annealing on the performance of MOS capacitors, p-i-n diodes with ion-implanted anode layers, and SiC power MOSFETs needs to be investigated. The low sheet resistances obtainable by microwave annealing may lead to a drastic decrease in overall power consumption and may lead to higher blocking voltages in SiC power devices. Also, the low defect levels obtainable by microwave annealing may lead to an improvement in the inversion layer mobilities for SiC MOSFETs and an increase in ambipolar carrier lifetime for p-i-n diodes.

### 3. MICROWAVE ANNEALING OF IN-SITU AND ION-IMPLANTED ACCEPTOR DOPED GALLIUM NITRIDE

#### 3.1 Existing issues concerning acceptor activation in in-situ and ion-implantation doped GaN

Gallium nitride (GaN) is a very important (direct) wide bandgap semiconductor for fabricating opto-electronic devices in the short-wavelength region and for high-power / frequency devices. Like SiC, the inability to achieve high p-type conduction in GaN has so far limited the commercialization of this otherwise promising semiconductor for many electronic and opto-electronic applications. Similar to the strong Si-C covalent bond in SiC, the large ionicity of the Ga-N bond gives GaN its unique properties, but also makes it a difficult material to work with technologically. Table VIII lists the best sheet resistance values and other electrical properties reported to-date for p-type GaN. The minimum achievable sheet resistance for doping with magnesium (Mg) and beryllium (Be), the popularly used p-type dopants in GaN, is in the range  $10^4 \Omega/\square$  -  $10^5 \Omega/\square$ . Clearly, these values are too high to permit one to fabricate high-performance electronic and opto-electronic devices. The difficulty in achieving low sheet resistance for p-type GaN may be attributed to the presence of high densities of donor-type point defects such as nitrogen vacancies ( $V_N$ ), and their complexes with native defects and acceptor dopants, which have relatively low formation energies. These defects are known to have a donor

**Table VIII:** List of the electrical characteristics of p-type GaN available from literature*PLA: pulsed laser annealing. RTA: rapid thermal annealing*

<b>Specie and doping method</b>	<b>Dose cm<sup>-2</sup></b>	<b>Depth μm</b>	<b>RTA temp/ time</b>	<b>Sheet Res. Ω/□</b>	<b>Mobility cm<sup>2</sup>/Vs</b>	<b>Sheet Carrier Conc. cm<sup>-2</sup></b>	<b>Ref</b>
Be implant	1 x 10 <sup>13</sup>	0.25	1100°C /30s	8.4 x 10 <sup>4</sup>	4.4	5.75 x 10 <sup>13</sup>	92
Be implant	5 x 10 <sup>14</sup>	40 KeV	PLA + RTA 1100 °C /120s	8.4 x 10 <sup>4</sup>	8.7	8.56 x 10 <sup>12</sup>	93
Be/N=1 Co-implant	2.5x 0 <sup>14</sup>	0.5	1200 °C /10s	5.6 x 10 <sup>4</sup>	6.8	2.7 x 10 <sup>12</sup>	94
Mg/N=2 Co-implant	1.5x 0 <sup>15</sup>	0.3	1200°C /10s	5.6 x10 <sup>3</sup>	7.7	1.4 x 10 <sup>14</sup>	94

behavior in GaN, thus restricting the maximum p-type conduction<sup>92-94</sup>. The achievement of high p-type conductivity is even more difficult in ion-implanted GaN layers<sup>3,9</sup> because the implantation-induced damage creates extra donor-type defects, which compensate the activated holes. Also, the optical properties of GaN are greatly diminished by ion-implantation resulting in a complete loss of luminescence even for low doses. The strongest effect is the creation of non-radiative recombination centers due to the implant-induced damage. The introduced defects have mainly deep levels within the bandgap; therefore the as-implanted GaN is electrically highly resistive. The damage must be annealed out to achieve optical and electrical activation of the implanted dopants. Fig. 33 summarizes schematically the fundamental diffusion, recovery, and activation processes that occur in ion-implanted GaN as a function of annealing temperature. It can be seen from Fig. 33 that the optical activation can be achieved in the temperature range 1200 °C – 1300 °C, but defect complexes (which cause an intense yellow band in the photoluminescence (PL) spectra) require still higher temperatures (in excess of 1300 °C) to break up. Acceptor-type activation in GaN is much more difficult to achieve compared to donor-type activation due to presence of unintentional compensating deep donors (for e.g. nitrogen vacancies,  $V_N$  and its complexes) as well as the absence of shallow acceptors. Halogen-lamp based rapid thermal annealing (RTA) is the common method used to anneal the defects, to repair the lattice damage and to activate the dopants in GaN. The lowest sheet resistance values,  $5.6 \times 10^4 \Omega/\square$  for Be-implanted GaN, and  $5.6 \times 10^3 \Omega/\square$  for Mg implanted GaN in Table VIII, were achieved using RTA at an annealing temperature of 1200 °C and a short anneal duration of 10 s. Fig. 34 shows an AFM

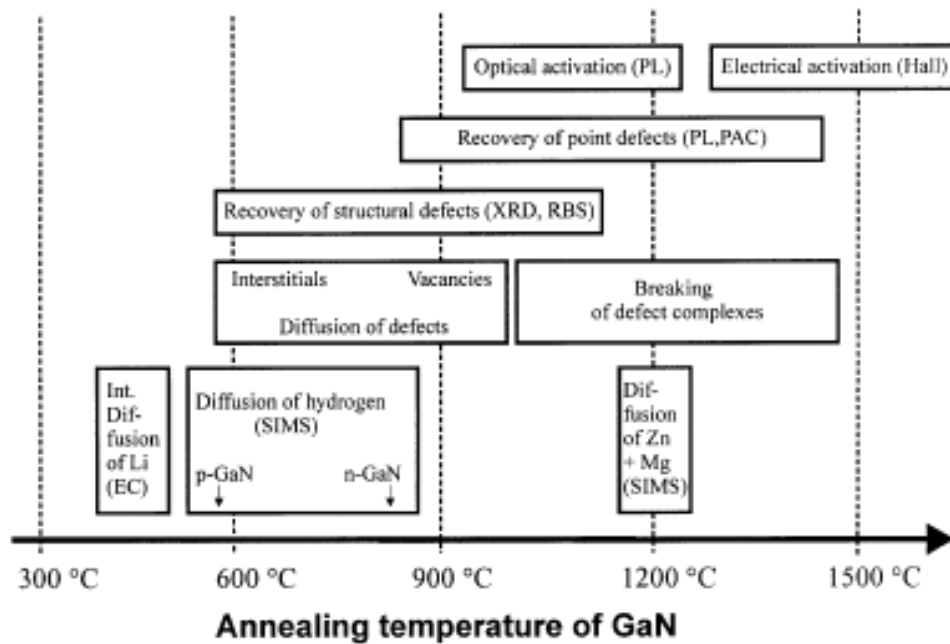


**Figure 33:** Diffusion, recovery, and activation processes of ion-implanted impurities in GaN as a function of annealing temperature.[C. Ronning et al. Phys. Reports **351**, 349 (2001)]

micrograph of a Be<sup>+</sup>-implanted GaN sample annealed by halogen-lamp RTA for 2 min. The RMS roughness extracted from the AFM image is 2 nm, inspite of only scanning a 1 μm x 1 μm square area.

High-resolution x-ray diffraction spectra for as-grown GaN, Be-implanted GaN, before and after both PLA and RTA are shown in Fig. 35. Compared to the MBE as-grown sample, the Be as-implanted sample shows both a broadening of the main (0002) GaN peak as well as the appearance of an additional peak at the low-angle side, which is consistent with the expansion of the GaN lattice in the implanted region. Even after the PLA treatment, the lower angle peak remains. This indicates that the shallow penetration depth of the 248 nm laser only anneals the near surface region and leaves the deeper crystal defects untouched. After RTA at 1100 °C following the PLA, the lower angle peak has disappeared, however, the main peak is still much broader compared to the as-grown sample, indicating that the RTA temperature is not high enough to anneal out all the implant-induced defects, and some residual strain still exists in the GaN layer after annealing. This result emphasizes the need for a RTA technique with a higher temperature capability.

Therefore the key requirements for optimum annealing conditions for GaN appear to include both a high annealing temperature and a short annealing time. As a rule of thumb, an implanted semiconductor should be annealed up to a temperature of 2/3 of its melting point for damage recovery and dopant activation<sup>92,95-98</sup>. In the case of GaN, this temperature is about 1650 °C. However, such high temperatures are well beyond the capability of most commercial halogen lamp-based RTA equipment, which only have a

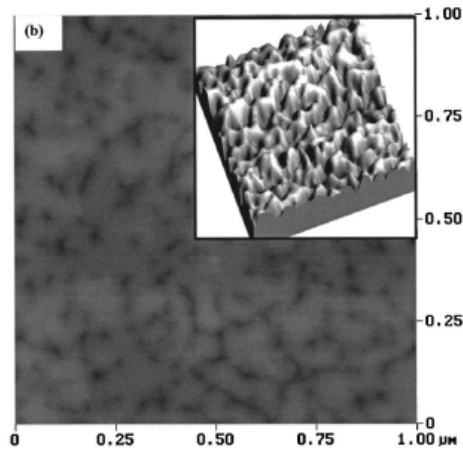


**Figure 34:** AFM micrograph of  $\text{Be}^+$ -implanted GaN, annealed by halogen lamp RTA at 1100 °C for 2 min.[H.T. Wang et al. J. Appl. Phys. **98**, 094901 (2005).]

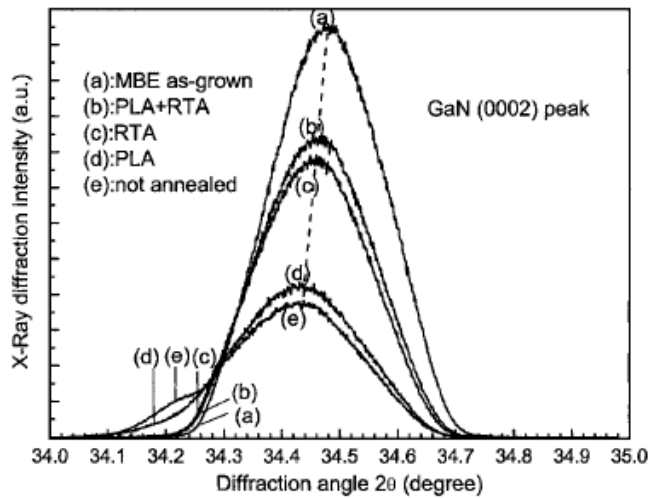


**Figure 35:** X-ray diffraction spectra  $\theta$ - $2\theta$  recorded for (a) a MBE as-grown GaN sample, (b) a Be-implanted sample after combination of PLA and RTA (c) a Be-implanted sample after RTA, (d) a Be-implanted sample after PLA, and (e) a Be-implanted sample without annealing [H.T. Wang et al. J. App. Phys. **98**, 094901 (2005)].

modest temperature capability of  $<1200$  °C. Therefore an annealing method with the capability of high processing temperature ( $\geq 1300$  °C) is needed<sup>92,97</sup>. Compared to SiC, an additional difficulty arises in case of GaN, which can not withstand slow heating rates and long duration anneals at temperatures  $\geq 1000$  °C due to an incongruent sublimation of GaN which decomposes into a N-rich gas and a gallium rich liquid at higher temperatures. Hence, to preserve the chemical integrity of GaN, and at the same time reduce the density of compensating defects, the required anneal temperature should be reached very fast and the annealing duration should be limited to a few seconds. Compared to SiC, the anneal duration for GaN has to be shorter to preserve surface integrity. This requirement on ultra-fast heating rates is not met by most conventional equipment.

Recently, a RTP unit called Zapper<sup>TM</sup> based on a MOCVD system has been built<sup>99</sup> that employs RF heating with heating rates of 50 °C/s. They have annealed ion-implanted GaN, capped with a layer of aluminum nitride (AlN) in the temperature range 1200 – 1500 °C. It is reported<sup>99</sup> by the authors that indeed temperatures as high as 1400 °C are required for alleviating the implantation induced lattice damage and optimally activating the implanted dopants. Figure 36 shows the sheet carrier concentration and mobility of Si-implanted GaN subjected to annealing using the Zapper furnace. It can be observed from Fig. 36 that there is an improvement in the AlN encapsulated material quality up to 1400 °C, but the results degrade for annealing temperatures  $> 1400$  °C. This is due to reliability issues associated with the AlN cap at higher temperatures, and possibly because the heating rates (50 °C/s) are still not high enough to prevent GaN

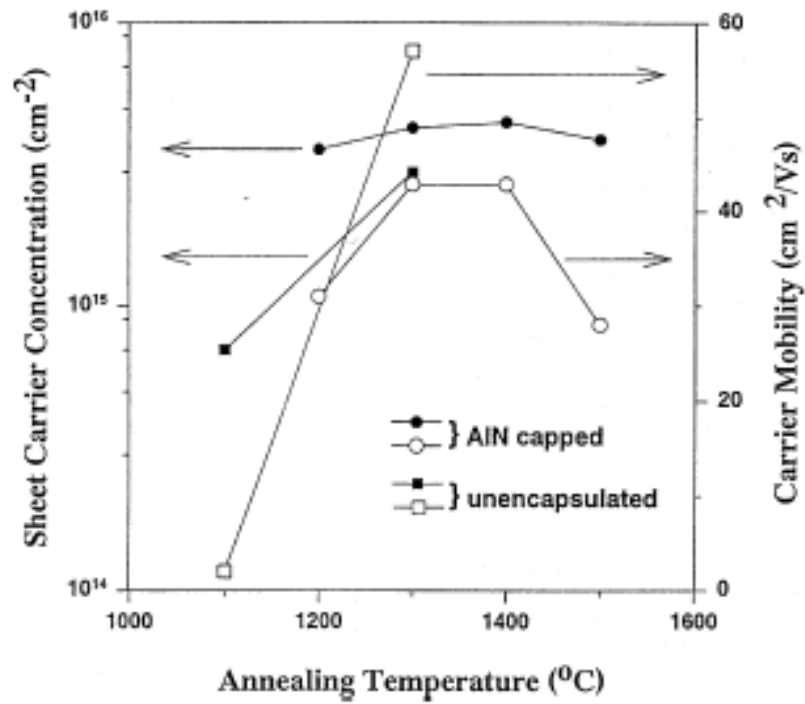


**Figure 36:** Electrical characteristics of uncapped and AlN capped GaN, annealed using the Zapper furnace with heating rates of 50 °C / s [Ref: S.J. Pearton, C.R. Abernathy, F. Ren, *Gallium Nitride Processing for Electronics, Sensors, and Spintronics*, Springer-Verlag, London (2006)].

decomposition. However, with the much higher heating rates achievable with the microwave annealing system used in this work, there is the possibility of reliably annealing GaN at temperatures higher than 1400 °C.

### **3.2 Microwave annealing of in-situ Mg doped GaN**

#### **3.2.1 Experimental Details**

The samples explored in this study were 3 μm thick Mg-doped GaN epilayers on a-plane sapphire substrates grown by metalorganic chemical vapor deposition (MOCVD)<sup>100</sup>. For heating the GaN sample, a 5 mm x 5 mm highly conducting 4H-SiC piece is placed directly underneath the GaN sample of interest to serve as the susceptor, when both the GaN sample and the SiC piece are placed within the microwave heating head. Microwave annealing of GaN is performed with and without a surface capping layer composed of MgO, AlN or graphite. The AlN layers (200 nm thick) were deposited on the GaN sample using pulsed-laser deposition<sup>101</sup>. The MgO layers (200 nm thick) were deposited on the GaN using electron beam evaporation of a MgO target. Fused lumps of MgO (Alfa Aesar, 99.95%, metals basics, 3-12 mm pieces) were used as target material. Graphite caps are formed on the GaN epilayers by first spin-coating a layer of standard photoresist, followed by annealing in vacuum at 750 °C. Microwave annealing is performed in the temperature range of 1300 – 1550 °C for short 5 s durations in a pure (99.999%) nitrogen atmosphere. After microwave annealing, the MgO cap is removed by etching in dilute acetic acid, whereas the AlN cap is removed by a 10 min etch in 85 wt% H<sub>3</sub>PO<sub>4</sub> at 80 °C.

The reliable application and removal of the AlN cap on the GaN surface was studied using x-ray photoelectron spectroscopy (XPS). The XPS spectra were acquired using a Mg K $\alpha$  x-ray source. The sample surface after annealing and removal of the cap is monitored by tapping mode atomic force microscopy (AFM). The optical characterization of the material is performed using low-temperature (5 K) photoluminescence (PL) spectroscopy. For obtaining the PL spectra, a He-Cd laser was used with an excitation intensity of 2.5 mW. For more details about the PL system, refer to Ref. 102. Room-temperature Hall measurements were performed after depositing (30 nm) Ni / (30 nm) Au contacts on the GaN layers in the van der Pauw geometry. The contacts were made ohmic by alloying in a conventional box furnace at 550 °C, in air, for 10 min.

### **3.2.2 XPS characterization of AlN capped GaN**

The reliability of the application, sustainability of the AlN cap during annealing, and removal of the AlN cap after microwave annealing was studied by XPS. A survey XPS scan of the surface of the AlN as-capped sample is shown in Fig. 37(a). Other than O 1s and C 1s signals coming from the native oxide/hydrocarbon layer, only Al and N signals can be seen in the survey scan. The survey XPS scan of the AlN capped sample after 1400 °C / 5 s microwave annealing is shown in Fig. 37(b). Surprisingly, no nitrogen signal can be detected from this scan but a rather strong O 1s signal is seen in addition to the Al signal. Narrow scans (not shown) of the O 1s peak were consistent with the

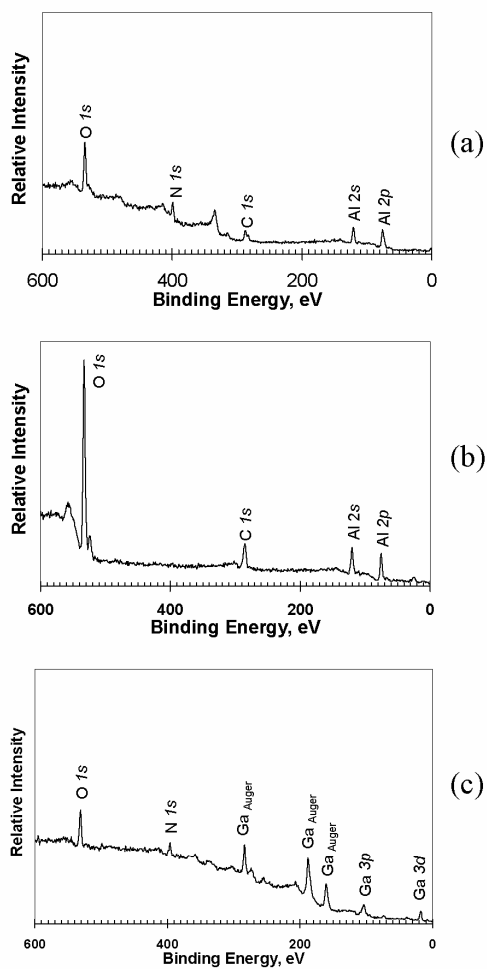


**Figure 37:** XPS survey scans of: (a) AlN as-capped GaN sample, (b) AlN capped sample after 1400 °C/5 s annealing, and (c) after removal of the AlN cap at the conclusion of annealing

presence of either  $\text{Al}_2\text{O}_3$  or  $\text{Al}(\text{OH})_3$  [Ref. 103].

Thus upon microwave annealing, the AlN film has oxidized and formed  $\text{Al}_2\text{O}_3$  and/or  $\text{Al}(\text{OH})_3$ . This is in spite of the fact that the annealing was done in a 99.999% atmosphere of UHP nitrogen, which emphasizes the strong oxidation affinity of the AlN film. A similar result was obtained after microwave annealing at  $1500\text{ }^\circ\text{C} / 5\text{ s}$ . A survey XPS scan of the sample after  $1400\text{ }^\circ\text{C}$  microwave annealing and removal of the cap by  $\text{H}_3\text{PO}_4$  is shown in Fig. 37(c). Clearly, Ga and N signals can be observed for this XPS scan, but no Al signals are observed indicating that the AlN cap was successfully removed. Again, a similar XPS scan was obtained for the  $1500\text{ }^\circ\text{C}$  annealed sample as well as after the AlN cap removal.

### **3.2.3. Surface morphology of the microwave annealed samples**

AFM images of the GaN sample surface, after microwave annealing at different temperatures with a MgO cap in place are shown in Fig. 38. It can be seen from Fig. 38 that the MgO cap was able to protect the GaN surface without any substantial decomposition at annealing temperatures up to  $1300\text{ }^\circ\text{C}$ , but significant GaN decomposition could be detected for the MgO capped annealing done at  $1400\text{ }^\circ\text{C}$  (Fig. 38(e)). The GaN film totally decomposed, when the microwave annealing temperature was increased above  $1400\text{ }^\circ\text{C}$ . Decomposition of the GaN was accompanied by cracking of the MgO cap, and liquid Ga droplets could be observed (not shown) on the surface.

AFM images of the GaN sample surface after microwave annealing at  $1300\text{ }^\circ\text{C}$  and  $1500\text{ }^\circ\text{C}$  with an AlN cap in place are shown in Fig. 38(d) and 38(f), respectively. It

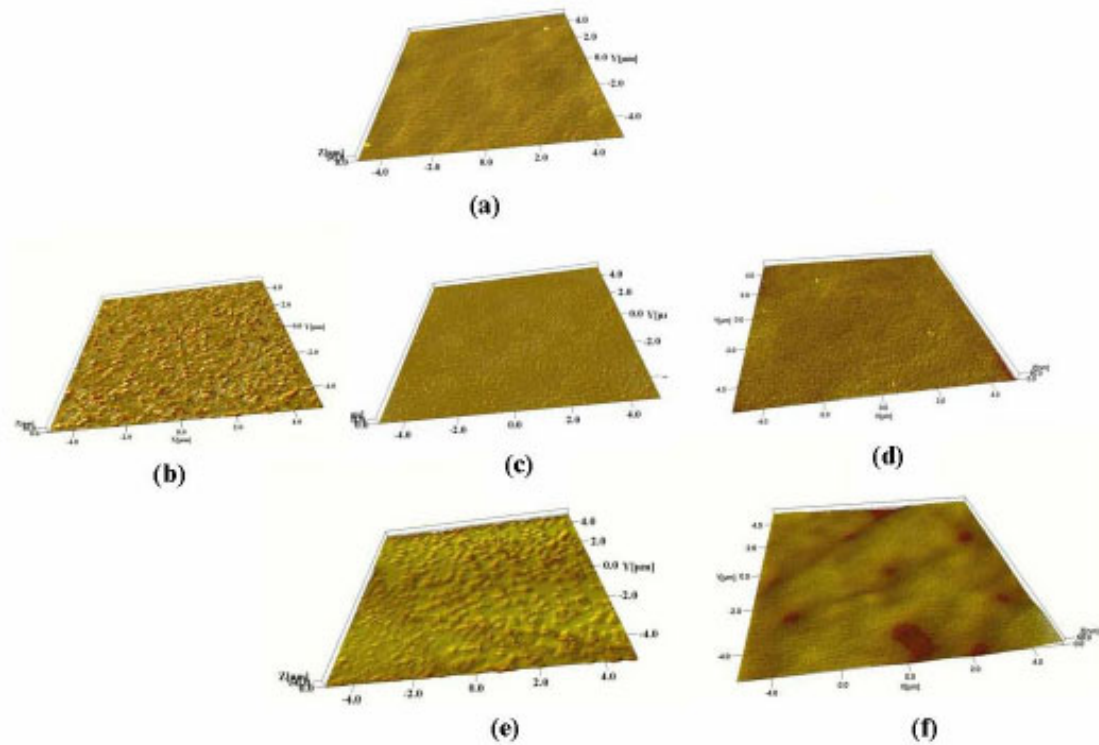


**Figure 38:** Tapping mode AFM images of: (a) an as-grown GaN surface (RMS = 0.3 nm); after 1300 °C / 5 s microwave annealing of GaN layers with (b) no cap (RMS =9.2 nm), (c) MgO cap (RMS =0.8 nm), and (d) AlN cap (RMS = 1 nm); (e) after 1400 °C / 5 s annealing with MgO cap (RMS = 7.2 nm); and (f) after 1500 °C/5 s annealing with AlN cap (RMS = 0.6 nm).

can be seen from Fig. 38(f) that the GaN surface of the 1500 °C/5 s microwave annealed sample, with an AlN cap in place appears very smooth with a RMS roughness (0.6 nm) comparable to the as-grown sample (0.3 nm). No evidence of any GaN decomposition can be seen for even this ultra-high-temperature AlN capped annealing. For comparison, the AFM image of a GaN sample annealed for 5 s at 1300 °C without any cap in place is shown in Fig. 38(b). Significant GaN decomposition resulting in the formation of hexagonal cavities can be observed in Fig. 38(b).

To summarize, ultra-fast microwave annealing was successfully used to anneal GaN epi-layers up to temperatures as high as 1500 °C using a protective PLD AlN capping layer. The PLD deposited AlN film is a much better capping layer to preserve the surface integrity of GaN at temperatures > 1300 °C compared to the e-beam deposited MgO film. It might seem that the MgO film might have cracked due to a greater lattice mismatch<sup>104</sup> between the GaN and MgO (~ 6.5%)<sup>105</sup> compared to the GaN and AlN (2.6%)<sup>106</sup>. However, x-ray diffraction scans (not shown) confirmed that the e-beam deposited MgO layer is fine-grain polycrystalline. Thus, the MgO layer should have plenty of grain boundaries to accommodate lattice or thermal co-efficient of expansion (TCE) mismatch without cracking. In fact, significant GaN decomposition was observed for the MgO capped sample annealed at 1350 °C, 50 °C before the MgO film cracked, whereas the AlN capped samples remained decomposition-free even after a 1500 °C treatment. It is known that the PLD process used to deposit the AlN cap results in a much better interface with the underlying GaN compared to the e-beam deposition process, which was used for the MgO cap formation. Thus, the presence of a large number of

voids at the MgO /GaN interface could have allowed the escape of nitrogen from the GaN film, which accelerated the decomposition of the GaN film. It would be interesting to explore pulsed laser deposited MgO caps for protecting the GaN surface during high-temperature microwave annealing.

In addition to the MgO and AlN caps, photoresist converted graphite caps were also explored to study their feasibility for protecting the GaN surface during high-temperature microwave annealing. Graphite caps have successfully protected SiC epilayers during ultra-high temperature (1700 - 1900 °C) microwave annealing of SiC<sup>73</sup>. However, in the present study it was found that for microwave annealing of GaN, the graphite caps started delaminating from the GaN surface at temperatures > 1000 °C, presumably because of the stress at the GaN/graphite interface, created by localized decomposition of the GaN epilayer under the graphite cap. From this study, it is evident that an excellent interface between the GaN and the capping layer is vital, if the GaN surface morphology is to be preserved during high-temperature annealing.

#### **3.2.4. Photoluminescence characterization**

Low-temperature (5 K) PL spectra on the in-situ Mg-doped GaN films annealed at 1300 °C and 1500 °C for a duration of 5 s, using AlN cap layer, are shown in Fig. 39. The PL spectrum from an as-grown (unannealed) sample is also shown in Fig. 39 for comparison. The only feature visible in the PL spectra from the as-grown sample is a broad band (3.0 -3.2 eV), with no phonon replicas. This band may be a superposition of at-least two components, the blue luminescence (BL) band<sup>107,108</sup> which is known to

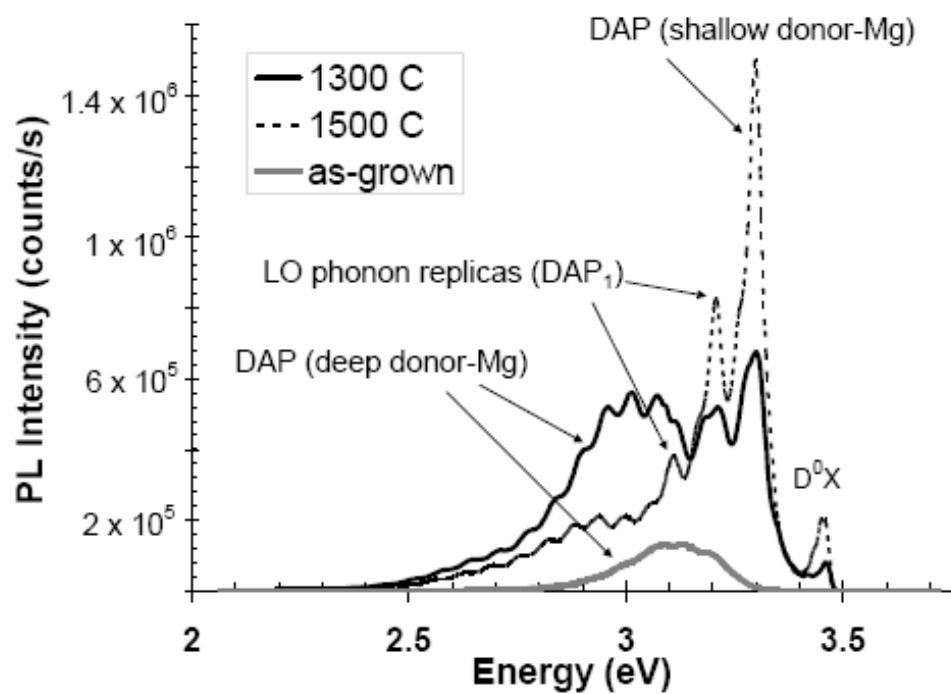


**Figure 39:** Low-temperature (5 K) PL spectra of as-grown Mg-doped GaN; and of AlN capped samples subjected to 5 s microwave annealing at 1300 °C and 1500 °C.

appear at 2.9 – 3.1 eV in heavily Mg-doped GaN grown by MOCVD and the ultraviolet luminescence (UVL) band<sup>107</sup>, which appears at 3.1 - 3.2 eV, also in heavily Mg-doped and compensated GaN. The BL band is supposed to be due to photo-excited carriers from a deep localized donor recombining with the shallow Mg acceptor<sup>109</sup>. The UVL band is supposed to originate from the DAP recombination between a shallow donor level (presumably  $O_N$ ) and the Mg acceptor<sup>105,107</sup>. The UVL band appears broad and featureless for the as-grown sample possibly due to potential fluctuations arising from the random distribution of charged impurities such as donors and acceptors, coupled with the fact that there are not enough free carriers to screen them<sup>107</sup>. For the sample annealed at 1300 °C, the relative intensity of the blue band reduces. The UVL band increases in intensity and is significantly blue shifted to yield a zero-phonon line (ZPL) at 3.27 eV along with its two LO phonon replicas at 3.18 eV and 3.09 eV. Also, a near band-edge emission peak<sup>107</sup> corresponding to the recombination of an exciton bound to a neutral donor ( $D^0X$ ) can also be observed from Fig. 39. A decrease in the intensity of the blue band and the appearance of the  $D^0X$  band indicate that the concentration of the compensating deep donors has reduced due to the microwave annealing, thus activating the Mg acceptors. This activation can be seen by the blue shift as well as the increase in both intensity and structure of the UVL band. For the sample annealed at 1500 °C, the relative intensity of the blue band decreases further, whereas the intensities of the UVL band and the near-band-edge emission band increase. This indicates that the 1500 °C / 5 s microwave annealing is more effective than the 1300 °C / 5 s annealing in reducing the concentration of the compensating deep donor levels and, therefore, in activating the Mg dopants.

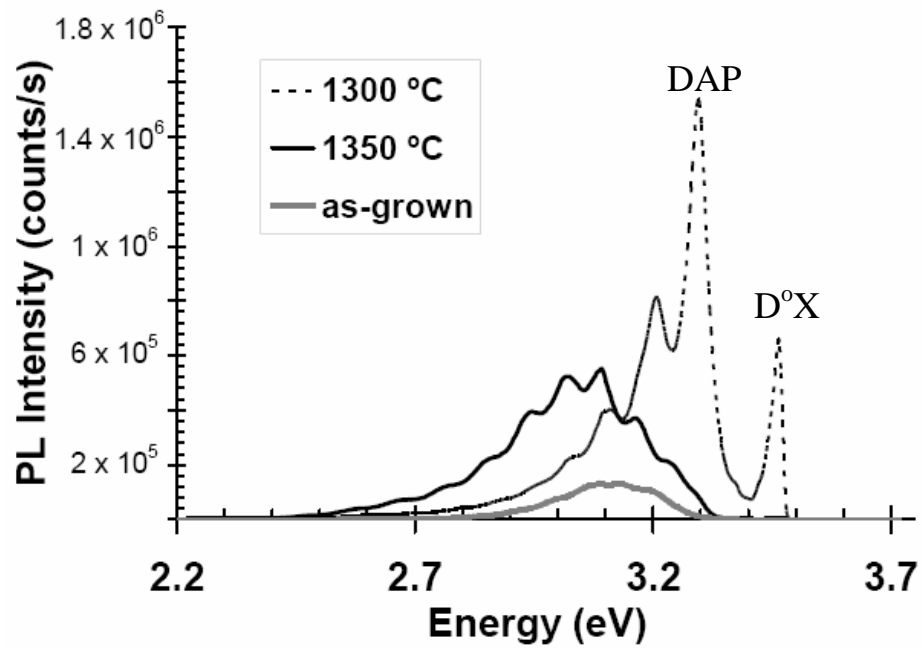


**Figure 40:** Low-temperature (5 K) PL spectra of as-grown Mg-doped GaN; and of e-beam deposited MgO capped in-situ Mg-doped GaN samples after 5 s microwave annealing at 1300 °C and 1350 °C.

Low-temperature PL spectra (shown in Fig. 40), on the microwave annealed samples with a MgO cap in place, indicate an increase in Mg activation for 1300 °C /5 s annealed sample by the presence of an intense, structured DAP UVL band at 3.29 eV (ZPL) as well as a strong near-band-edge emission ( $D^0X$ ) band at 3.46 eV. However, upon increasing the annealing temperature to 1350 °C, the  $D^0X$  band disappears, whereas a broad blue band (2.7 – 3.1 eV) is observed, which is red shifted even more than the 3.0 -3.2 eV band observed in the spectra of the as-grown sample. Since the AFM images did show a significant increase in GaN decomposition for the 1350 °C annealing, it is conceivable that this broad band originates from a number of deep donor-like defects (such as  $V_N$  [ $^{110}$ ]) which were created by the decomposition. A similar spectra (not shown) was also obtained for the 1400 °C / 5 s annealed sample, with the MgO cap in place.

The above PL results suggest that high-temperature (1500 °C) microwave annealing using AlN cap is very effective in increasing the net acceptor concentration by decreasing the concentration of the compensating deep donors in GaN.

### **3.2.5. Electrical Characterization**

A variation of the hole concentration (p) as a function of microwave annealing temperature, for the uncapped samples and for samples protected by the MgO and AlN caps during 5 s microwave annealing, is shown in Fig. 41. For both uncapped as well as MgO capped samples, the p decreases, when the annealing temperature is increased

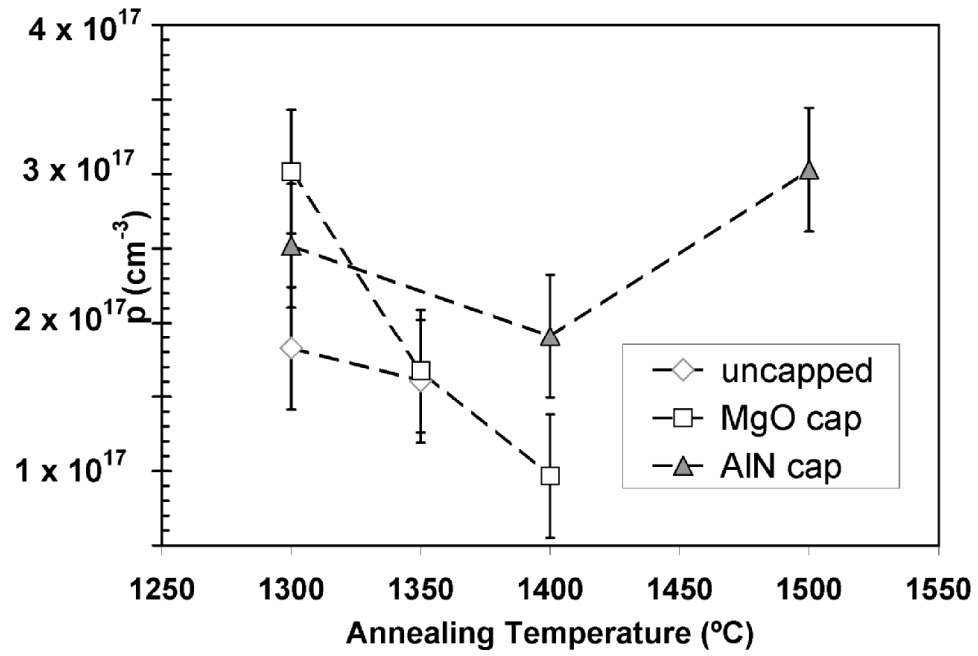


**Figure 41:** Hole concentration ( $p$ ) as a function of annealing temperature for 5 s duration microwave annealing on uncapped, MgO capped, and AlN capped in-situ Mg-doped GaN.

above 1300 °C. This is a direct result of increasing GaN decomposition with increasing annealing temperature for uncapped and MgO capped GaN layers, which was observed from the AFM images. The PL spectra for the MgO capped samples also indicated a decrease in Mg acceptor activation for the 1350 °C and 1400 °C anneals compared to the 1300 °C annealing, which agrees with the electrical results.

However, for the samples which were capped by the AlN during annealing, the highest  $p$  is measured for the 1500 °C annealing. Based on the above PL results, we believe that this is due to a decrease in the compensating deep donor concentration with increasing annealing temperature as long as the integrity of the GaN material is maintained. Relatively high hole mobilities of 14 – 19 cm<sup>2</sup>/V.s were measured on all the above-mentioned samples. We did not observe any change in the hole mobility after the microwave annealing treatment.

### **3.2.6 Conclusions from microwave annealing of in-situ Mg doped GaN**

Due to the ultra-fast heating/cooling rates of the microwave RTA system, the GaN can be successfully annealed in the temperature range of 1300 – 1500 °C, when the GaN is protected by a pulsed laser deposited AlN cap. The surface of the AlN capped GaN layer annealed at 1500 °C for 5 s is very smooth with a RMS roughness of 0.6 nm, which is comparable to the RMS roughness of 0.3 nm measured on the as-grown sample. The e-beam deposited MgO cap successfully protected the GaN surface during microwave annealing only up to 1300 °C, but a significant GaN decomposition is observed for the higher temperature anneals. Low-temperature (5 K) PL spectra and Hall

measurements performed on the AlN capped samples indicate that the 1500 °C / 5 s microwave annealing is more effective than the 1300 °C / 5 s microwave annealing in activating the Mg-dopant by decreasing the concentration of the compensating deep donor levels present in the as-grown sample. By comparison, fairly good luminescence and electrical results were obtained for the e-beam deposited MgO capped GaN layers only for annealing at 1300 °C, but the optical as well as electrical quality of the GaN layers degrade during higher-temperature (> 1300 °C) annealing. Photoresist converted graphite cap delaminates from the GaN surface for microwave annealing temperatures > 1000 °C and is therefore not a suitable capping material for high-temperature annealing of GaN.

### **3.3 Microwave annealing of Mg-implanted GaN**

After demonstrating improvement in the optical and electrical properties of in-situ Mg-doped GaN after high-temperature (1300 – 1500 °C) microwave annealing, the logical next step was to explore the feasibility of microwave annealing on Mg ion-implanted GaN. The Mg-implanted GaN layers could be used as the base region in a GaN heterojunction bipolar transistor (HBT). Also, selective Mg-implants through an implantation mask could be used to more easily create arrays of GaN LEDs and laser diodes as opposed to reactive ion etching p-type GaN epilayers.

#### **3.3.1 Implantation and annealing schedules**

The multiple energy Mg<sup>+</sup> implant schedule performed into undoped 3 μm GaN epilayers grown on a-plane sapphire is given in Table IX. The implantation was

performed at a temperature of 500 °C with a tilt of 7 °. As in case of SiC, the multiple energy Mg implant schedule for GaN was also designed using the SRIM -2006 software. A comparison of the simulated and the experimental (SIMS) Mg implant profiles is shown in Fig. 42. It can be observed from Fig. 42 that there is a significant discrepancy between the simulated and the experimentally determined Mg implant profiles. The simulation predicts a higher Mg concentration and a smaller ion penetration depth, whereas the experimentally measured profile displays a longer implant tail into the substrate. A similar discrepancy between simulated and experimental Si implant profiles in GaN was observed by Pearton et al<sup>3</sup>. Thus, some work will need to be done to obtain better stopping powers for implanted ions in GaN.

After implantation, the GaN epilayers were capped by a 0.3 µm layer of AlN grown by PLD and then subjected to microwave annealing in the range of 1300 – 1500 °C. After annealing, the AlN cap was etched by the H<sub>3</sub>PO<sub>4</sub> recipe, as described earlier. The reliable removal of the AlN caps after microwave annealing was again confirmed by the XPS measurements. After removing the cap, the Mg – implanted GaN epilayers were characterized for their structural and electrical properties, and also for the thermal stability of the implant.

### 3.3.2 SIMS depth profiling

SIMS depth profiles of the Mg implanted GaN before and after 1300 °C /5 s and 1400 °C / 5 s microwave annealing are shown in Fig. 43. The SIMS profile for the as-implanted sample and for the 1300 °C / 5 s annealed sample are close. However, a

**Table IX:** Multiple energy Mg implant schedule performed into undoped GaN

Implant Energy (keV)	Implant Dose (cm <sup>-2</sup> )
10	$3.8 \times 10^{13}$
25	$3.3 \times 10^{14}$
55	$1.7 \times 10^{14}$
110	$4.1 \times 10^{14}$
225	$8.3 \times 10^{14}$
300	$8.3 \times 10^{14}$

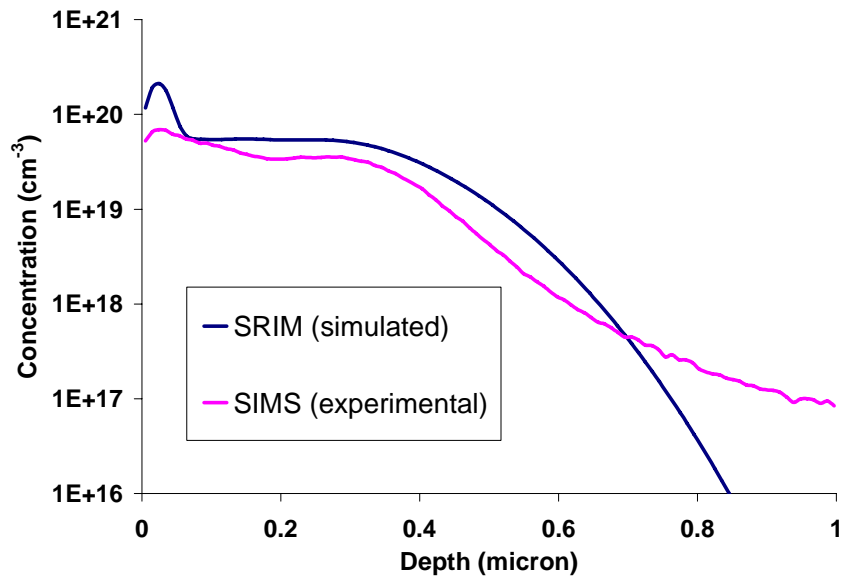


**Figure 42:** A comparison of simulated and experimental (as-implanted) Mg multiple energy implant profile in GaN

slight Mg accumulation at the surface and some in-diffusion of Mg into the GaN can be observed for the 1300 °C annealed sample. The microwave annealing at 1400 °C resulted in a significant Mg accumulation in a thin  $\approx 40$  nm surface layer, and a depletion of Mg at depths of 40 nm – 400 nm from the surface. A pronounced in-diffusion of Mg into the GaN can also be observed from Fig. 43 at depths beyond 400 nm. As indicated in Fig. 43, the extracted doses from the 1300 °C ( $1.6 \times 10^{15} \text{ cm}^{-2}$ ) and 1400 °C ( $1.5 \times 10^{15} \text{ cm}^{-2}$ ) annealed samples are slightly lower compared to the extracted dose ( $1.7 \times 10^{15} \text{ cm}^{-2}$ ) from the as-implanted sample. This is probably due to some out-diffusion of Mg into the AlN cap during the annealing treatment.

### 3.3.3 Photoluminescence characterization

Low-temperature PL spectra from Mg – implanted GaN, before and after 1400 °C / 5 s and 1500 °C / 5 s microwave annealing are shown in Fig. 44. For reference, the PL spectra from an as-grown GaN epilayer used for the Mg- implantation is also shown in Fig. 44. In addition to the near-band edge emission, a broad yellow luminescence (YL) band (2.0 eV – 2.6 eV) and a broad blue luminescence (BL) band (2.7 eV – 3.2 eV) also can be observed in the PL spectra obtained from the as-grown GaN epilayer. As discussed before, the appearance of BL in low-temperature PL spectra of GaN is

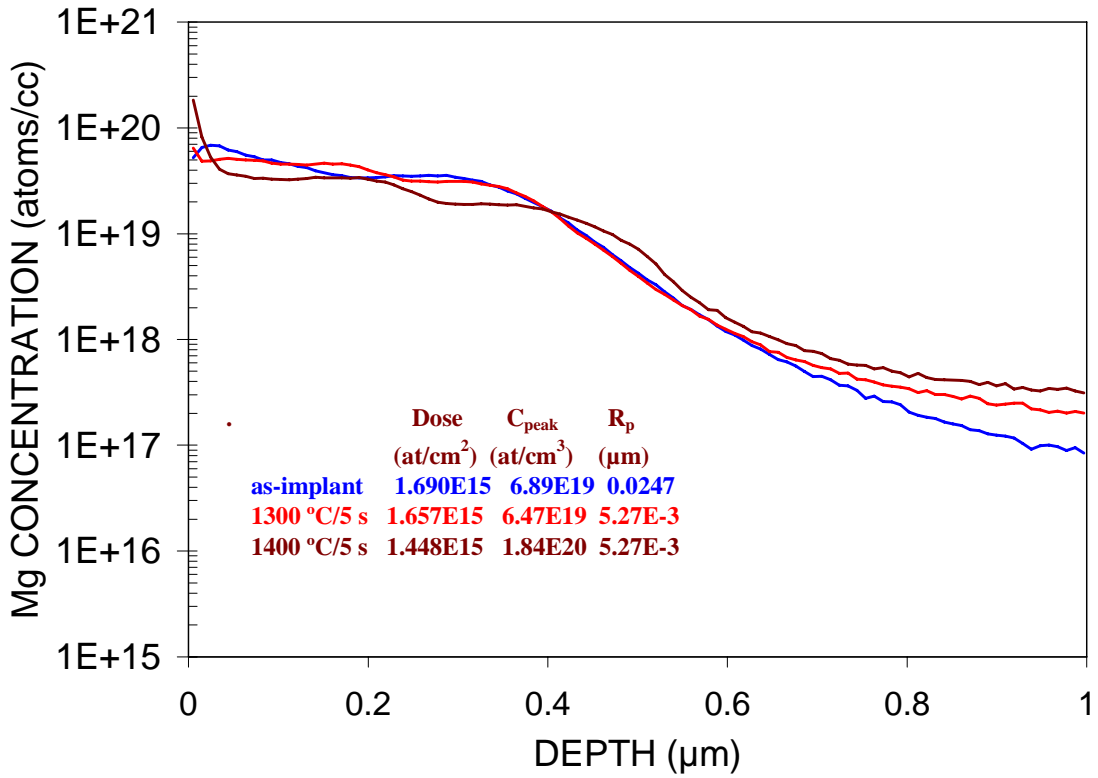


**Figure 43:** SIMS depth profiles of the Mg implanted GaN before and after 1300 °C /5 s and 1400 °C / 5 s microwave annealing

attributed to the presence of donor-like states in the bandgap, which may arise from  $V_N$  or pyramidal defects. The YL in GaN is generally attributed to the presence of C, O, and H in the material<sup>107</sup>. The presence of YL and BL in the PL spectra indicates a poor quality GaN material, especially for p-type doping, since the YL and BL can severely compensate the activated acceptors.

The as-implanted GaN does not exhibit any photoluminescence, since the implant-induced damage introduces a lot of defect levels in the bandgap, which act as non-radiative recombination centers. The PL spectra from the 1400 °C microwave annealed GaN does show the re-appearance of the near band-edge  $D^0X$  emission as well as DAP emission related to Mg activation. Thus, microwave annealing at 1400 °C at-least partially heals the implant-induced lattice damage. Increasing the annealing temperature to 1500 °C results in further recovery of implant-induced damage as can be seen from the increase in intensity of both  $D^0X$  emission and Mg activation related DAP emission from the PL spectra (Fig. 44). However, the YL and BL bands can also be seen in the PL spectra of microwave annealed samples, which possibly precludes any electrical activation due to compensation of the activated acceptors. Thus, it is paramount to have an excellent quality GaN epilayer which doesn't emit YL and BL, especially for fabricating device structures which require p-type implantation.

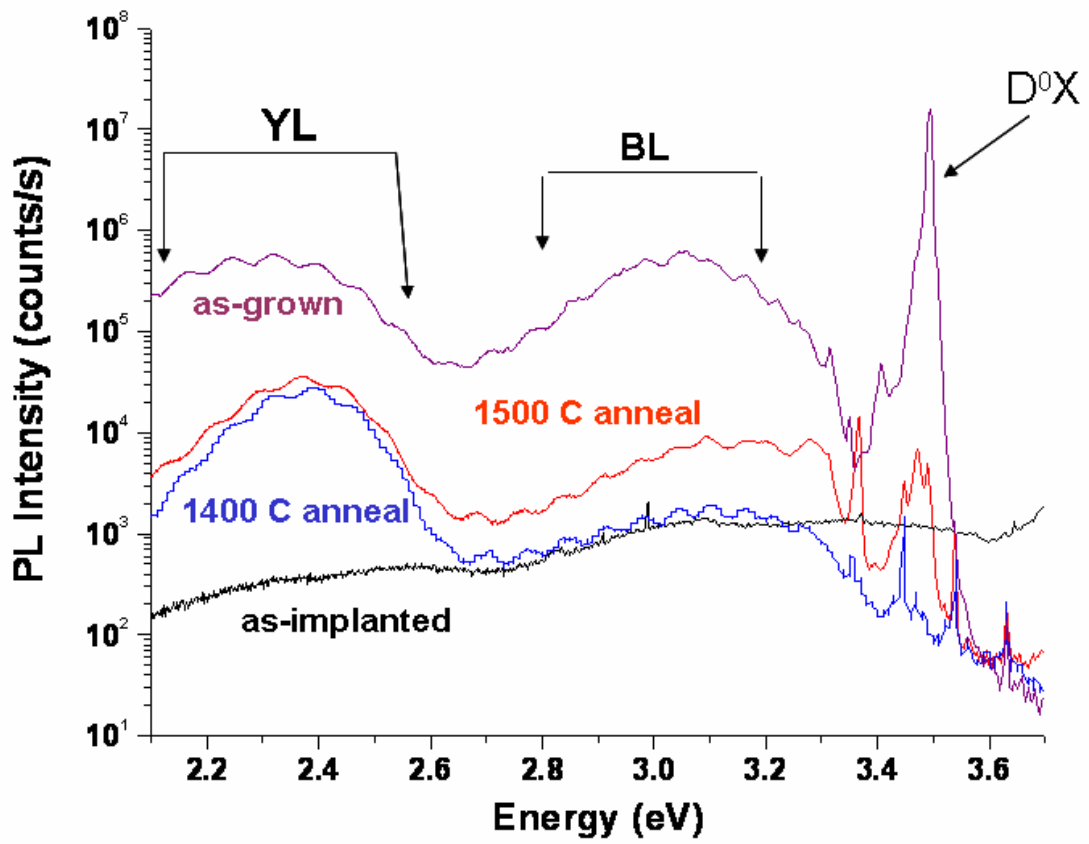


Figure 44: Low-temperature (5 K) PL spectra from an un-implanted GaN epilayer, and GaN epilayers before and after 1400 °C / 5 s and 1500 °C / 5 s microwave annealing.

### **3.3.4 Electrical characterization**

Electrical characterization of the GaN even after a 1500 °C annealing treatment has indicated almost no electrical activation of Mg. The samples are highly resistive. This is likely due to the significant lattice damage created by the high dose, multiple energy Mg implant. Also, the PL spectra (Fig. 44) have indicated the presence of compensating deep levels even in the as-grown GaN epilayer. The combination of the poor starting

### **3.4 Summary and suggested future work on microwave annealing of GaN**

In summary, GaN epilayers were reliably annealed at high-temperatures in the range of 1300 -1500 °C, when the GaN is protected by a PLD AlN cap. Promising electrical and optical results were obtained for in-situ Mg doped epilayers. However, it has proven to be more challenging to activate a multiple energy, high dose Mg implanted GaN. Significant lattice damage exists even after annealing at temperatures as high as 1500 °C, albeit for short 5 s durations. Lower dose single-energy Mg implantations are planned on GaN epilayers, which are of a much higher quality than the ones explored in the present study.

Future work involves ultra-high temperature annealing of Si (n-type) implanted GaN and especially AlGaN epilayers grown on SiC. If successful, such layers can be used under source/drain metal contacts of AlGaN- GaN HEMT devices, in an attempt to lower the source/drain access resistance, and to increase the device transconductance. Also, future high-temperature microwave anneals are planned on in-situ Mg doped  $\text{Al}_{0.25}\text{Ga}_{0.75}\text{N}$  and  $\text{Al}_{0.4}\text{Ga}_{0.6}\text{N}$  grown on sapphire. Increasing the Al content in the AlGaN

ternary increases the bandgap and finds application in smaller wavelength laser diodes. However, the increasing Al content in AlGaIn also makes p-type doping more difficult to achieve.

## 4. SILICON CARBIDE NANOWIRES

### 4.1 Introduction

In this work, a new method for the growth of 3C-SiC nanowires by a novel catalyst-assisted sublimation-sandwich (SS) method was developed. For heating, an ultra-fast microwave heating technique developed by LT technologies was employed. Different morphologies of 1-D SiC nanostructures were grown by appropriately adjusting the process parameters. The as-grown nanowires were characterized using field-emission scanning electron microscopy (FESEM), energy dispersive x-ray spectroscopy (EDAX), electron backscattered diffraction (EBSD), transmission electron microscopy (TEM), and micro-Raman spectroscopy.

### 4.2 Sublimation-sandwich method developed in this work to grow SiC nanowires

A detailed description of the solid-state microwave heating system used in this work is provided in the introduction chapter. This microwave heating system was primarily designed for post-implantation annealing of ion-implanted SiC<sup>51,63,73</sup>. A schematic of a typical “sandwich” cell employed in this work for SiC nanowire growth is shown in Fig. 45. The ‘sandwich cell’ in Fig. 45 consists of two parallel 4H-SiC wafers with a very small gap, ‘*d*’, between them. The bottom wafer in Fig. 45 is semi-insulating

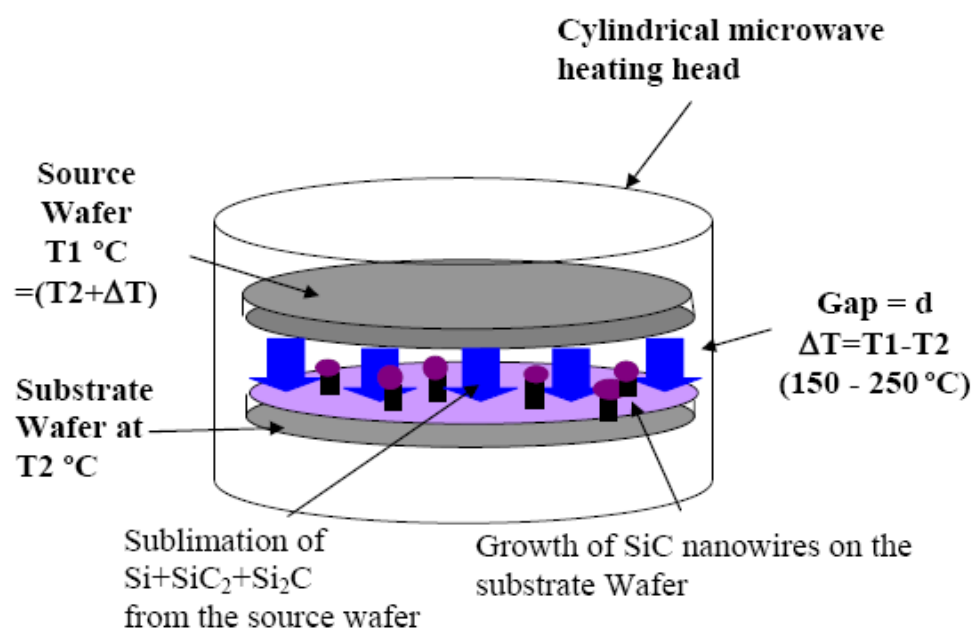


**Figure 45:** Schematic of the ‘sublimation-sandwich’ cell used to grow SiC nanowires

SiC, which will be referred to as the '*substrate wafer*' hereafter. The inner surface of the *substrate wafer* is coated with a 5 nm layer of Fe, Ni, Pd, or Pt that acts as a catalyst for the VLS growth of SiC nanowires. The top wafer in Fig. 45 is a heavily n-type (nitrogen doped) *in-situ* doped SiC, which will be referred to as the '*source wafer*'. As shown in Fig. 45, the microwave heating head is placed around the sandwich cell. Due to the difference in electrical conductivity of the *source wafer* and the *substrate wafer*, at a given microwave power, the *source wafer* temperature is higher than the *substrate wafer* temperature, resulting in a temperature gradient,  $\Delta T$  between the two wafers. When the Si- and C-containing species, such as Si, SiC<sub>2</sub>, and Si<sub>2</sub>C sublime from the *source wafer* at temperatures > 1500 °C, the temperature gradient  $\Delta T$  provides the driving force for transporting these species to the *substrate wafer*. On the *substrate wafer* surface, the metal film is either already molten at the growth temperature, or it melts after absorbing the Si species and forms spherical islands to minimize its surface free energy. The Si- and C-containing vapor species are absorbed by these metal islands, converting them into liquid droplets of metal-Si-C alloys. Once this alloy reaches a saturation point for SiC, a precipitation of SiC occurs at the liquid-substrate interface thereby leading to a VLS growth<sup>111</sup> of the SiC nanowires. The nanowires always terminate in hemispherical metal-Si alloy end-caps. While group VIII metals facilitated growth of SiC nanowires, Au was unsuccessful as a catalyst in this VLS process. No traces of Au on the sample surface were found during a post-growth SEM/EDAX inspection, due to its possible evaporation at the growth temperature. In this dissertation, the results obtained using Fe as a metal

catalyst are presented since SiC growth using other Group VIII metals produced similar results.

#### **4.3 Unique features of the sublimation-sandwich method used in this work compared to other techniques employed for nanowire growth**

The sublimation sandwich method used in this work can reliably grow SiC nanostructures with predictable morphologies, with very high growth rates, using a well-known sublimation sandwich method, which is used in industry for growing SiC epilayers and substrates. As a result, there exists a vast body of information available for controlling the polytype, doping, orientation, etc. of the SiC growth. The sandwich cell used in this work is a nearly closed system because of the small gap between the source and substrates wafers, which allows precise control of the composition of the vapor phase in the growth cell. At the same time the system is open to the species exchange between the sandwich growth cell and the surrounding environment in the chamber. By appropriately adjusting the composition of the precursor species in the vapor, this approach has the potential to control the doping levels, or create heterostructures in the growing nanostructures. Another important feature of the sandwich growth cell is its compact size, which significantly reduces the volume of the surrounding chamber. The use of a small chamber not only saves the cost by utilization of small amount of expensive source materials, but also significantly reduces the vacuum pumping cycle time, which is needed for a high throughput fabrication. Yet another novel feature is the dynamic range of temperature ramping rates ( $\geq 600$  °C/s) that are possible using the

microwave heating system. This is another process parameter which can be tweaked to circumvent some thermodynamic restrictions.

#### **4.4 Experimental parameters related to SiC nanostructure growth**

The *substrate wafer* temperature window for growing SiC nanostructures is 1550 °C to 1750 °C. In this growth method, the precursor Si and C containing species sublime from the *source wafer*. Significant sublimation of Si and C species from a SiC wafer requires temperatures  $> 1400$  °C (at 1 atm pressure). Therefore, the growth temperatures used in this work are higher than those typically employed<sup>20-29</sup> for SiC nanowire growth (1000 °C – 1200 °C), since the previous works did not employ sublimated Si and C containing species from a SiC wafer as the source material. The growth is performed for time durations of 15 s to 40 s. The  $\Delta T$  between the *source wafer* and the *substrate wafer* is varied from 150 °C to 250 °C by varying the spacing (d) from 300  $\mu\text{m}$  to 600  $\mu\text{m}$ . All the growth experiments are performed in an atmosphere of UHP-grade nitrogen. Growth was also attempted in other inert gases such as Ar, He and Xe, but they were found to ionize due to the intense microwave field in the growth chamber.

#### **4.5 Experimental apparatus used for characterizing SiC nanostructures**

A Hitachi S-4700 field emission scanning electron microscope (FESEM) was used for studying the surface morphology of the SiC nanowires. An EDAX attachment to the S-4700 microscope was used to determine chemical composition, and a HKL Nordlys II EBSD detector attached to the S-4700 microscope was used to collect the electron

backscatter diffraction (EBSD) patterns. X-ray diffraction was performed using a Bruker D8 x-ray diffractometer equipped with an area detector. Samples for transmission electron microscopy (TEM) were prepared by dispersing nanowires on lacey carbon-coated copper grids. The samples were examined in a Philips CM-30 TEM operated at 200 kV. Samples for  $\mu$ -Raman spectroscopy were prepared by dispersing the SiC nanowires on an *a*-plane sapphire substrate. Raman spectra were obtained with 514.5 nm excitation (argon ion laser) in a back-scattering configuration using a custom-built Raman microprobe system. Incident laser radiation was delivered to the microprobe using a single mode optical fiber, resulting in a depolarized radiation exiting the fiber (no subsequent attempt was made to polarize the radiation). Radiation was introduced into the microscope optical path using an angled dielectric edge filter in the so-called injection-rejection configuration. Collected scattered radiation was delivered to a 0.5 m focal length imaging single spectrograph using a multimode optical fiber. A 100X infinity-corrected microscope objective was used for focusing incident radiation and collecting scattered radiation. Power levels at the sample were less than 1.6 mW. Light was detected with a back-illuminated, charge coupled device camera system operating at -90 °C. The instrumental bandpass (FWHM) was approximately 3.1  $\text{cm}^{-1}$ .

#### **4.6 Morphology and chemical composition of SiC nanowires**

Growth of SiC nanowires was observed over a very narrow range of both substrate temperature ' $T_s$ ' (1650 °C -1750 °C) and  $\Delta T$  ( $\approx 150$  °C). A plan-view FESEM image of the nanowires grown at 1700 °C for 40 s is shown in Fig. 46. The growth and structural

characterization of these nanowires, which are 10  $\mu\text{m}$  to 30  $\mu\text{m}$  long, is the main focus of this work. Typical 3C-SiC nanowire lengths reported in the literature<sup>20-29</sup> range from as short as 1  $\mu\text{m}$  to as long as several mm. The diameters of the nanowires grown in this work are in the range of 15 nm to 300 nm. EDAX analysis of the nanowires (not shown) indicates that they mainly consist of Si and C with traces of nitrogen. The likely source of this nitrogen is the ambient atmosphere, however the source wafer is also doped with nitrogen ( $N_D = 1 \times 10^{19} \text{ cm}^{-3}$ ). The exact mechanism of the accommodation of nitrogen in SiC nanowires requires further investigation. EDAX spectra (not shown) from the droplets at the nanowire tips consist of the corresponding metal and Si.

The statistical distribution of the nanowire diameters was determined using FESEM images of nanowire samples dispersed on a low-resistivity Si wafer. The diameters of 50 nanowires were measured at different locations on the wafer. The diameter distribution for the SiC nanowires grown at 1700  $^{\circ}\text{C}$  for 40 s (Fig. 47) reveals that 42 % of the nanowires exhibited diameters in the range of 15 nm to 100 nm while 14% of nanowires had diameters in excess of 300 nm.

In addition to SiC nanowires, growth of cone-shaped and needle-shaped SiC nanostructures was also observed under different growth conditions. For  $\Delta T=150$   $^{\circ}\text{C}$ , the *substrate wafer* temperatures in the range of 1550  $^{\circ}\text{C}$  to 1650  $^{\circ}\text{C}$  for 15 s to 1 min durations yielded mainly cone-shaped quasi 1-D SiC nanostructures (Fig. 48(a)) which are 2  $\mu\text{m}$  – 5  $\mu\text{m}$  long, whereas *substrate wafer* temperatures  $> 1750$   $^{\circ}\text{C}$  for the same durations resulted in micron-sized SiC deposits (not shown). The “nanocones” shown in Fig. 47(a) taper off along their axis from thick catalytic metal tips. This suggests that the

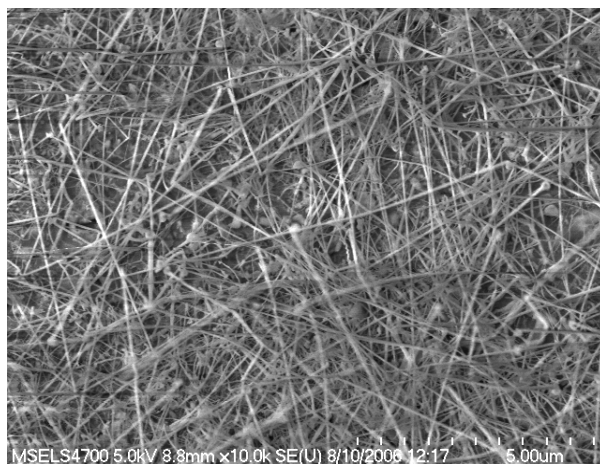


**Figure 46:** FESEM image of SiC nanowires grown at  $T_s = 1700\text{ }^\circ\text{C}$  and  $\Delta T = 150\text{ }^\circ\text{C}$  for 40 s.

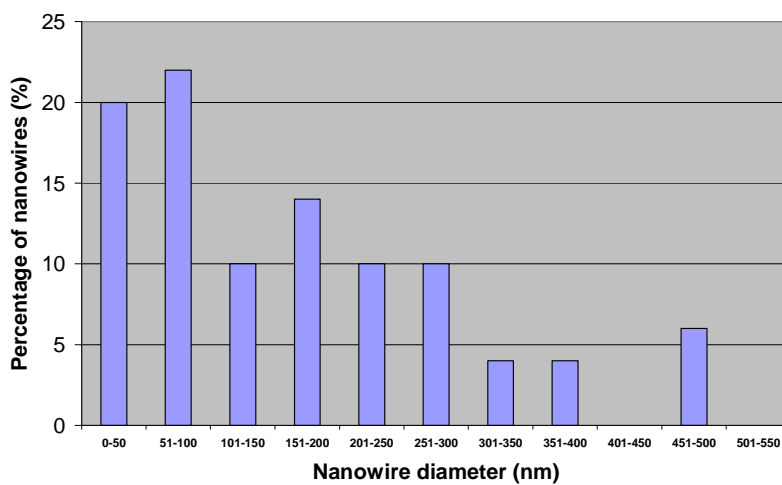
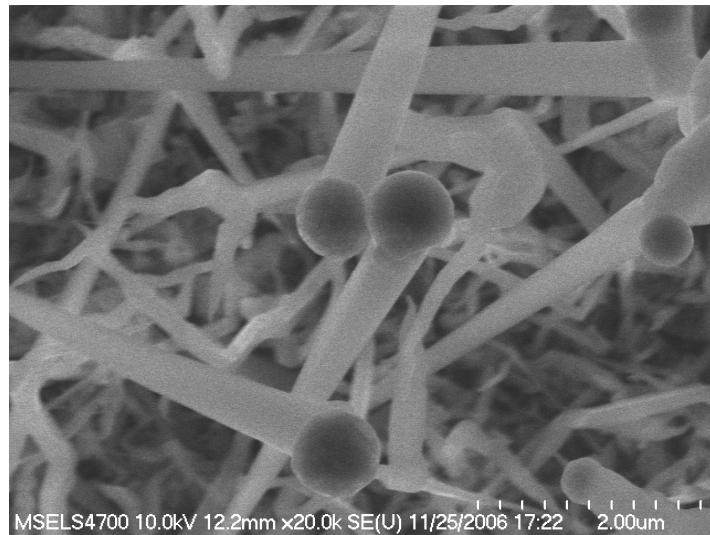


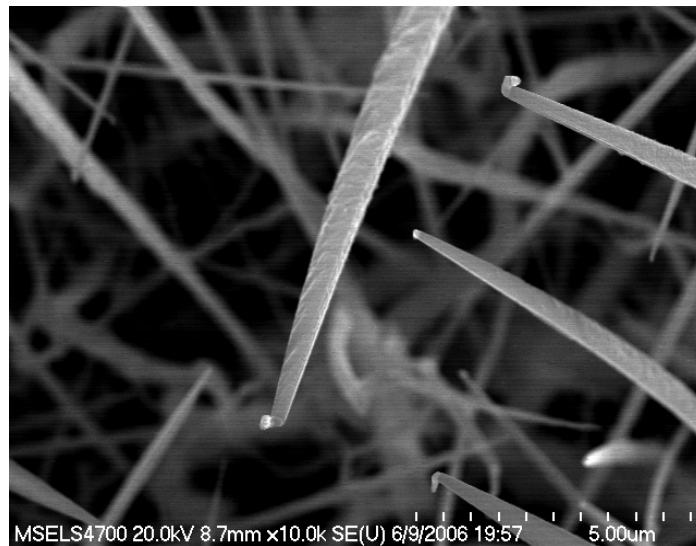
**Figure 47:** Statistical distribution of the SiC nanowire diameters. About 42% of the nanowires have diameters  $\leq 100\text{ nm}$ .

diameter of the droplets increased during the growth of the cones. The diameters of their thin ends are about 10 nm to 30 nm, while the broad portion at the top just under the catalytic metal tips, range from 100 nm to 200 nm. The fact that the diameter of the cones increases with growth duration must mean that there is an Oswald ripening effect, i.e. the metal is transferred from the smaller diameter droplets to the larger diameter ones, possibly via surface diffusion<sup>112</sup>. The short length of the cones results from a relatively low SiC growth rate for the experimental conditions under which the cones are grown. Thus the surface diffusion length for the liquid metal to flow from the smaller diameter droplets to the larger diameter droplets is short.

Increasing the  $\Delta T$  to 250 °C (by increasing ' $d$ ' from 300  $\mu\text{m}$  to 600  $\mu\text{m}$ ) at a  $T_s$  of 1700 °C resulted in mainly needle-shaped SiC nanostructures (Fig. 48(b)), which are 50  $\mu\text{m}$  – 100  $\mu\text{m}$  in length. These needles are narrow under the catalytic metal tips. It is obvious that the diameter of the metal droplets catalyzing the needle growth decreases with growth duration. Because the source wafer temperature for needle growth (1900 °C – 2000 °C) is the highest among the temperatures explored in this work, it is possible that the metal droplets evaporate during crystal growth due to high temperatures in the vicinity of the droplets. The much longer needles (in comparison with the cones) also results in a greater surface diffusion length for the liquid metal to flow between droplets, which might have inhibited significant surface diffusion of the metal.



(a)



(b)

**Figure 48:** (a) Cone-shaped SiC nanostructures grown at  $T_s = 1600\text{ }^\circ\text{C}$  and  $\Delta T = 150\text{ }^\circ\text{C}$ .

(b) Needle-shaped SiC nanostructures grown at  $T_s = 1700\text{ }^\circ\text{C}$  and  $\Delta T = 250\text{ }^\circ\text{C}$

#### 4.7 Crystallography of the SiC nanowires

A typical  $\theta$ - $2\theta$  powder x-ray diffraction spectrum obtained from the SiC nanowires is shown in Fig. 49. The only phase unambiguously identified from the XRD spectrum is 3C-SiC. EBSD patterns from the SiC nanowire and catalytic cap shown in Fig. 50(a) are presented in Fig. 50(b) and 50(c), respectively. The EBSD pattern from the nanowire was successfully indexed to 3C SiC and not one of the hexagonal variants (2H, 4H, etc.) or rhombohedral variants (e.g. 15R). This distinction relies on the presence and/or absence of relatively weak lines in the EBSD spectra, but the result was unequivocal. The growth direction of the nanowire was identified as  $\langle 112 \rangle$  which is in contrast to the  $\langle 111 \rangle$  growth direction commonly observed for 3C SiC nanowires<sup>5,7,8-10,11-22</sup>. The EBSD pattern from the catalytic tip of the SiC nanowire, which clearly shows the six-fold symmetry about the c-axis, was indexed according to the hexagonal Fe<sub>2</sub>Si phase. One of the reasons as to why the  $\langle 112 \rangle$  growth direction is preferred for the SiC nanowires grown in this work over the commonly reported  $\langle 111 \rangle$  direction could be the very high temperatures (1650 °C – 1750 °C) used in this work for nanowire growth. The nanowire growth generally occurs along the direction, whose corresponding face has the highest surface energy, so that that particular face is not exposed. The  $\{111\}$  being a three cluster face must have a higher surface energy for SiC at lower temperatures, thereby driving the nanowire growth along the  $\langle 111 \rangle$  direction. At higher temperatures, the nucleation rate along directions normal to lower atomic density planes such as  $\{110\}$  and  $\{112\}$  is known to be faster than  $\{111\}$ . Pampuch et al.<sup>19</sup> observed 3C-SiC nanowire growth direction switched from  $\langle 111 \rangle$  to  $\langle 110 \rangle$ , when the growth temperature was

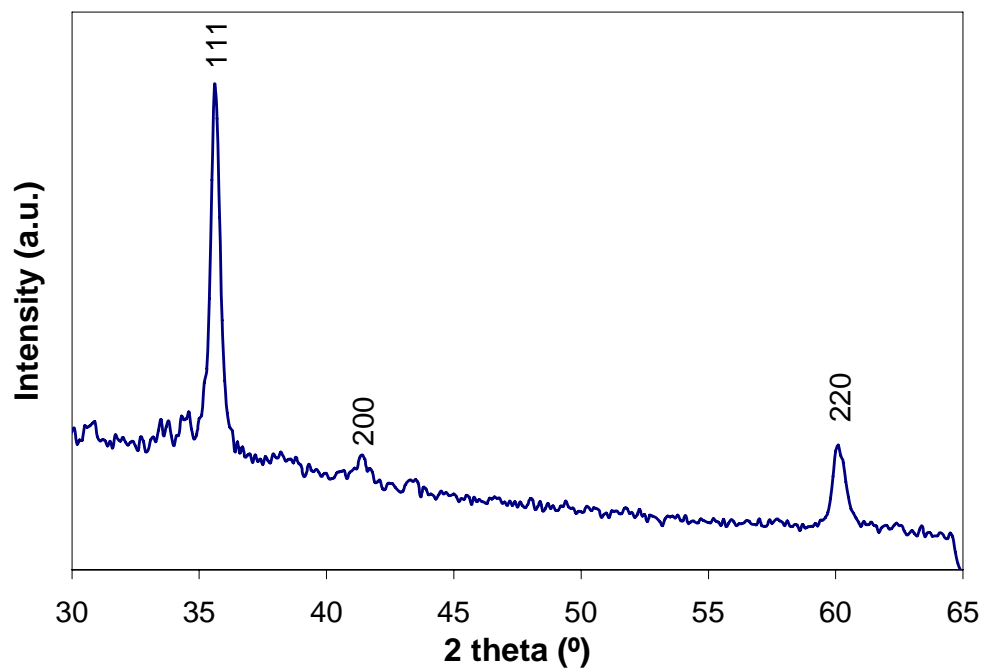


**Figure 49:** A typical x-ray diffraction spectrum obtained from the SiC nanowires grown in this work.

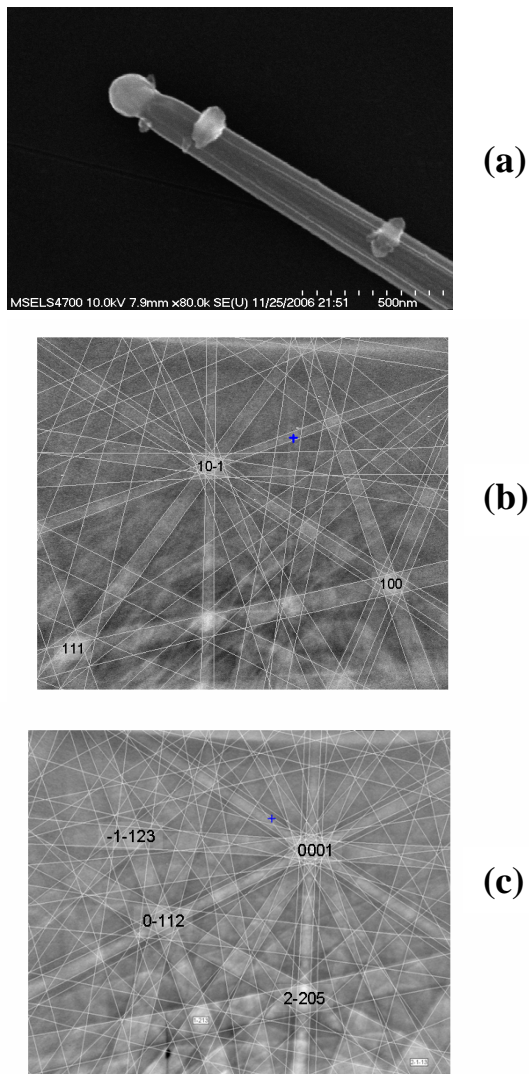


**Figure 50** (a) FESEM image of a SiC nanowire harvested on a heavily doped Si substrate. (b) EBSD pattern from the nanowire indexed to the 3C-SiC phase. (c) EBSD pattern from the nanowire tip indexed to Fe<sub>2</sub>Si.

increased beyond 1500 °C.

The occurrence of different polytypes dependent on the temperature has been studied in sublimation experiments under near-equilibrium conditions<sup>113</sup>. Factors affecting the crystal polytype are the temperature and the pressure in the growth chamber, the polarity of the seed crystal, the presence of certain impurities and the Si/C ratio. Under more Si-rich (C-rich) conditions the formation of the cubic (hexagonal) polytype should be preferred<sup>114</sup>. Nucleation far from equilibrium conditions and a nitrogen atmosphere has been generally assumed to stabilize the cubic polytype<sup>115-117</sup>. This is supported by nucleation theory. Furthermore, 3C SiC has the lowest surface energy among all polytypes. Since, in the experiments of this work, Si- rich precursor species are present (Si, Si<sub>2</sub>C), and nucleation occurs far from equilibrium conditions in a nitrogen atmosphere, the growth of 3C-SiC is to be expected from the above considerations. Furthermore, since nanowires have a large surface to volume ratio, the low surface energy of the 3C-SiC polytype makes it much more favorable to grow 3C-SiC over other polytypes.

As mentioned before, SiC nanowire growth was successfully performed by using other group VIII metal catalysts such as Ni, Pd, and Pt, in addition to Fe. In each case, the EBSD patterns from the nanowires were indexed to 3C-SiC and the growth direction of the nanowire was identified as parallel to the  $\langle 112 \rangle$  crystallographic directions, which indicates the unique  $\langle 112 \rangle$  growth direction observed for SiC nanowire growth in this work does not depend on the metal catalyst used for the growth. EBSD patterns from the end-caps of the nanowires grown using Ni, Pd, and Pt are shown in Fig. 51(a), 51(b), and

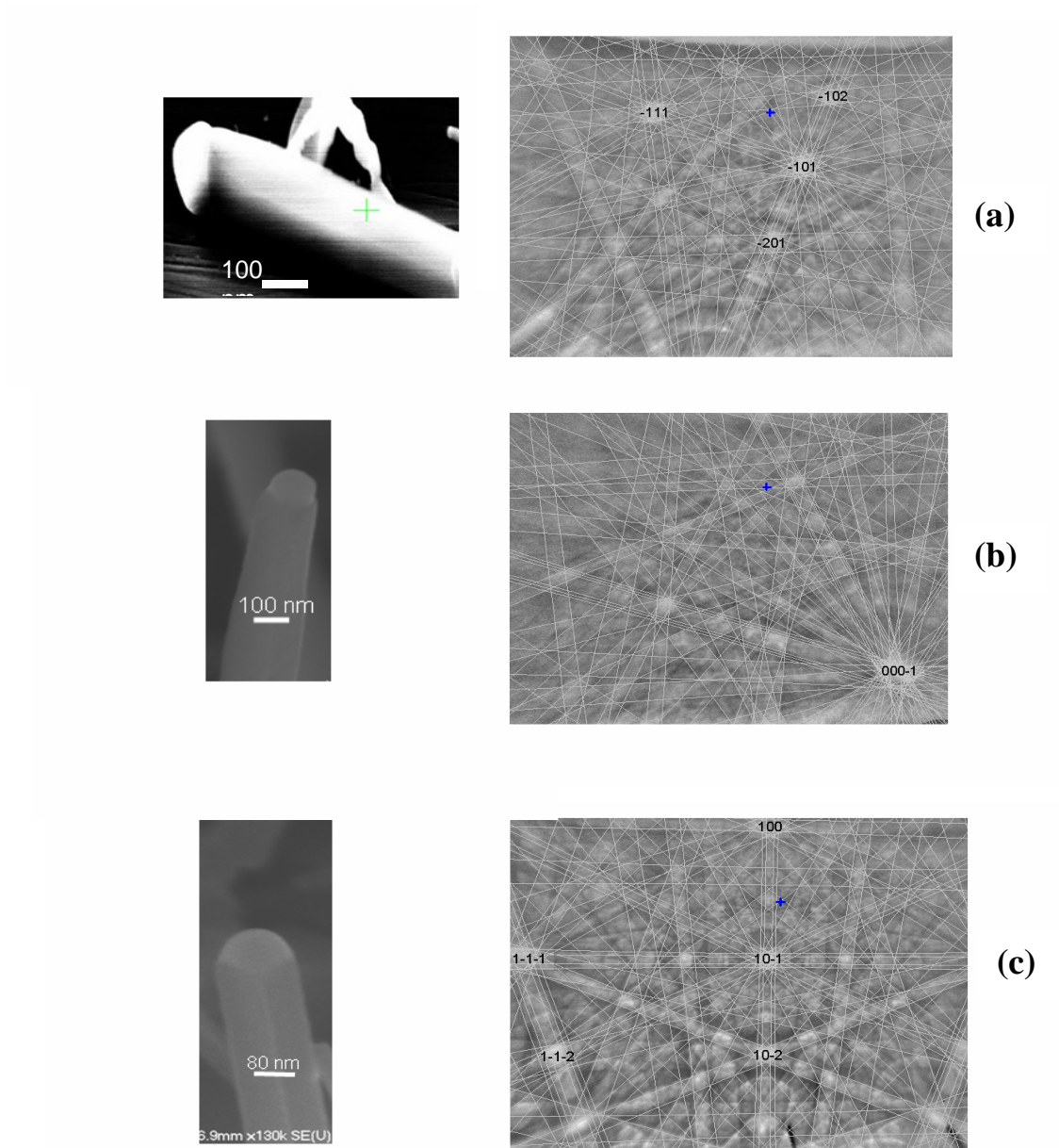


**Figure 51:** EBSD patterns from the catalytic tip of the SiC nanowires grown using (a) Ni catalyst. (EBSD pattern indexed to  $\text{Ni}_3\text{Si}$ ) (b) Pd catalyst (EBSD pattern indexed to  $\text{Pd}_2\text{Si}$ ). (c) Pt catalyst (EBSD pattern indexed to  $\text{PtSi}$ ).

51(c), respectively, and were indexed to Ni<sub>3</sub>Si, Pd<sub>2</sub>Si, and PtSi phases respectively. It should be pointed out that a much higher density of nanowires in comparison with other 2-D deposits are observed for the growth performed using Fe, Ni, and Pd. It was still possible to grow SiC nanowires using Pt as well, but the yield of the nanowires in comparison with other 2-D deposits was much lower. This can be possibly attributed to the higher melting point of the Pt-Si alloys compared to other metals used in this work. However, no major difference in the structural characteristics of the nanowires grown using the different metal catalysts were observed.

Selected area electron diffraction patterns (Fig. 52) recorded from 10 nanowires were all consistent with a cubic 3C-SiC structure. The growth direction is parallel to  $\langle 112 \rangle$ , as was inferred from the nanowire projections in several zone axis orientations, which is consistent with EBSD results. At-least two different types of SiC nanowires were observed under TEM. Diffraction contrast TEM images representative of these two types of nanowires are shown in Fig. 53. The nanowire shown in Fig. 53(a) exhibits twinning on four non-equivalent  $\{111\}$  planes, with the growth direction switching among the  $\langle 112 \rangle$  directions in these planes ( $\approx 70^\circ$  apart), which creates an impression of nanowire bending. The nanowire shown in Fig. 53(b) is relatively straight but features a high-incidence of planar  $\{111\}$  defects (presumably, stacking faults and/or twins) parallel to the growth axis. It must be pointed out that even though an image of a thin (50 nm diameter) straight nanowire and a thick (500 nm diameter) bent nanowire are shown in Fig. 53, the nanowire diameter has no bearing on whether a nanowire is straight or bent. Thick, straight nanowires and thin bent nanowires have also been observed.

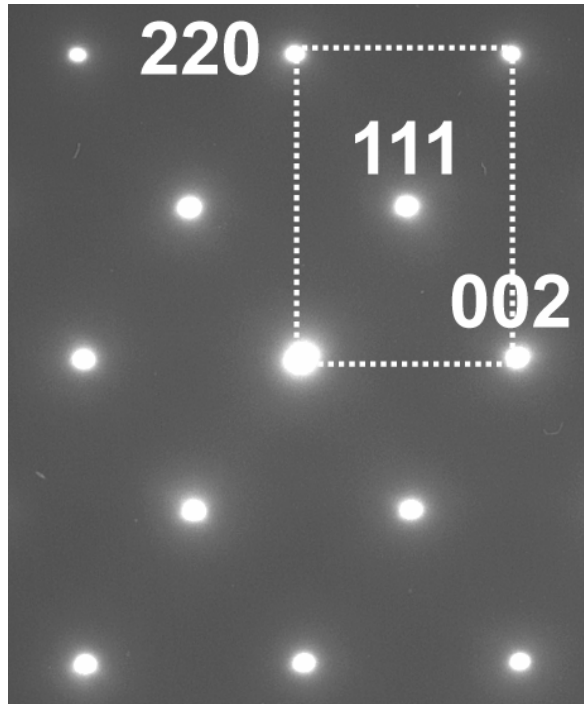


**Figure 52:** Representative  $\langle 101 \rangle$  selected area electron diffraction pattern recorded from a single SiC nanowire. The reflections are indexed according to the F-centered cubic 3C-SiC unit cell.

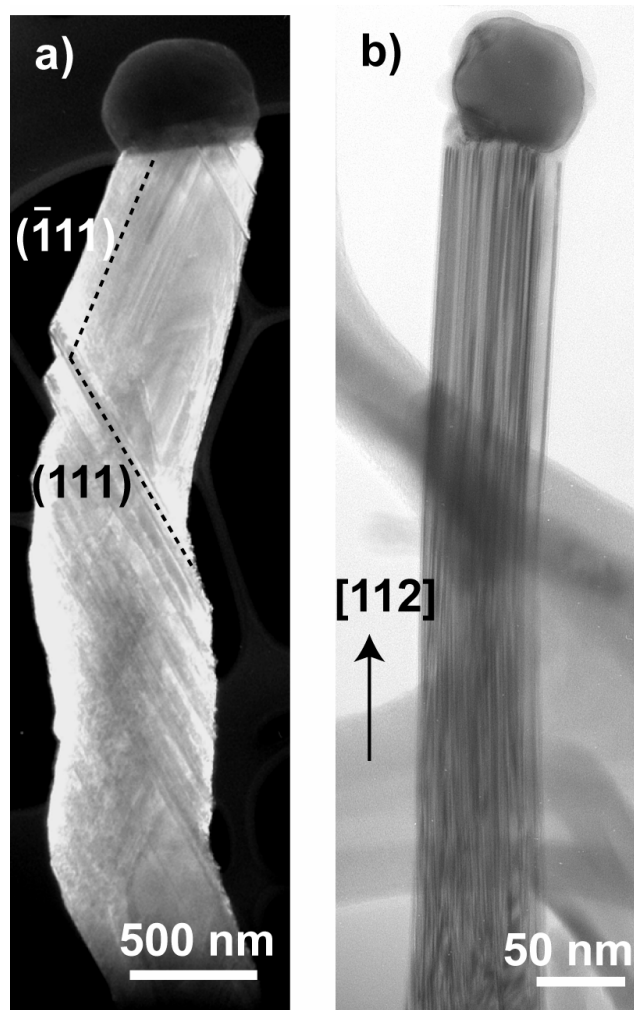


**Figure 53:** Diffraction contrast TEM images of two types of 3C-SiC nanowires. (a) twin-like defects are observed on different sets of  $\{111\}$  planes. The twinning was confirmed through the selected area electron diffraction patterns (not shown). (b) High-incidence of planar defects parallel to  $\{111\}$  planes along the wire axis. These defects produced streaks of diffuse intensity along the  $\langle 111 \rangle$  direction in electron diffraction patterns.

#### 4.8 Raman study of the SiC nanowires

Figure 54 shows a typical micro-Raman spectrum obtained from an isolated SiC nanowire. The most intense feature in Fig. 54 is observed at  $\approx 800 \text{ cm}^{-1}$  and is attributed to zone center transverse optical (TO) phonon modes in 3C-SiC. This feature is composed of at least two peaks with center wavenumbers of  $\approx 794 \text{ cm}^{-1}$  and  $\approx 810 \text{ cm}^{-1}$  (obtained by performing a peak deconvolution assuming only two peaks) and exhibits a shoulder at  $\approx 756 \text{ cm}^{-1}$ . In comparison, bulk 3C-SiC Raman spectra exhibit only one TO mode<sup>118,119</sup> at  $\approx 796 \text{ cm}^{-1}$ . The TO phonon mode at  $794 \text{ cm}^{-1}$  in the nanowire spectrum is comparable with bulk 3C-SiC. However, the appearance of a second TO phonon mode at  $810 \text{ cm}^{-1}$  in the nanowire spectrum indicates that there are regions in the nanowire under compressive strain. A relatively large increase in the SiC TO phonon wavenumber ( $\approx 5 \text{ cm}^{-1}$  to  $\approx 6 \text{ cm}^{-1}$ ) has been reported in 3C-SiC grown on TiC and attributed to compressive strain in the SiC layer<sup>120</sup>. A likely cause of the strain is the presence of planar defects in the nanowires, as identified by TEM. It is possible that either the low-strain region grows with a lower defect concentration than the high-strain region or that the defect concentration is high enough to lead to strain relaxation in the low-strain region.

Broader, weaker features observed in Fig. 54 at  $\approx 480 \text{ cm}^{-1}$  to  $\approx 640 \text{ cm}^{-1}$  and  $\approx 820 \text{ cm}^{-1}$  to  $\approx 980 \text{ cm}^{-1}$  are attributed to scattering by phonon modes originating from other than the Brillouin zone center<sup>121-123</sup>. In pure, perfect crystals, only zone center optical phonon modes should be allowed for the scattering conditions employed in this work. However, this restriction can be relaxed due to the presence of defects which

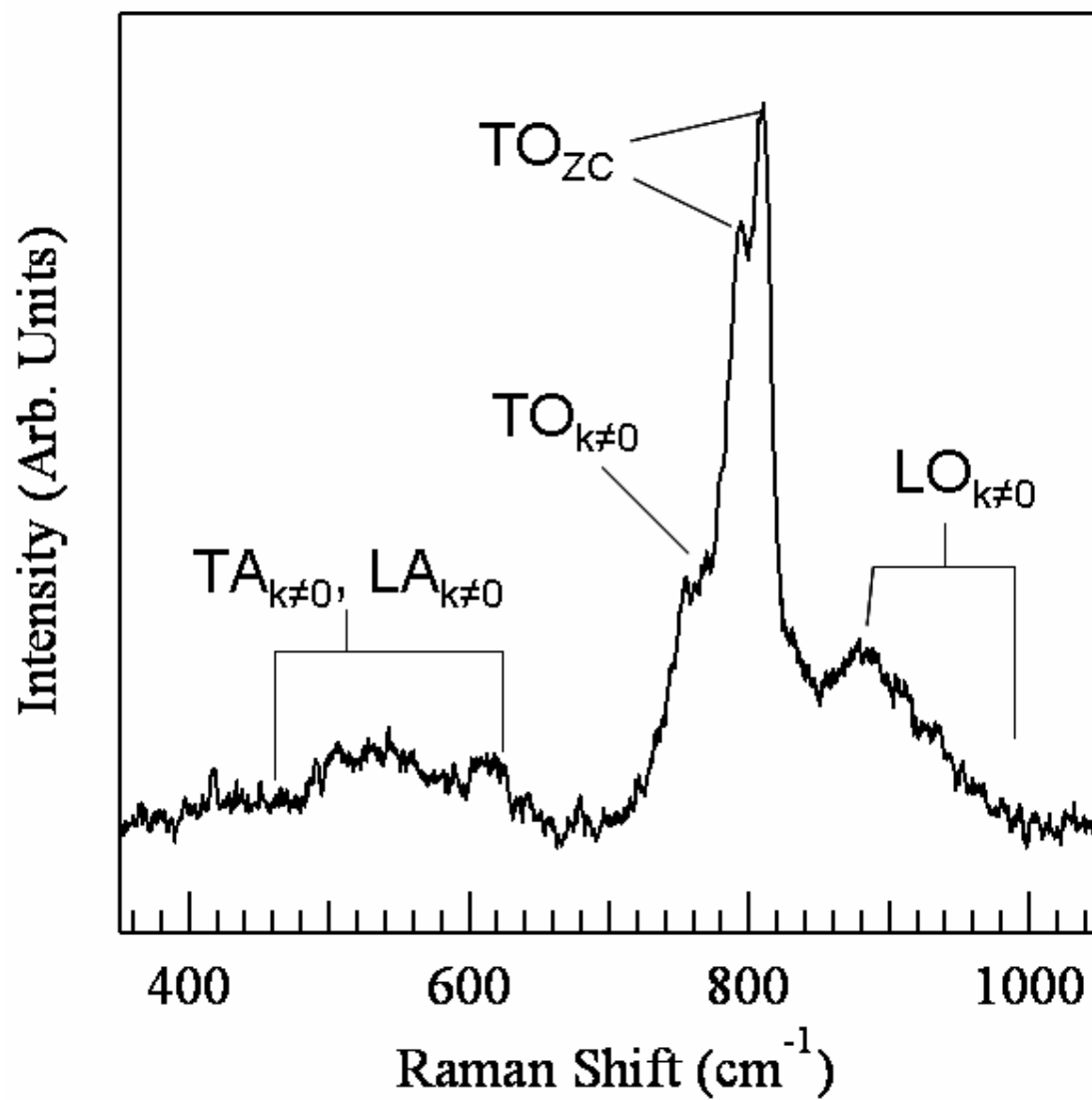


**Figure 54:**  $\mu$ -Raman spectrum from an isolated SiC nanowire.

destroy translational symmetry<sup>124</sup>. The resulting Raman spectrum exhibits features of the phonon density of states rather than only zone center phonon modes. Hence, the  $\approx 480\text{ cm}^{-1}$  to  $\approx 640\text{ cm}^{-1}$ ,  $\approx 820\text{ cm}^{-1}$  to  $\approx 980\text{ cm}^{-1}$ , and  $\approx 756\text{ cm}^{-1}$  features are attributed to defect-induced acoustic (transverse and longitudinal) phonon mode scattering, LO phonon mode scattering, and TO phonon mode scattering, respectively, from throughout the Brillouin zone<sup>125,126,118,119</sup>. Surface optical phonon modes may also contribute to the signal observed in  $\approx 900\text{ cm}^{-1}$  to  $\approx 980\text{ cm}^{-1}$  range<sup>122</sup>. No longitudinal optical (LO) phonon modes are observed in Fig. 54. This is consistent with previously reported SiC nanowire spectra obtained in this geometry<sup>120,121</sup>.

#### **4.9 Summary and suggested future work on SiC nanowires**

In summary, a novel technique for the controlled rapid growth of 1-D nanostructures of 3C-SiC using various group VIII transition metal catalysts has been developed. The experimental parameters that dictate the growth of faceted nanowires (with straight sidewalls), nanoneedles and nanocones (with tapering sidewalls) have been identified. The nanowires, which are the focus of this article are found to grow by the VLS mechanism at substrate temperatures in the range of  $1650\text{ }^{\circ}\text{C}$  –  $1750\text{ }^{\circ}\text{C}$ , for growth durations of  $15\text{ s}$  –  $40\text{ s}$ , along the  $\langle 112 \rangle$  crystallographic directions. TEM studies have indicated the presence of two types of nanowires, one type maintains a constant growth direction, and another type frequently changes its growth direction by twinning. Also, several stacking faults running along the length of the nanowires have been identified. Micro-Raman spectra of the SiC nanowires, in addition to confirming the 3C-polytype,

also indicate the presence of regions exhibiting different compressive strain in the nanowire as well as non Brillouin zone-center modes.

## 5. CONCLUSIONS AND FUTURE WORK

### 5.1 Conclusions

This Ph.D. dissertation work has demonstrated the use of a novel solid-state microwave annealing system for ultra-fast high-temperature processing of SiC and GaN.

The post-implantation microwave annealing parameters for SiC have been optimized for obtaining ultra-low sheet resistivities, high carrier mobilities, and low defect concentrations. Use of a protective photoresist-converted graphite cap and high temperature ramping rates ( $\geq 400$  °C/s) have resulted in elimination of SiC sublimation during microwave annealing, even at temperatures as high as 2100 °C. Smooth surfaces with comparable surface roughness to the as-implanted SiC have resulted after high-temperature microwave annealing treatments. Negligible redistribution of buried boron implanted SiC was observed, after 1700 °C microwave annealing treatments. Also, the lattice quality of microwave-annealed, implanted SiC is superior to that of virgin material due to removal of defects introduced during SiC growth.

For GaN, microwave annealing with a PLD AlN cap in place has resulted in negligible GaN decomposition even at temperatures as high as 1500 °C, for short-duration (5 s) microwave annealing. On the other hand, the GaN film totally decomposed (forming liquid Ga droplets), for 1400 °C microwave annealing, when an electron-beam deposited MgO cap was used in place of the PLD AlN cap. Compared to 1300 °C

annealing, the 1500 °C microwave annealing resulted in an increased hole concentration, due to both an increase in Mg acceptor activation, and a decrease in the compensating deep donor concentration.

As for the high-dose multiple energy, Mg –implanted GaN, we were unable to achieve any electrical activation in spite of annealing at temperatures as high as 1400 °C. A significant lattice damage was observed even after 1400 °C annealing, which precluded any electrical activation.

A novel catalyst-assisted sublimation-sandwich technique has been developed for the controlled growth of different SiC nanostructure morphologies. Process parameters for the controlled growth of specific nanostructure morphologies, i.e. nanocones, nanowires, and nanoneedles have been identified. In-depth structural and optical characterization has been performed on the nanowires.

## **5.2 Future work**

It has been demonstrated in this dissertation that microwave annealing of ion-implanted SiC can result in unprecedented ultra-low sheet resistances for both p-type and n-type implants. Also, the defect densities in the microwave annealed SiC are lower than even un-implanted SiC epilayers. The next step would be to validate these superior material characteristics at the device level by fabricating SiC n- and p-MOSFETS, p-i-n diodes (with ion-implanted anode layers), and bipolar junction transistors, using microwave processing, with the hope of improving the inversion layer mobilities in

MOSFETs, and increasing the breakdown voltage and decreasing the on-resistance of the p-i-n diodes.

In GaN technology, the low sheet resistances obtained for implanted p-type layers and the superior material quality could lead to drastic performance improvements in both MOSFET type electronic devices as well as laser diodes. The fabrication and characterization of these devices would be the logical next step. Future work involves ultra-high temperature annealing of Si (n-type) implanted GaN and especially AlGaN epilayers grown on SiC. If successful, such layers can be used under source/drain contacts of AlGaN- GaN HEMT devices, in an attempt to lower the source/drain access resistance, and to increase the device transconductance. Also, future high-temperature microwave anneals are planned on in-situ Mg doped  $\text{Al}_{0.25}\text{Ga}_{0.75}\text{N}$  and  $\text{Al}_{0.4}\text{Ga}_{0.6}\text{N}$  grown on sapphire. Increasing the Al content in the AlGaN ternary increases the bandgap and finds application in smaller wavelength laser diodes. However, the increasing Al content in AlGaN also makes p-type doping more difficult to achieve.

Future work on SiC nanowires involves:

1. Investigation of the methods and process conditions which yield controllable growth of SiC nanowires along different crystallographic axes.
2. Exploring techniques for defining diameter and patterning of the SiC nanowires on the substrate wafer.
3. Exploring methods for in-situ and/or ex-situ doping of the SiC nanowires.

4. Fabrication of SiC nanowire MOSFETs and device characterization to extract transport parameters such as field-effect mobilities.

## 6. APPENDIX

### A.1 Photoluminescence spectroscopy

#### Instrumentation and principle of operation

A typical PL setup is shown in Fig. A.1. The sample is excited with an optical source, typically a laser<sup>1</sup> with energy  $h\nu > E_G$ , generating electron hole pairs (ehps) which recombine by one of several mechanisms. Photons are emitted for radiative recombinations, which is detected as a PL signal. The optics in a PL apparatus are designed to ensure maximum light collection. The PL-emitted light from the sample can be analyzed by a grating monochromator and detected by a photodetector. One can also vary the wavelength of the incident light using a tunable dye laser. Low temperature measurements are desirable to obtain the fullest spectroscopic information by minimizing the thermally activated non-radiative recombination processes and thermal line broadening. The thermal distribution of carriers excited into a band contributes a width of  $\approx kT/2$  to an emission line originating from that band. This makes it necessary to cool the sample down to increase the resolution of the PL spectra. The thermal energy,  $kT/2$  is only 1.8 meV at  $T = 4.2$  K (liquid He temperature).

---

<sup>1</sup> For the PL characterization performed in this dissertation on GaN, the 325 nm line of a He-Cd laser was used for above-bandgap excitation.

The emitted PL intensity depends on the particular recombination process. There are five common PL transitions in semiconductors. (a) Band-to-band recombination is commonly observed at room temperature but is rarely observed at low temperatures in materials with small effective masses. (b) Free-exciton (FE) recombination. (c) Free hole

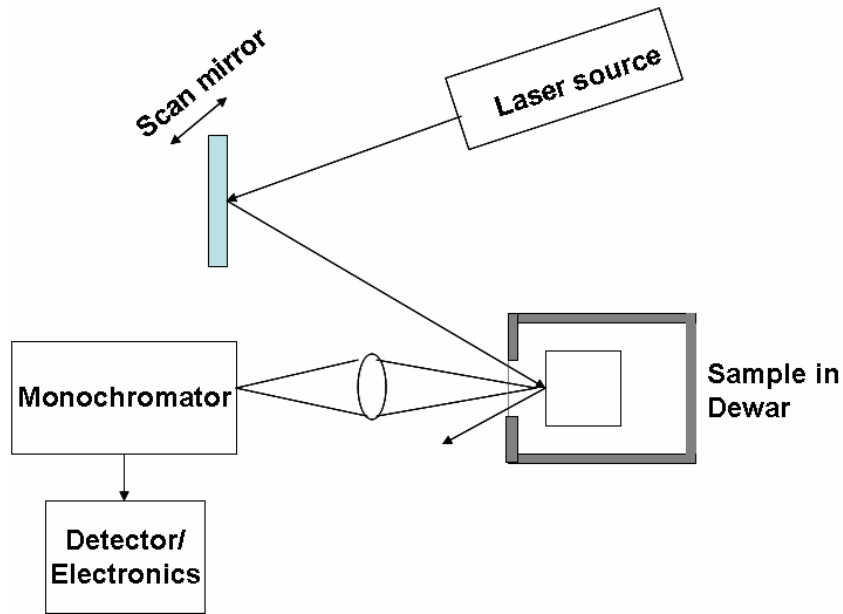


**Figure A.1:** Typical experimental setup employed for PL measurements [Source: D.K.

Schroder, *Semiconductor and Device Characterization*, IEEE Press, 2006]

combining with a neutral donor to form a positively charged excitonic ion ( $D^0X$ ). (d) Free electron recombining with a neutral acceptor to form a negatively charged excitonic ion called exciton bound to neutral acceptor ( $A^0X$ ). (e) Donor-acceptor pair (DAP) recombination: Electron on a neutral donor recombining with a hole on a neutral

acceptor. The emission line in a DAP transition has an energy augmented by the Coulombic attraction<sup>127</sup> between the donor and the acceptor:

$$h\nu = E_G - (E_D - E_A) + \frac{q^2}{K_S \epsilon_0 r} \quad (6)$$

where  $r$  is the distance between the donor and the acceptor. The FWHMs for bound exciton recombinations are typically  $\leq kT/2$ , which distinguishes them from donor-valence band transitions which are typically a few  $kT$  wide.

### **Strengths of PL**

- PL is generally not sensitive to the pressure in the sample chamber. Hence, it can be used to study surface properties in relatively high-pressure semiconductor growth reactors.
- PL has little effect on the surface under investigation (non destructive). Photoinduced changes and sample heating are possible, but low excitation can minimize these effects.
- In situ PL measurements do require optical access to the sample chamber.
- Compared with other optical methods of characterization like reflection and absorption, PL is less stringent about beam alignment, surface flatness, and sample thickness.

## **Weaknesses of PL**

- The sample under investigation must emit light. Indirect-bandgap semiconductors, where the conduction band minimum is separated from the valence band maximum in momentum space, have inherently low PL efficiency.
- Difficulty in estimating the density of interface and impurity states.

## **A.2 Secondary ion mass spectrometry**

Secondary ion mass spectrometry (SIMS) is the most sensitive surface analysis technique. It is capable of detecting all elements (H – U) with detection limits in the  $10^{14}$   $\text{cm}^{-3}$  to  $10^{15}$   $\text{cm}^{-3}$  range. Lateral resolution is typically 100  $\mu\text{m}$ , but can be as small as 0.5  $\mu\text{m}$  with depth resolution of 5 to 10 nm.

### **Instrumentation and principle of operation**

The basis of SIMS is the destructive removal of material from the sample by sputtering and the analysis of the ejected material by a mass analyzer. A schematic of a typical SIMS setup is shown in Fig. A.2. Primary ions are passed to the sample through the primary ion column. The column usually contains a primary beam mass filter that transmits only ions with a specified mass-to-charge ( $m/z$ ) ratio. This mass filter eliminates impurity species in the beam. When the primary ion impinges on the sample surface, it is implanted into the sample, and ejects material out from the sample. The ejected material consists of (neutral) atoms as well as charged ions. The charged ions typically constitute  $\approx 1\%$  of the mass ejected out of the sample. It is these secondary ions

which are detected by the mass spectrometer and constitute the scattering yield in a SIMS experiment. The scattering yields can however be enhanced by using (electropositive)  $\text{Cs}^+$  primary ions for elements which form negative ions such as oxygen, phosphorus, etc., and (electronegative)  $\text{O}^+$  primary ions for elements which form positive ions such as aluminum, boron, magnesium, etc. The secondary ions are then analyzed for their mass to charge ( $m/e$ ) ratio by either an electrostatic-magnetic sector analyzer or a quadrupole mass analyzer. The advantage of using an electrostatic-magnetic sector analyzer is the ability to distinguish between masses, which are as close as 0.003%.

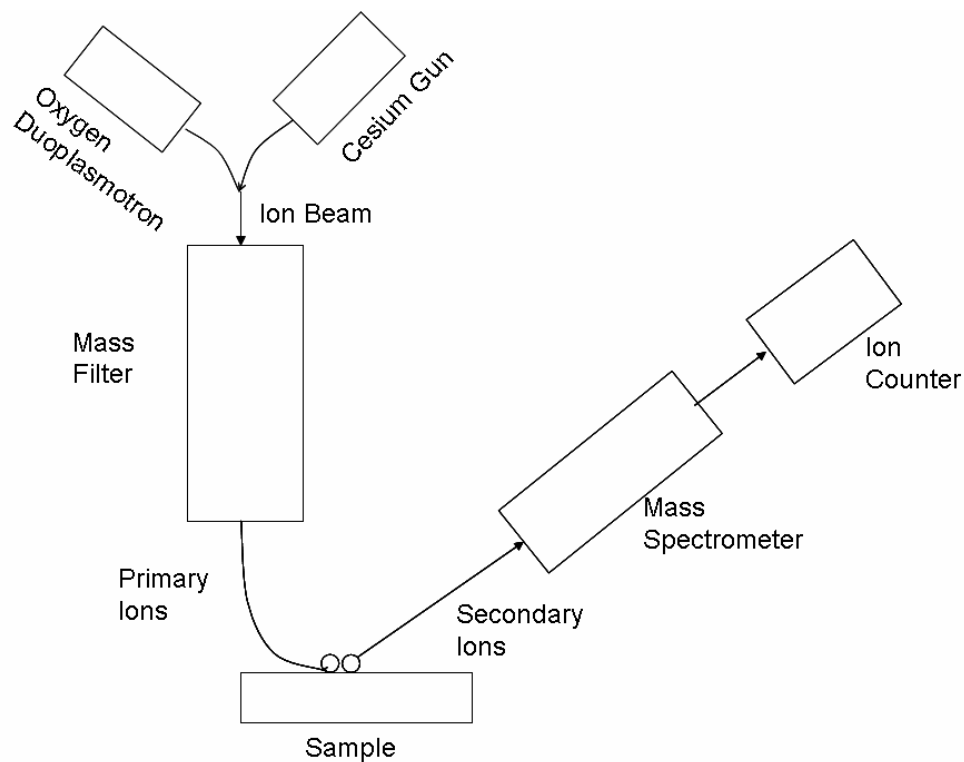


**Figure A.2:** A schematic of a typical SIMS setup [Source: D.K. Schroder, *Semiconductor Material and Device Characterization*, IEEE Press, 2006]

example,  $^{31}\text{P}$  (31.9738 amu) has a very similar m/e ratio as  $^{30}\text{Si} \ ^1\text{H}$  (31,9816 amu) . A quadropole mass analyzer on the other hand is less expensive and has lower extraction potentials due to which it is suitable for analyzing insulating samples. Also, quadropole SIMS can rapidly switch between different mass peaks, increasing the depth resolution. However, it is less sensitive to the m/e ratio.

### **Strengths of SIMS**

- Excellent detection sensitivity for dopants and impurities, with ppm or lower detection sensitivity
- Depth profiles with excellent detection limits and depth resolution
- Small-area analysis (10  $\mu\text{m}$  or larger)
- Detection of all elements and isotopes, including H
- Excellent dynamic range (up to 6 orders of magnitude)

### **Weaknesses of SIMS**

- SIMS is a destructive technique
- Does not provide chemical bonding information
- Sample must be solid and vacuum compatible

### **A.3 Rutherford backscattering spectrometry**

Rutherford backscattering spectrometry (RBS) is based on bombarding a sample with energetic ions – typically He ions of 1 – 3 MeV energy – and measuring the energy of backscattered He ions. It allows the determination of the masses of the elements in the sample, their depth distribution over distances from 10 nm to a few microns from the surface, their areal density, and the crystalline structure in a non-destructive manner. The depth resolution is on the order of 10 nm.

#### **Instrumentation and principle of operation**

An RBS system consists of an evacuated chamber containing the He ion generator, the accelerator, the sample and the detector. Negative He ions are generated in the ion accelerator at close to the ground potential, following which they are accelerated to 1 MeV, traversing a stripper canal where either 2 or 3 electrons are stripped from the He<sup>-</sup> to form He<sup>+</sup> or He<sup>2+</sup>, respectively. These ions are further accelerated to ground potential at which point the He<sup>+</sup> ions have 2 MeV and the He<sup>2+</sup> ions have 3 MeV energy. A magnet separates the two ion species. In the sample chamber, the He ions are incident on the sample, and the backscattered ions are detected by a Si surface barrier detector. The spectrum is displayed as yield or counts versus channel number with channel number proportional to energy. The energy resolution of Si detectors is 10 – 20 keV.

If  $E_0$ ,  $v_0$ , and  $M_1$  are the energy, velocity, and mass of an incident ion,  $E_1$ ,  $v_1$ ,  $M_2$  correspond to the backscattered ion, and  $v_2$  and  $M_2$  correspond to the velocity and mass of the target atom after the scattering event, equations for the conservation of energy and

momentum can be written down. Combining these equations, a so-called kinematic factor,  $K$  is defined as<sup>127</sup>:

$$K = \frac{E_1}{E_0} = \frac{\left[ \sqrt{1 - (R \sin \theta)^2} + R \cos \theta \right]^2}{(1 + R)^2} \approx 1 - \frac{2R(1 - \cos \theta)}{(1 + R)^2} \quad (7)$$

where  $R = M_1/M_2$  and  $\theta$  is the scattering angle. The unknown mass  $M_2$  is calculated from the measured energy  $E_1$  through the kinematic factor. The approximation in eqn. 7 holds only as long as  $M_1 \ll M_2$ , and  $\theta$  is close to  $180^\circ$ . This is why He is chosen as the primary ion species, and scattering angles of  $170^\circ$  are commonly employed in practice.

In this dissertation, RBS was used to evaluate the crystallinity of ion-implanted semiconductor samples before and after high-temperature annealing treatments. Backscattering is strongly affected by the alignment of atoms in a single crystal sample with the He incident He ion beam. If the atoms are well aligned with the beam, the scattering yield is substantially (2 orders of magnitude) lower than a randomly aligned sample.

### **Strengths of RBS:**

- Quantitative without standards
- Whole wafer analysis (150, 200, 300 mm) as well as irregular and large samples
- Channeling analysis to quantify crystallinity

## **Weaknesses of RBS**

- Large analysis area (~2 mm)
- Useful information limited to top ~1  $\mu\text{m}$  of the sample
- Destructive technique
- Sensitivity is lower than SIMS ( $> 10^{17} \text{ cm}^{-3}$ )
- not suitable for elements lighter than substrate

## **A.4 Raman Spectroscopy**

This technique relies on inelastic scattering, or Raman scattering of monochromatic light, usually from a laser in the visible, near infrared, or near ultraviolet range. The laser light interacts with optical phonons in the system, resulting in the energy of the laser photons being shifted up (Stokes shift) or down (anti-Stokes shift). The shift in energy gives information about the phonon modes in the system.

### **Instrumentation and Principle of Operation**

A schematic of a micro-Raman setup is shown in Fig. A.4. The radiation from a CW laser is focused onto a sample of interest through a microscope objective, so that the incident radiation can be confined to a very small spot (~ 1-5  $\mu\text{m}$ ) on the sample. Incident laser radiation is usually delivered to the microprobe using a single mode optical fiber, resulting in depolarized radiation exiting the fiber. Radiation is introduced into the microscope optical path using an angled dielectric edge filter in the so-called injection-rejection configuration. Collected scattered radiation is delivered to a 0.5 m focal length

imaging single spectrograph using a multimode optical fiber. Then, the Raman shifted radiation is incident on a spectrograph and the Raman spectrum is fed to a CCD operating typically at  $-90\text{ }^{\circ}\text{C}$ , to reduce the instrumental bandpass. Typically, laser intensity is kept  $< 5\text{ mW}$  to prevent heating of the sample.

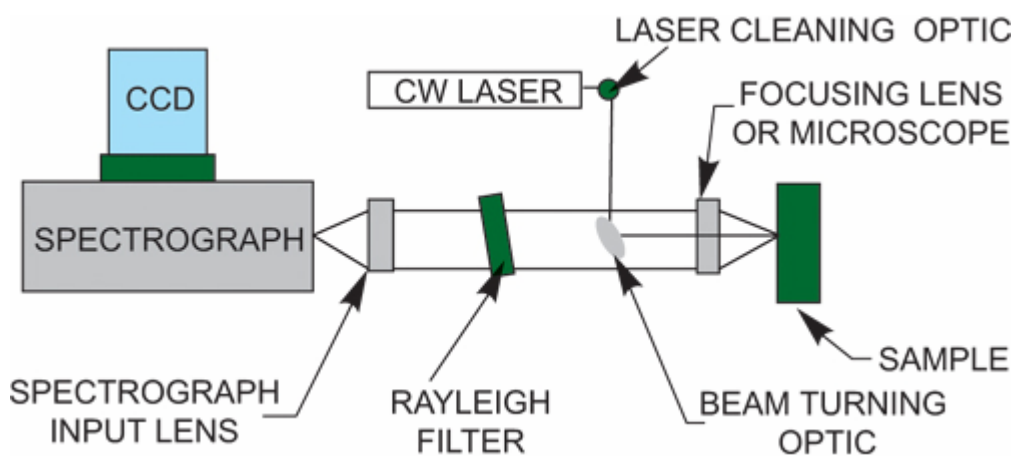


**Figure A.4:** A schematic of the experimental setup for performing micro-Raman spectroscopy [Source: <http://elchem.kaist.ac.kr/vt/chem-ed/spec/vib/raman.htm>]

### Strengths of Raman spectroscopy

- Capable of identifying organic functional groups and often specific organic compounds
- Capable of a detailed strain analysis of semiconductor samples.

- Ambient conditions (not vacuum; good for semi-volatile compounds)
- Typically non-destructive
- Minimum analysis area:  $\sim 1 \mu\text{m}$

### **Weaknesses of Raman Spectroscopy**

- Limited surface sensitivity (typical sampling volumes are  $\sim 0.8 \mu\text{m}$ )
- Limited inorganic information
- Typically not quantitative (needs standards)
- Fluorescence (much more intense than the Raman signal) can limit Raman usefulness

### **A.5 Auger Electron Spectroscopy**

Auger Electron Spectroscopy (AES) is a surface-specific analytical technique that utilizes a high-energy electron beam as an excitation source. Atoms that are excited by the electron beam can relax under the emission of "Auger" electrons. AES measures the kinetic energies of the emitted Auger electrons, which are characteristic of elements present at the surface and "near-surface" of a sample.

### **Instrumentation and Principle of Operation**

Assume a material with a K level at energy level  $E_K$  and two L levels ( $E_{L1}$  and  $E_{L2}$ ). A primary electron with typically 3 -5 keV energy from an electron gun ejects an electron from the K shell. The K-shell vacancy is filled in this case by an electron from the  $L_1$  shell, and this energy ( $E_K - E_{L1}$ ) is transferred to a third Auger electron which originates in this case from the  $L_{2,3}$  level. The atom remains in a doubly ionized state, and the entire process is labeled KLL. In the KLL transition, the L level ends up with two vacancies, which can lead to an LVV transition. The Auger electron energy, characteristic of the emitting atom of atomic number  $Z$ , for the KLL transition is

$$E_{KLL} = E_K(Z) - E_{L_1}(Z) - E_{L_{2,3}}(Z+1) - q\phi \quad (8)$$

AES instrumentation (Fig. A.5) consists of an electron gun, electron beam control, an electron energy analyzer, and data analysis electronics. The incident electron beam energy is typically 1 to 5 keV. The emitted Auger electrons are detected with a cylindrical mirror analyzer (CMA). Auger electrons, entering the inlet aperture between two concentric cylinders, are focused by a negative potential creating a cylindrical electric field between the coaxial electrodes. The CMA allows electrons with  $E \approx V_a$  and energy spread  $\Delta E$  to pass through the exit slit. Ramping the analyzing potential  $V_a$  provides the electron energy spectrum. The energy resolution is defined by

$$R = \frac{\Delta E}{E} \quad (9)$$

where  $\Delta E$  is the pass energy of the analyzer and  $E$  is the electron energy.

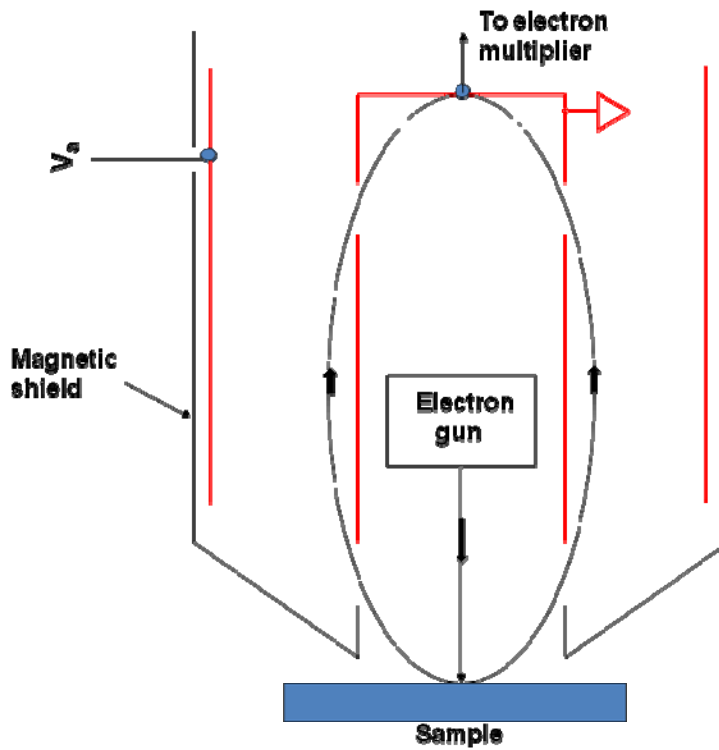


**Figure A.5** A typical AES experimental setup with a cylindrical mirror analyzer [Source: D.K. Schroder, *Semiconductor Material and Device Characterization*, IEEE Press, 2006]

### Strengths of AES

- Surface elemental analysis, depth profiling possible by ion beam sputtering
- Small area analysis (as small as 30 nanometers)
- Excellent surface sensitivity (top 1-5 nm)
- Good depth resolution

### Weaknesses of AES

- Standards required for best quantification
- Samples must be vacuum compatible
- Relatively poor detection sensitivity (0.1 at% at best)

### **A.6 X-ray photoelectron spectroscopy**

X-ray photoelectron spectroscopy (XPS) also known as electron spectroscopy for chemical analysis (ESCA) is the high-energy version of the photoelectric effect discovered by Hertz in 1887. It is primarily used for identifying chemical species at the sample surface, allowing all elements except hydrogen and helium to be detected.

#### **Instrumentation and principle of operation**

In XPS, the photons that interact with the core-level electrons are X-rays. Electrons can be emitted from any orbital with photoemission occurring for X-ray energies exceeding the binding energy. Primary X-rays of 1 – 2 keV eject photoelectrons from the sample. The measured (kinetic) energy of the ejected electron at the spectrometer  $E_{KE}$  is related to the binding energy (referenced to the Fermi energy  $E_F$ ), by<sup>127</sup>

$$E_{KE} = h\nu - E_B - q\phi_{sp} \quad (10)$$

where  $h\nu$  is the energy of the primary X-rays and  $\Phi_{sp}$  is the work function of the spectrometer (3 to 4 eV). With  $E_{KE}$  depending on the X-ray energy, it is important that the X-rays be monochromatic. The spectrometer and the sample are connected forcing their Fermi levels to line up. The electron binding energy is influenced by its surroundings, making XPS capable of determining chemical states, in addition to elemental information. X-ray induced Auger electron emission may also occur during XPS, which can be used to advantage. For example; varying the incident X-ray energy changes the energy of the XPS electrons but does not affect the energy of the Auger electrons. XPS is surface sensitive because the emitted photoelectrons originate from the top 0.5 – 5 nm of the sample, just as the Auger electrons do, despite the deeper penetration depth of the X-rays compared to electrons.

The three basic components of XPS are an X-ray source, the spectrometer, and a high-vacuum chamber. X-ray line widths are proportional to the atomic number of the target in the X-ray tube. The X-ray line width in XPS should be as narrow as possible; hence light elements like Al ( $E_{K\alpha} = 1.4866$  keV) and Mg ( $E_{K\alpha} = 1.2566$  keV) are common X-ray sources. The XPS electrons can be detected by a similar analyzer (cylindrical mirror analyzer) as in AES. The XPS sensitivity is about 0.1% or  $5 \times 10^{19} \text{ cm}^{-3}$  and depth resolution is around 10 nm.

### **Strengths of XPS**

- Chemical state identification on surfaces
- Identification of all elements except for H and He

- Quantitative analysis, including chemical state differences between samples

### **Weaknesses of XPS**

- Detection limits typically ~ 0.1 at%
- Smallest analytical area ~10  $\mu\text{m}$
- Limited specific organic information
- Sample compatibility with UHV environment

### **A.7 Electron backscatter diffraction**

Electron Backscatter Diffraction (EBSD) is a technique which allows crystallographic information to be obtained from samples in the scanning electron microscope (SEM). In EBSD a stationary electron beam strikes a tilted crystalline sample and the diffracted electrons form a pattern on a fluorescent screen. This pattern is characteristic of the crystal structure and orientation of the sample region from which it was generated. The diffraction pattern can be used to measure the crystal orientation, measure grain boundary misorientations, discriminate between different materials, and provide information about local crystalline perfection.

### **Instrumentation and principle of operation**

The mechanism by which the electron backscatter diffraction patterns are formed is complex, but the following model describes the principal features. The atoms in the

material inelastically scatter a fraction of the electrons with a small loss of energy to form a divergent source of electrons close to the surface of the sample. Some of these electrons are incident on atomic planes at angles which satisfy the Bragg equation:

$$n\lambda = 2d \sin \theta \quad (11)$$

where  $n$  is an integer,  $\lambda$  is the wavelength of the electrons,  $d$  is the spacing of the diffracting plane, and  $\theta$  is the angle of incidence of the electrons on the diffracting plane. These electrons are diffracted to form a set of paired large angle cones corresponding to each diffracting plane. When used to form an image on the fluorescent screen the regions of enhanced electron intensity between the cones produce the characteristic Kikuchi bands of the electron backscatter diffraction pattern (see Figure A.7.1). The center lines of the Kikuchi bands correspond to the (gnomonic) projection of the diffracting planes on the phosphor screen. Hence, each Kikuchi band can be indexed by the Miller indices of the diffracting crystal plane which formed it. Each point on the phosphor screen corresponds to the intersection of a crystal direction with the screen. In particular, the intersections of the Kikuchi bands correspond to the intersection of zone axes in the crystal with the phosphor screen.

The principal components of an EBSD system are (Figure A.7.3):

- A sample tilted at  $70^\circ$  from the horizontal.
- A phosphor screen which is fluoresced by electrons from the sample to form the diffraction pattern.

- A sensitive charge coupled device (CCD) video camera for viewing the diffraction pattern on the phosphor screen.
- A vacuum interface for mounting the phosphor and camera in an SEM port. The camera monitors the phosphor through a lead glass screen in the interface and the phosphor can be retracted to the edge of the SEM chamber when not in use.
- Electronic hardware that controls the SEM, including the beam position, stage, focus, and magnification.
- A computer to control EBSD experiments, analyze the diffraction pattern and process and display the results.
- An optional electron detector mounted below the phosphor screen for electrons scattered in the forward direction from the sample.

### **Strengths of EBSD**

- Surface crystal structure determination with a spatial and depth resolution as fine as 100 nm.
- When the beam is scanned in a grid across a polycrystalline sample and the crystal orientation measured at each point, the resulting map will reveal the constituent grain morphology, orientations, texture, and boundaries.
- Ideal for studying crystal structure (polytype, growth direction) of nanowires and nanotubes, due to its ultra-high spatial and depth resolution.
- Measurement of localized strain in materials.

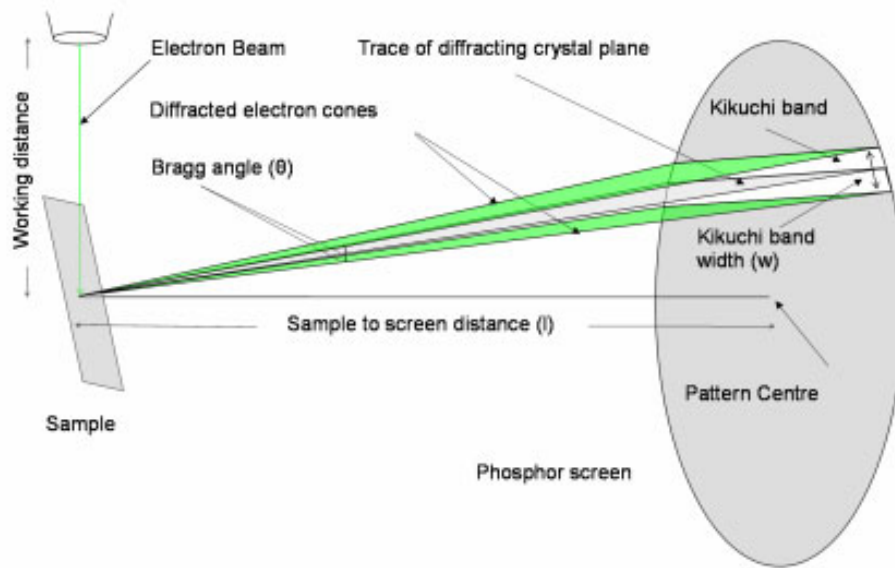


**Figure A.7.1:** Schematic illustrating how features in the diffraction pattern are related to the crystal structure [Source: [www.EBSD.com](http://www.EBSD.com)]

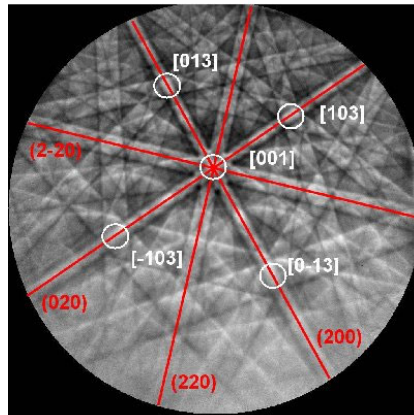


**Figure A.7.2:** An indexed diffraction pattern from nickel collected at 20 kV accelerating voltage. The (2-20), (020), (220), (200) planes meet each other at the [001] zone axis. The symmetry of the crystal is shown in the diffraction pattern. For example, four fold symmetry is shown around the [001] direction by four symmetrically equivalent  $\langle 013 \rangle$  zone axes. [Source: [www.ebsd.com](http://www.ebsd.com)]

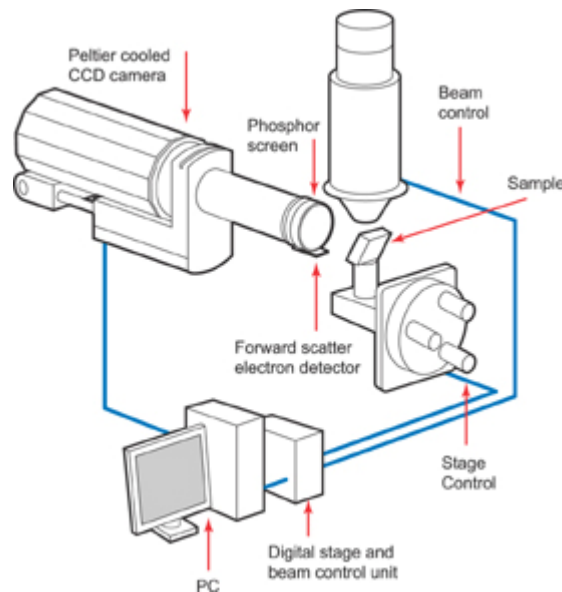


**Figure A.7.3:** The experimental set up employed for EBSD measurements [Source: [www.ebsd.com](http://www.ebsd.com)]

### **Weaknesses of EBSD**

- Unsuitable for biological or polymeric materials due to high energy electron beam.
- Inability to ascertain lattice parameters.
- Interaction of electron beam with SEM magnetic field causes warpage of diffraction patterns.
- Resolution is smaller for lower atomic number materials.

### **A.8 X-ray diffraction**

X-ray diffraction is one of the most commonly used characterization techniques to study the crystal structure of materials. The wavelength of X-rays is comparable with interatomic spacing in materials; therefore, a wealth of information can be gained by studying the interaction of X-rays with materials. X-ray (electron, neutron, etc.) diffraction is based on Bragg's law (eqn. 11) which relates the interatomic spacing,  $d$ , with the x-ray wavelength,  $\lambda$  and incident angle,  $\theta$ .

X-ray diffraction is depicted schematically in Fig. A.8. There are several ways in which x-ray diffraction can be performed such as  $\theta$ - $2\theta$  scans, rocking curve scans, pole figure scans, etc. Details of these specific techniques can be found in several textbooks. A peak of diffracted X-ray intensity is obtained, when the Bragg condition is met.

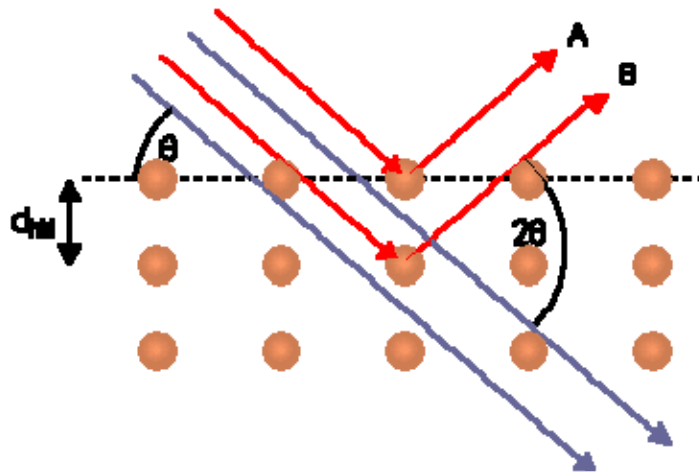


**Figure A.8:** A schematic of X-ray diffraction by atomic planes of a crystal. A particular atomic plane diffracts x-rays, when the angle,  $\theta$  made by the incoming x-ray beam with that particular atomic plane satisfies the Bragg condition.  $d_{hkl}$  is the interatomic spacing for the diffracting atomic plane in this example .

### Strengths of X-ray diffraction

- Thorough and accurate crystal structure analysis including lattice parameter determination, stress measurements, texture analysis, and other mechanical parameters of the material.
- One of the oldest crystal structure analysis techniques with an exhaustive database of crystallographic data for almost any known material.

### Weaknesses of X-ray diffraction

- Spatial resolution is limited, typically 0.5 – 1mm.

## List of References

- <sup>1</sup> C-M. Zetterling (ed.), *Process Technology for Silicon Carbide Devices*, INSPEC, IEEE Press, London, U.K. (2002).
- <sup>2</sup> S.E. Saddow, A.K. Agarwal (eds.), *Advances in Silicon Carbide Processing and Applications*, Artech House, Norwood, MA (2004).
- <sup>3</sup> S.J. Pearton, C.R. Abernathy, F. Ren, *Gallium Nitride Processing for Electronics, Sensors, and Spintronics*, Springer-Verlag, London (2006).
- <sup>4</sup> <http://www.nitronex.com/education/ganHEMT.pdf>.
- <sup>5</sup> Z. C. Feng (ed.), *III-Nitride Semiconductor Materials*, Imperial College Press. London (2006).
- <sup>6</sup> S.C Singhal, *J. Mater. Sci.* **11**(7), 1246-53 (1976).
- <sup>7</sup> G. Pensl, V. Afanasev, M. Bassler, M. Schadt, T. Troffer, J. Heindl, H. Strunk, M. Maier, and W. Choyke, *Inst. Phys. Conf. Ser.* **142**, 275–80 (1996).
- <sup>8</sup> S. Sheshadri, G.W. Elkridge, A.K. Agarwal, *Appl. Phys. Lett.* **72**, 2026 (1998).
- <sup>9</sup> C. Ronning et al. *Phys. Reports* **351**, 349 (2001).
- <sup>10</sup> Y. Huang, C.M. Lieber, *Pure Appl. Chem.* **76**, 2051 (2004).
- <sup>11</sup> M. Law, J. Goldberger, P. Yang, *Annu. Rev. Mater. Res.* **34**, 83 (2004).
- <sup>12</sup> W.Z. Li, S.S. Xie, L.X. Qian, B.H. Chang, B.S. Zou, W.Y. Zhou, R.A. Zhou, G. Wang, *Science* **274**, 1701 (1996).
- <sup>13</sup> W.Q. Han, S.S. Fan, Q.Q. Li, Y.D. Hu, *Science*, **277**, 1287 (1996).

- <sup>14</sup> A.M. Morales, C.M. Lieber, *Science*, **279**, 208 (1998).
- <sup>15</sup> J.Y. Fan, X.L. Wu, P.K. Chu, *Prog. Mater. Sci.* **2**, 1 (2006).
- <sup>16</sup> Z.S. Wu, S.Z. Deng, J. Chen, J. Zhou, *Appl. Phys. Lett.* **80**, 3829 (2002).
- <sup>17</sup> H.F. Zhang, C.M. Wang, S.L. Wang, *Nano Lett.* **2**, 941 (2002).
- <sup>18</sup> X. Wu, W. Song, W. Huang, M. Pu, B. Zhao, Y. Sun, J. Du, *Mater. Res. Bul.* **36**, 847 (2001).
- <sup>19</sup> R. Pampuch, G. Gorny, L. Stobierski, *Glass Phys. Chem.* **31**, 370 (2005).
- <sup>20</sup> W. Shi, Y. Zheng, H. Peng, N. Wang, C.S. Lee, S.T. Lee, *J. Am. Ceram. Soc.* **83**, 3228 (2000).
- <sup>21</sup> D.P. Yu, C.S. Lee, I. Bello, X.S. Sun, Y.H. Tang, G.W. Zhou, Z.G. Bai, Z. Zhang, S.Q. Feng, *Chem. Phys. Lett.* **345**, 29 (2001).
- <sup>22</sup> F. Yan, Z. Xu, M.B. Zhao, *Scr. Mater.* **53**, 361 (2005).
- <sup>23</sup> A.J. Winn, R.I. Todd, *Br. Ceram. Trans.* **98**, 219 (1999).
- <sup>24</sup> S.M. Dong, G. Chollon, C. Labrugere, *J. Mater. Sci.* **36**, 2371 (2001).
- <sup>25</sup> P.G. Neudeck, *J. Electron. Mater.* **24**, 283 (1995).
- <sup>26</sup> Y.W. Ryu, K.J. Yong, *J. Vac. Sci. Technol. B*, **23**, 2069 (2005).

- <sup>27</sup> Y. Baek, Y. Ryu, K. Yong, *Mater. Sci. Engg. C*, **26**, 805 (2006).
- <sup>28</sup> S.Z. Deng, Z.S. Wu, J. Zhou, N.S. Xu, J. Chen, J. Chen, *Chem. Phys. Lett.* **356** (2002).
- <sup>29</sup> W.M. Zhou, B. Yang, Z.X. Yang, F. Zhu, L.J. Yan, Y.F. Zhang, *App. Surf. Sci.* **252**, 5143 (2006).
- <sup>30</sup> F. Li, G. Wen, L. Song, *J. Crys. Growth*, **290**, 466 (2006).
- <sup>31</sup> H-J. Choi, H-K. Seong, J-C. Lee, Y-M. Sung, *J. Crys. Growth*, **269**, 472 (2004).
- <sup>32</sup> V. A. Izhevskiy<sup>1</sup>, L. A. Genova, J. C. Bressiani, A. H. A. Bressiani, *Ceramica*, **46**, 297 (2000).
- <sup>33</sup> M.V. Rao, *Solid State Electronics* **47**, 213 (2003).
- <sup>34</sup> E.M. Handy, M.V. Rao, O.W. Holland, P.H. Chi, K.A. Jones, M.A. Derenge, R.D. Vispute, and T. Venkatesan, *J. Electron. Mater.* **29**, 1340 (2000).
- <sup>35</sup> M.V. Rao, J.A. Gardner, P.H. Chi, O.W. Holland, G. Kelner, J. Kretchmer and M. Ghezzi, *J. Appl. Phys.* **81**, 6635 (1997).
- <sup>36</sup> D. Dwight, M. V. Rao, O. W. Holland, G. Kelner, P. H. Chi, J. Kretchmer, and M. Ghezzi, *J. Appl. Phys.* **82**, 5327 (1997).
- <sup>37</sup> M.A. Capano, R. Santhakumar, R. Venugopal, M.R. Melloch, and J.A. Cooper, Jr. *J. Electron. Mater.* **29**, 210 (2000).
- <sup>38</sup> Y. Negoro, N. Miyamoto, T. Kimoto, and H. Matsunami, *Appl. Phys. Lett.* **80**, 240 (2002).

- <sup>39</sup> F. Schmid, M. Laube, and G. Pensl, *J. Appl. Phys.* **91**, 9182 (2002).
- <sup>40</sup> M.A. Capano, S. Ryu, J.A. Cooper, Jr, M.R. Melloch, K. Rottner, Karlsson, N. Nordell, A. Powell, D.E. Walker, Jr. *J. Electron. Mater.* **28**, 214 (1999).
- <sup>41</sup> M.A. Capano, S. Ryu, , M.R. Melloch, J.A. Cooper, Jr, M.R. Buss, *J. Electron. Mater.* **27**, 370 (1998).
- <sup>42</sup> J. Senzaki, K. Fukuda, K. Arai, *J. Appl. Phys.* **94**, 2942 (2003).
- <sup>43</sup> M. Rambach, et al., *Nucl. Instr. Met. Phys. Res. B*, **237**, 8 (2005).
- <sup>44</sup> K.A. Jones et al. *J. Appl. Phys.* **10**, 5613 (2004).
- <sup>45</sup> J.R. Jenny et al. *J. Appl. Phys.* **100**, 113710 (2006).
- <sup>46</sup> J.A. Gardner, M.V. Rao, Y-L. Tian, I. Ahmad, O.W. Holland, E.G. Roth, *J. Electron. Mater.* **26**, 144 (1997).
- <sup>47</sup> D. Panknin, H. Wirth, W. Anwand, G. Brauer, W. Skorupa, *Mater. Sci. Forum*, **338-342**, 877 (2000).
- <sup>48</sup> Y. Tanaka, H. Tanoue, K. Arai, *J. Appl. Phys.* **93**, 5934 (2003).
- <sup>49</sup> S.D. Ruksell, A.D. Ramirez, *Appl. Phys. Lett.* **74**, 3368 (2002).
- <sup>50</sup> Y. Hishida, M. Watanabe, K. Nakashima, O. Eryu, *Mater. Sci. Forum*, **338-342**, 873 (2000).
- <sup>51</sup> S.G. Sundaresan, Y-L. Tian, M.V. Rao, J.A. Schreifels, K.A. Jones, M.C. Wood, A.V. Davydov, *J. Electron. Mater.* **36**(4), 324 (2007).
- <sup>52</sup> S.C Singhal, *J. Mater. Sci.* **11**, 1246 (1976).

- <sup>53</sup> C. Raynaud, *J. Non-Cryst. Sol.* **280** 1-31 (2001).
- <sup>54</sup> T. Narushima, T. Goto, T Hirai, *J. Am. Cer. Soc.* **72**(8), 1386 (1989).
- <sup>55</sup> T. Troffer, C. Peppermuller, G. Pensl and A. Schoner, *J. App. Phys.* **80**, 3739 (1996).
- <sup>56</sup> G. Pensl, V. Afanasev, M. Bassler, M. Schadt, T. Troffer, J. Heindl, H. Strunk, M. Maier, and W. Choyke, *Inst. Phys. Conf. Ser.* **142**, 275 (1996).
- <sup>57</sup> M.V. Rao, J.B. Tucker, M.C. Ridgway, O.W. Holland, N. Papanicolaou, J. Mittereder, *J. App. Phys.* **86**, 752 (1999).
- <sup>58</sup> K.V. Vassilevski, A.B. Horsfall, C.M. Johnson, N.G. Wright, *Mater. Sci. Forum*, **457-460**, 989 (2004).
- <sup>59</sup> Y. Negoro, T. Kimoto, H. Matsunami, F. Schmid, G. Pensl, *J. App. Phys.* **96**(9), 4916-22 (2004).
- <sup>60</sup> W.C. Mitchel, A.O. Evwaraye, S.R. Smith, M.D. Roth, *J. Electron. Mater.* **26**(3), 113-18 (1997).
- <sup>61</sup> K. Tone, S.P. Weiner, J.H. Zhao, *Electron. Lett.* **33**, 1904 (1997).
- <sup>62</sup> H. Wirth, D. Panknin, W. Skorupa, E. Niemann, *App. Phys. Lett.* **74**, 979 (1999).
- <sup>63</sup> S.G. Sundaresan, M.V. Rao, Y-L. Tian, M.C. Ridgway, J.A. Schreifels, J.J. Kopanski, *J. Appl. Phys.* **101**(7), 073708 (2007).
- <sup>64</sup> J.A. Gardner, A. Edwards, M.V. Rao, N. Papanicolaou, G. Kelner, O.W. Holland, M.A. Capano, M. Ghezzi, J. Kretchmer, *J. Appl. Phys.* **83**, 5119 (1998).

- <sup>65</sup> K.V. Vassilevski, N.G. Wright, I.P. Nikitina, A.B. Horsfall, A.G. O'Neill, M.J. Uren, K.P. Hilton, A.G. Masterson, A.J. Hydes and C.M. Johnson, *Semicond. Sci. Technol.* **20**, 271-278 (2005).
- <sup>66</sup> K.A. Jones, P.B. Shah, K.W. Kirchner, R.T. Lareau, M.C. Wood, M.H. Ervin, R.D. Vispute, R.P. Sharma, T. Venkatesan and O.W. Holland, *Mater. Sci. & Eng. B*, **61-62**, 281 (2000).
- <sup>67</sup> K. Hata, A. Kawazu, T. Okano, T. Ueda and M. Akiyama, *Appl. Phys. Lett.* **63**, 1625–7 (1993).
- <sup>68</sup> V.R. Vathulya, M.H. White M H, *Solid-State Electron.* **44**, 309–15 (2000).
- <sup>69</sup> Y. Negoro, T. Kimoto, H. Matsunami, F. Schmid, G. Pensl, *J. App. Phys.* **96**, 4916 (2004).
- <sup>70</sup> H. Wirth, D. Panknin, W. Skorupa and E. Niemann, *Appl. Phys. Lett.* **74**, 979 (1999).
- <sup>71</sup> W.C. Mitchel, A.O. Evarayay, S.R. Smith, M.D. Roth, *J. Electron. Mater.* **26**, 113 (1997).
- <sup>72</sup> G.L. Harris (ed.), *Properties of Silicon Carbide*, INSPEC, IEEE Press, London (1995).
- <sup>73</sup> S.G. Sundaresan, Y-L. Tian, M.V. Rao, J.A. Schreifels, J. Zhang, E. Gomar-Nadal, *Solid-State Electronics* (accepted for publication).
- <sup>74</sup> K.A Jones, M.A. Derenge, P.B. Shah, T.S. Zheleva, M.H. Ervin, K.W. Kirchner, M.C. Wood, C. Thomas, M.G. Spencer, O.W. Holland, and R.D. Vispute, *J. Electron. Mater.* **31** 568 (2002).
- <sup>75</sup> Y. Negoro, K. Katsumoto, T. Kimoto, and H. Matsunami, *Mater. Sci. Forum* **457-460** 933 (2004).

- <sup>76</sup> Y. Negoro, K. Katsumoto, T. Kimoto, and H. Matsunami, *J. Appl. Phys.* **96**, 224 (2004).
- <sup>77</sup> O.J. Guy, D. Doneddu, L. Chen, M.R. Jennings, M.P. Ackland, R. Baylis, M.D. Holton, P. Dunstan, S.P. Wilks, P.A. Mawby, *Diam. Rel. Mater.* **15**, 1472 (2006).
- <sup>78</sup> R.V. Kukta, A. Peralta, and D. Kouris, *Phys. Rev. Lett.* **88**, 186102 (2002).
- <sup>79</sup> W. Chen and M.A. Capano, *J. Appl. Phys.* **98**, 114907 (2005).
- <sup>80</sup> H. Nakagawa, S. Tanaka, and I. Suenume, *Phys. Rev. Lett.* **91**, 226107 (2003).
- <sup>81</sup> J.J. Sumekaris, J.R. Jenny, and A.R. Powell, *MRS Bull.* **22**, 19 (1997).
- <sup>82</sup> T. Troffer, M. Schadt, T. Frank, H. Itoh, G. Pensl, J. Heindl, H.P. Strunk, and M. Maier, *Phys. Stat. Sol. A* **162**, 277 (1997).
- <sup>83</sup> F. Schmid, M. Laube, G. Pensl, G. Wagner, M. Maier, *J. Appl. Phys.* **91**, 9182 (2002).
- <sup>84</sup> Y. Wang, P.A. Losee, S. Balachandran, I.B. Bhat, T.P. Chow, Y. Wang, B.J. Skromme, J.K. Kim, E.F. Schubert, proceedings of the 6<sup>th</sup> ECSCRM held in Newcastle upon Tyne, September 2006, p 567.
- <sup>85</sup> H. Kiessig, *Ann. Phys. Leipzig* **10**, 769 (1931).
- <sup>86</sup> J. Simonson, S.B. Qadri, M.V. Rao, R. Fischer, J. Grun, and M.C. Ridgway, *Appl. Phys. A* **81** 601 (2005).
- <sup>87</sup> B.D. Cullity and S.R. Stock, *Elements of X-Ray Diffraction*, (Prentice-Hall, 2001), page 512.

- <sup>88</sup> J. Pernot, S. Contreras, and J. Camassel, *J. Appl. Phys.* **98**, 023706 (2005).
- <sup>89</sup> J.D. Wiley, in *Semiconductors and Semimetals*, edited by R.K. Willardson and A.C. Beer (Academic, New York, 1975), Vol **10**.
- <sup>90</sup> N.S. Saks, A.V. Suvorov, and D.C. Capell, *Appl. Phys. Lett.* **94**, 5195 (2004).
- <sup>91</sup> G. Pensl et al. *Mater. Sci. Forum* **433-436**, 365 (2003).
- <sup>92</sup> R.Y. Korotkov, J.M. Greigie, B.W. Wessels, *Appl. Phys. Lett.* **78**, 222 (2001).
- <sup>93</sup> N. Yamamoto, H. Katayama-Yoshida, Proceedings of the 19<sup>th</sup> International Conference on Defects in Semiconductors, Aveiro, Portugal, 1185 (1997).
- <sup>94</sup> O. Brandt, H. Yang, H. Kostial, K.H. Ploog, *Appl. Phys. Lett.* **78**, 222 (2001).
- <sup>95</sup> H.T. Wang et al. *J. Appl. Phys.* **98**, 094901 (2005).
- <sup>96</sup> K.T. Liu et al. *J. Appl. Phys.* **98**, 073702 (2005).
- <sup>97</sup> H.Y.A. Chung et al. *J. Crys. Growth* **230**, 549 (2001).
- <sup>98</sup> O. Ambacher, *J. Phys. D* **31**, 2653 (1998).
- <sup>99</sup> R.G. Wilson et al. *J. Vac. Sci. Tech. A* **17**, 1226 (1999).
- <sup>100</sup> C.R. Eddy, Jr. et al. *Appl. Phys. Lett.* **90**, 162101 (2007).
- <sup>101</sup> S.S. Hullavarad, R.D. Vispute et al. *J. Electron. Mater.* **35**, 777 (2007).

- <sup>102</sup> J.A. Freitas, Jr. *J. Cryst. Growth*, **281**, 168 (2005).
- <sup>103</sup> R. Dalmau S. Collazo Z. Mita Z. Sitar, *J. Electron. Mater.* DOI: 10.1007/s11664-006-0044-x (2007).
- <sup>104</sup> M.E. Levinshtein, S. Rumyantsev, M.S. Shur (eds.), *Properties of Advanced Semiconductor Materials: GaN, AlN, InN, SiC, SiGe*, Wiley-Interscience (2001).
- <sup>105</sup> B.P. Gila, S.J. Pearton et al. *Proc. Electrochem. Soc.* **4**, 247 (2005).
- <sup>106</sup> C. Kumtornkittikul, M. Sugiyama Y. Nakano, *J. Electron. Mater.* **35**, 744 (2006).
- <sup>107</sup> M.A. Reschikov, H. Morkoc, *J. Appl. Phys.* **97**, 061301 (2005).
- <sup>108</sup> M.A. Reschikov G-C. Yi B.W. Wessels, *MRS Internet J Nitride Semicond. Res.* 4S1, G11.8 (1999).
- <sup>109</sup> H. Teisseyre, J.A. Freitas, Jr. et al. *Phys. Rev. B*, **62**, 10151 (2000).
- <sup>110</sup> M.G. Ganchenkova, R.M. Nieminen, *Phys. Rev. Lett.* **96** 196402 (2006).
- <sup>111</sup> R.S. Wagner, W.C. Ellis, *Appl. Phys. Lett.* **4**, 89 (1964).
- <sup>112</sup> J.B. Hannon, S. Kodambaka, F.M. Ross, R.M. Tromp, *Nature*, **440**, 69 (2006).
- <sup>113</sup> W.F. Knippenberg, *Philips Res. Rep.* **18**, 161 (1963).
- <sup>114</sup> M. Omuri, H. Takei, T. Fukuda, *Japan. J. Appl. Phys.* **28**, 1217 (1989).

- <sup>115</sup> V. Heine, C. Cheng, R.J. Needs, *J. Am. Ceram. Soc.* **74**, 2630 (1991).
- <sup>116</sup> S. Limpijumnong, W.R.L. Lambrecht, *Phys. Rev. B* **57**, 12017 (1998).
- <sup>117</sup> Y.M. Tairov, V.F. Tsevtkov, *J. Cryst. Growth* **52**, 146 (1981).
- <sup>118</sup> H. Nakashima, H. Harima, *Phys. Stat. Sol. A*, **162**, 39 (1997).
- <sup>119</sup> H. Harima, S. Nakashima, J. M. Carulli, C. P. Beetz, and W. S. Yoo, *Japan. J. Appl. Phys.* **36**, 5525 (1997).
- <sup>120</sup> J. Frechette, C. Carraro, *J. Am. Chem. Soc.* **128**, 14774 (2006).
- <sup>121</sup> J. Frechette, C. Carraro, *Phys. Rev. B* **74**, 161404 (2006).
- <sup>122</sup> Z. J. Li, J. L. Zhang, A. Meng, J. Z. Guo, *J. Phys. Chem. B* **110**, 22382 (2006).
- <sup>123</sup> R. Merlin, A. Pinczuk, and W. H. Weber, in *Raman scattering in materials science*, 42 ed., edited by W. H. Weber and R. Merlin (Springer-Verlag, Berlin, 2000), p. 1-29.
- <sup>124</sup> K. Karch, P. Pavone, W. Windl, O. Schutt, D. Strauch, *Phys. Rev. B* **50**, 17054 (1994).
- <sup>125</sup> D. Olego and M. Cardona, *Phys. Rev. B* **25**, 1151 (1982).
- <sup>126</sup> J. F. Digregorio, T. E. Furtak, *Solid State Communications* **89**, 163 (1994).
- <sup>127</sup> D.K. Schroder, *Semiconductor and Device Characterization*, IEEE Press, New Jersey, 2007.

## **Curriculum Vitae**

Siddarth G. Sundaresan was born in Mumbai, India on November 12<sup>th</sup>, 1979. He received his Bachelors degree in Computer Engineering from Mumbai University in June, 2001. He subsequently received his Masters in Electrical Engineering and his Ph.D. in Electrical and Computer Engineering, both from George Mason University, in December 2004, and December 2007, respectively.